NUMERICAL INVESTIGATIONS ON FACTORS INFLUENCING LIMIT LOADING FOR TRANSONIC TURBINE AIRFOILS

by

Spencer Sutherland Owen

A dissertation submitted to the faculty of
The University of North Carolina at Charlotte
in partial fulfillment of the requirements
for the degree of Doctor of Philosophy in
Mechanical Engineering

Charlotte

2021

Approved by:

____

Dr. Mesbah Uddin

____

Dr. Badrul Chowdhury

____

Dr. Amirhossein Ghasemi

____

Dr. Russell Keanini

ABSTRACT

SPENCER SUTHERLAND OWEN. Numerical Investigations on Factors Influencing Limit Loading for Transonic Turbine Airfoils. (Under the direction of DR. MESBAH UDDIN)

To stay competitive within the gas turbine community, turbine aero designers strive to maximize the total work output of each turbine stage through a combination of airfoil design improvements and increased total pressure ratio. Although increasing the mass flow rate could achieve a higher power target, the resultant increase in turbine annulus would result in structural limitations due to longer blades which cause increased strain on the blade root as well as amplified flutter and rotor dynamic excitation. An alternative path to achieving higher power output is to maximize the loading of each turbine stage through increased pressure ratio, but this may lead to airfoil limit loading and high aerodynamic losses.

This research systematically develops a detailed methodology to simulate the prediction of airfoil limit loading as well as provides a thorough investigation into the factors that influence the limit loading condition. A computational baseline was established using data previously collected at the Pratt & Whitney Canada High-Speed Wind Tunnel at Carleton University near design conditions. A number of eddy viscosity turbulence models were explored with the SST $k-\omega$ turbulence model with γ transition found to have superior predictive veracity for the limit loading condition. Development of an adaptive mesh refinement algorithm based on the normalized local cell gradients of pressure, temperature, density, turbulent kinetic energy, turbulent eddy viscosity and the specific dissipation rate of turbulence achieved an overall reduction in computational cost of roughly 50% per simulation.

Variation of turbine inflow conditions were analyzed for four different transonic turbine airfoils based on flow conditions exhausted by an upstream combustor. Influence was found to be minimal on the exit flow profile with the exception of the mass-flow averaged total pressure loss coefficients. Results show incidence variation to change the total pressure loss differently for each airfoil, whereas turbulence intensity and turbulent length scale predicted a drastic rise in loss with increased turbulence level for all airfoils considered. The geometric characteristics of each airfoil were also investigated for influence on the stages to limit loading. Similar to previous experimental work, the limit loading pressure ratio and the mass-flow averaged outlet flow angle were strongly correlated with the airfoil outlet metal angle. It was also determined that the airfoil stagger and trailing edge blockage ratio play a role in the determination of the sublimit loading range, although no definitive parameter could be isolated due to lack of specific geometric constraints.

Lastly, the effect of transient vortex shedding on the nature of the trailing edge shock system and subsequent influence on the stages towards limit loading were investigated. Each modeling strategy (URANS, DES and turbulence model free) predicted separation along the suction surface during limit loading due to acoustic wave propagation caused by the shock-base pressure interaction, although with varying degrees of size and magnitude. Temporal evolution of the mass flow averaged total pressure loss coefficient downstream of the airfoil allowed for the dominant vortex shedding frequency to be determined and subsequent Strouhal number to be calculated. It was found that each transient modeling strategy predicted the vortex frequency differently. A formal documentation and review were made outlining the required simulation time step to achieve accurate temporal resolution as well as approximate vortex shedding period. Qualitative images of numerical Schlieren contours were presented and reviewed showing large differences in the prediction of vortex shape, size, and subsequent shock influence. Although conclusions were made on modeling ability, without extensive experimental documentation no concrete justification can be made at this time, outlining the importance of an experimental investigation.

DEDICATION

This work is dedicated first to my parents, Kevin and Laura Owen, and my brother Dylan Owen who provided the much needed motivation to keep me focused on the finish line.

Secondly to my grandparents, Sam and Judy Owen and Paul and Connie Sutherland. Without the continual support and love they provided throughout my life this would not have been possible.

And finally, to my loving wife, Dr. Sandy Owen, for being my cheerleader throughout the last stages of the PhD endeavor.

Thank you all.

ACKNOWLEDGEMENTS

I would like to thank my advisor, Dr. Mesbah Uddin, and industry mentor, Dr. Farzad Taremi, for providing guidance and support throughout the PhD process. Thank you both for sticking with me to the end and providing the invaluable guidance to complete this research.

I would also like to thank Carlton University for providing the data used to validate the numerical methodology used in this research project.

Finally, I would like to thank Siemens Energy, Inc. for providing the airfoil geometries and for allowing me to publish our research findings.

TABLE OF CONTENTS

LIST OF TABLES

LIST OF FIGURES

LIST OF SYMBOLS

α Incidence angle.

α_1 Inlet flow angle.

α_2 Outlet flow angle.

α_{Eval} Evaluation plane flow angle.

α_{TE} Trailing edge plane flow angle.

β_1 Inlet metal angle.

β_2 Outlet metal angle.

ω Specific dissipation rate of turbulent kinetic energy.

ϕ Scalar quantity of interest or phase angle.

ρ Density.

θ_{UG} Unguided turn angle.

ζ Stagger angle.

A_o Initial cell area.

A_{in} Inlet plane (Paper 1, Paper 3).

A_j Measuring Plane at location j.

A_{LPL} Area of the last prism layer.

A_{out} Outlet Plane (Paper 1, Paper 3).

B_{eval} Evaluation Plane.

B_{in} Inlet plane (Paper 2).

B_{out} Outlet Plane (Paper 2).

c True chord.

c_1 Numerical Schlieren constant 1.

c_2 Numerical Schlieren constant 2.

C_t True chord.

c_{ax} Axial chord.

C_{P_b} Base pressure coefficient.

C_{po} Downstream total pressure loss coefficient.

d_{te} Trailing edge diameter.

f Frequency.

h Span.

k Turbulent kinetic energy.

l Turbulent length scale.

M Mach number.

M_x Axial component of Mach number.

$M_{2,isen}$ Outlet isentropic Mach Number.

M_{isen} Isentropic Mach Number.

$M_{s,isen}$ Surface isentropic Mach Number.

o Throat width.

P_b Static base pressure.

P_{o1} Inlet total pressure.

P_{o2} Outlet total pressure.

P_{oe} Evaluation plane total pressure.

P_{se} Evaluation plane static pressure.

P_s Static pressure.

PR_{LL} Limit loading pressure ratio.

q_e Evaluation plane dynamic pressure.

Re_c Reynolds number based on the true chord.

s Pitch.

St Strouhal number.

t Trailing edge diameter.

T_t Total temperature.

TI Turbulence intensity.

U Velocity.

U_{inf} Free-stream velocity.

$V_{2,is}$ Downstream isentropic velocity.

Y_m Mixed-out total pressure loss coefficient.

Y_P Local total pressure loss coefficient.

AMR Adaptive Mesh Refinement.

CFD Computational Fluid Dynamics.

DDES Delayed Detached Eddy Simulation.

DES Detached Eddy Simulation.

MF Model Free.

PR Pressure Ratio.

RANS Reynolds-Averaged Navier-Stokes.

TE Trailing Edge.

TEPSS Trailing Edge Pressure Side Shock.

TESSS Trailing Edge Suction Side Shock.

URANS Unsteady Reynolds-Averaged Navier-Stokes.

CHAPTER 1: INTRODUCTION

Whether used for propulsion or power generation, gas turbines remain an essential component of contemporary engineering. A balance of high efficiency and high power-to-weight ratio allows the application of gas turbines to continue to grow and increase in demand. Understanding and predicting the flow phenomena associated with these systems continues to be a major area of research, and further improvement can save both economic and environmental resources.

To stay competitive within the gas turbine community, turbine aero designers strive to maximize the total work output of each turbine stage through a balance of increased pressure ratio and airfoil design enhancements. Although a higher power target could be achieved by increasing mass flow rate, the corresponding increase in turbine annulus area would result in structural limitations due to longer blades which cause increased strain on the blade root as well as amplified flutter and rotor dynamic excitation. An alternative path to achieving higher power output is to maximize the loading of each turbine stage through increased pressure ratio, but this may lead to airfoil limit loading and high aerodynamic losses.

Airfoil limit loading was first documented in a National Advisory Committee for Aeronautics (NACA) Research Memorandum in the early 1950's [1, 2]. It was shown that the airfoil outlet metal angle was the dominant geometric factor to influence the point of limit loading. Since then numerous studies have proposed numerical methods to predict the pressure ratio required to reach limit loading [3, 4, 5] to name a few. Although these methods predict the onset of limit loading fairly well there has yet to be a robust method that provides detailed flow characteristics [6]. Computational fluid dynamics (CFD) provides the gas turbine community with an efficient and reliable method to analyze this condition allowing for a better understanding of the overall flow, potentially extending a turbine airfoil design envelope and reducing the total number of stages required to produce a specific power demand.

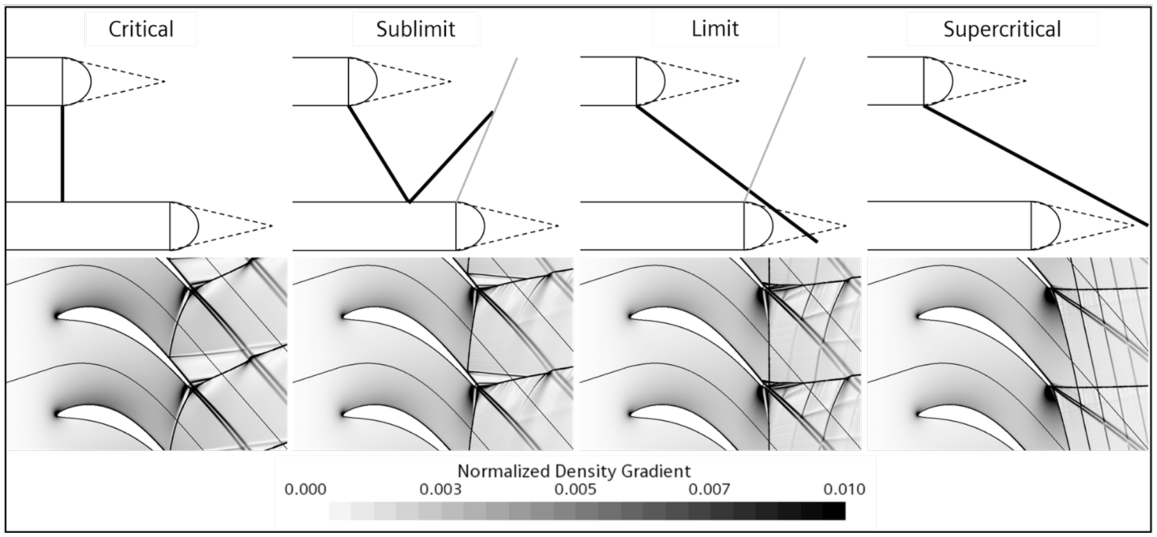

Figure 1.1: Limit Loading: Terminology (Reproduced from Chapter 4).

Figure 1.1 illustrates the terminology used to describe the stages of airfoil loading from critical to supercritical conditions. The top set of images provide a simplified representation of the trailing edge shock structure for a transonic turbine airfoil, while the bottom provides a realistic contrast of numerical Schlieren RANS CFD predictions.

The left most image, defined by the onset of choking within the blade passage due to a strong Trailing Edge Pressure Side Shock (TEPSS) normal to the airfoil surface, describes the critical loading condition. The bold solid line in the simplified representation is the TEPSS located at the throat of the airfoil passage. Here the flow has reached Mach one and the upstream fluid has become fully choked. As the pressure ratio is increased the TEPSS becomes oblique due to the Prandtl-Meyer expansion near the trailing edge. The TEPSS impinges on the adjacent airfoil suction surface and reflects downstream, ultimately coalescing with the weaker Trailing Edge Suction Side Shock (TESSS) and further propagating downstream towards the wake.

This is defined as the sublimit loading range which spans over a number of pressure ratios from critical to limit loading depending on the airfoil geometry. The extents of the pressure ratio to achieve sublimit loading is discussed in Chapter 3 and shown to be dependent on the airfoil geometry, specifically the airfoil stagger angle and trailing edge blockage ratio. Further increase of the pressure ratio causes the TEPSS to obtain sufficient flow turning to completely miss the surface of the adjacent airfoil, moving into the base pressure region downstream of the trailing edge. This is the point of maximum loading and is defined as the limit loading condition. Super critical loading is the fourth and final loading condition, shown as the right most set of images in Figure 1.1. Here a strong oblique TEPSS is produced that propagates downstream of the base pressure region of the adjacent airfoil and into the flow passage, causing the entire domain to become choked.

The purpose of this thesis is to develop a detailed methodology to simulate the prediction of airfoil limit loading as well as to provide the engineering community with a thorough investigation into the factors that influence the limit loading condition. Chapter 2 (Paper 1) establishes a computational baseline using data previously collected at the Pratt & Whitney Canada High-Speed Wind Tunnel at Carleton University near design conditions. A number of eddy viscosity turbulence models were explored with the SST $k-\omega$ turbulence model with γ transition found to have superior predictive veracity for the limit loading condition. Development of an adaptive mesh refinement algorithm based on the normalized local cell gradients of total pressure, total temperature, density, turbulent kinetic energy, turbulent eddy viscosity and the specific dissipation rate of turbulence achieved an overall reduction in computational cost of roughly 50% per simulation.

Using this baseline, Chapter 3 (Paper 2) investigates the sensitivities of inflow conditions on airfoil limit loading characteristics as well as provides a detailed analysis of the entire flow domain during limit loading for a set of four different transonic turbine airfoils. Focus is given to the potential boundary conditions exhausted by a combustor; variation of inlet flow angle and turbulence quantities: intensity and length scale. The flow within a turbine passage, specifically during ramping procedures experiences a wide range of both incidence and turbulence variation [7]. This is not included in modern compressible flow theory; therefore, it is unclear how these would affect the onset of choking or limit loading.

It was determined that, similar to previous experimental work, the limit loading pressure ratio and the mass-flow averaged total flow turning were strongly correlated with the airfoil outlet metal angle. The influence of inflow conditions was minimal on the exit flow profile with the exception of the mass-flow averaged total pressure loss coefficients. Results show incidence variation to change the total pressure loss coefficient depending on the airfoil, whereas turbulence intensity and turbulent length scale predicted a drastic increase in loss with increased turbulence level for all airfoils considered.

Chapter 4 (Paper 3) examines the effect of transient vortex shedding on the nature of the trailing edge shock system and subsequent influence on the stages towards limit loading. The objectives of this chapter were to identify the effects of vortex shedding on the nature of the trailing edge shock system during airfoil limit loading and to document an assessment of the ability of common transient modeling approaches to aid in the decisions of turbine aero designers. Three unsteady modeling strategies were employed and compared for their predictive capabilities: unsteady RANS, Delayed Detached Eddy Simulations, and turbulence model free.

Each modeling strategy predicted the base pressure region, trailing edge shock structures and trailing edge boundary layers quite differently. A detailed review of the boundary layer states at the trailing edge were performed showing that all of the modeling approaches predicted laminar boundary layer profiles along the pressure surface trailing edge and turbulent profiles along the suction surface trailing edge.

Separation along the suction surface during limit loading occurred for each numerical approach due to acoustic wave propagation caused by the shock-base pressure interaction, although with varying degrees of size and magnitude. A formal documentation and review were made outlining the required simulation time step to achieve accurate temporal resolution as well as approximate the vortex shedding period. Temporal evolution of the mass flow averaged total pressure loss coefficient downstream of the airfoil allowed for the dominant vortex shedding frequency to be determined and subsequent Strouhal number to be calculated. It was found that each transient modeling strategy predicted the vortex frequency differently; however, within experimental and numerical norms.

The research presented in this dissertation is in the three-article format. Chapter 2 has been published in the American Institute of Aeronautics and Astronautics conference proceedings in Dallas, Texas 2019, and establishes the numerical foundation for this thesis. Chapter 3 (Paper 2) provides an evaluation of the effect of inflow conditions on limit loading as well as an assessment and determination of the sensitivity of airfoil geometric characteristics on limit loading performance. This work has been accepted for publication in the Institute of Mechanical Engineers Power and Energy Journal and is expected to be published this spring. The third and final paper included in Chapter 4 presents an assessment of the effect of transient vortex shedding on the trailing edge shock system and subsequent development of the limit loading condition. This work has been submitted to the Journal of Turbomachinery and is awaiting editorial response. The amount of information provided shows the requirement of three articles for the proper support of this thesis.

The vision of this dissertation is to increase the overall understanding of how inflow conditions, airfoil design and computational modeling assumptions affect the limit loading of transonic airfoils. A new adaptive mesh refinement algorithm was created reducing computational cost by 50% and the numerical methodology was thoroughly validated showing the ability to properly capture the aerodynamics of airfoil limit loading. The impact of inflow conditions was found to be insignificant on the prediction of the pressure ratio to reach limit loading as well as the total flow turning within the passage; however, the inflow conditions were found to have a significant influence on the total pressure loss through the system. Thus, the research presented in this dissertation provides the turbine aero community with assurance that combustor discharge will not affect the limit loading profile; however, will significantly affect the total pressure loss through the system. An assessment of the contribution of airfoil geometric characteristics to the stages of limit loading was also conducted, showing the outlet metal angle to directly influence the pressure ratio to reach limit loading and the trailing edge blockage ratio to inversely alter the pressure ratio to reach critical loading. Stagger angle and airfoil unguided turning were identified as additional factors that could potentially influence the pressure ratio to reach limit loading; however, an additional study isolating each parameter is needed to provide sufficient assessment. Lastly the influence of trailing edge vortex shedding on the nature of the trailing edge shock system was performed. It was shown that transient influence was minimal for most engineering application; total flow turning, total pressure loss, and the pressure ratio to reach limit loading. An additional low frequency dynamic was identified using the DES modeling approach; however, without an extensive experimental investigation no justification can be made at the accuracy of this prediction. Therefore, additional experimental work is needed to provide the academic community with assurance of the various prediction methods.

REFERENCES

[1] C. H. Hauser, H. W. Plohr, and G. Sonder, "Study of flow conditions and deflection angle at exit of two-dimensional cascade of turbine rotor blades at critical and supercritical pressure ratios," *NACA-RM E9K25*, 1950.

[2] C. H. Hauser and H. W. Plohr, "Two-dimensional cascade investigation of the maximum exit tangential velocity component and other flow conditions at the exit of several turbine blade designs at supercritical pressure ratios," *NACA-RM E51F12*, 1951.

[3] I. Fruchtman, "The limit load of transonic turbine blading," in *Turbo Expo: Power for Land, Sea, and Air*, vol. 79788, p. V01AT01A080, American Society of Mechanical Engineers, 1974.

[4] A. J. Glassman, "Estimating turbine limit load," *NASA CR-191105*, 1993.

[5] S. S. Chen, "Axial-flow turbine rotor discharge-flow overexpansion and limit-loading condition. part 2; method of analysis and performance evaluation of computer code axod2," *NASA/TM-2018-219911*, 2018.

[6] S. S. Chen, "Axial-flow turbine rotor discharge-flow overexpansion and limit-loading condition, part 1: Computational fluid dynamics (cfd) investigation," *NASA/TM-2017-219506*, 2017.

[7] M. Folk, *The Impact of Combustor Turbulence on Loss Mechanisms in the High Pressure Turbine*. PhD thesis, University of Cambridge, 2020.

CHAPTER 2: (PAPER 1) TURBULENCE MODELING EFFECTS OF TRANSONIC, HIGH PRESSURE AIRFOILS AT DESIGN INCIDENCE

2.1 Introduction

Gas turbines, whether used for propulsion or power generation remain a fundamental component of modern engineering. A combination of high efficiency and high power-to-weight ratio allows the application of gas turbine engines to continue to grow and increase in demand. Understanding and predicting the flow phenomena associated with these systems continues to be a major area of research, and further improvement can save both economic and environmental resources. Simulation efficiency, robustness and reliability define the success of a modeling scheme which should be balanced for a beneficial design process. To fully understand the flow characteristics within a high pressure turbine system as well as to optimize the numerical methods for industrial applications, a thorough investigation into the limitations of potential modeling options should be conducted. A look into the ability of three Reynolds-Averaged Navier-Stokes (RANS) eddy viscosity turbulence models are explored here in an effort to determine the most reliable and accurate prediction method for this set of conditions.

The midspan aerodynamic characteristics of turbomachinary in both subsonic and transonic applications have been fairly well documented experimentally. Hoheisel et al. [1] and Xu and Denton [2] were among the first to investigate subsonic and transonic cascades. The former investigated the influence of free-stream turbulence on aerodynamic performance while the latter presented secondary losses of varying trailing edge thickness. These initial studies established the need for a better understanding of various loss generation mechanisms within turbine systems. Mee et al. [3]

expanded the understanding of loss components by describing them as split into three distinct regions: (a) the boundary layer along the blade surface, (b) possible shock wave discontinuities, and (c) mixing occurring downstream of the trailing edge. Denton [4] further expanded on the origins of loss generation, exploring the underlying process of entropy production rather than relying on the available prediction methods for determination of loss.

A number of computational studies associated with the impact of RANS modeling on the predictions of turbomachinary performance exist, cf. Mayle [5] and Michelassi [6]; both concluded that a transition model was necessary to the proper prediction of the overall flow pattern. A few years later Dunn [7] provided an extensive review of the state of numerical investigations for turbine systems in relation to blade heat transfer showing a lack of understanding into the mechanisms depreciating the value of RANS modeling. Ledezma et al. [8] extended the investigation to a high pressure turbine vane, further exemplifying the need of a transition model in predicting the possible separation and reattachment along the suction surface. More recently Duan et al. [9] explored the underlying mechanisms within loss generation of transonic cascades. They concluded that RANS modeling is an accurate tool for predicting loss generation trends with exit Mach number. The current investigation focuses on the limitations of RANS eddy viscosity turbulence modeling, specifically on the ability of each model to accurately predict surface pressure distributions, total pressure loss, shock location and base pressure.

The majority of experimental data used for simulation validation was collected at the Pratt & Whitney Canada (PWC) high-speed wind tunnel (HSWT) at Carleton University in Ottawa, Canada by Sooriyakumaran [10]. PWC tunnel is a blow-down configuration and is capable of sustaining stable transonic flow for up to sixty seconds. Both Reynolds number and exit Mach number can be varied independently due to an ejector-diffuser assembly [11] which modifies the static pressure at the outlet.

For a detailed description of the tunnel, an interested reader is referred to either the work of Sooriyakumaran [10] or Taremi [12]. This paper also presents a second experimental validation using the work of Stastny and Safarik [13] which has been extensively documented on the website of the European Research Community on Flow, Turbulence and Combustion (ERCOFTAC) knowledge base [14].

All simulations presented in this paper were performed using a commercial finite volume code, StarCCM+. Three steady-state RANS eddy viscosity turbulence models were tested for prediction veracity; these include the shear-stress transport (SST) $k-\omega$ with γ−Re$_\theta$ transition (Menter et al. [15]), the Abe-Kondoh-Nagano (AKN) low-Reynolds number $k-\varepsilon$ (Abe et al. [16]), and $\upsilon^2 - f$ (V2F) $k-\varepsilon$ (Durbin [17]) models. These models were chosen due to their more realistic aerodynamic prediction capabilities and potentials as seen in the existing literature as well as their additional intrinsic properties. The SST model provides an additional correlation based transition function to provide a means to emulate the mechanisms of transition onset [15], the AKN model utilizes a Kolmogorov velocity scale rather than friction velocity to account for near-wall and low-Reynolds number effects [16], and the V2F model employs a turbulent velocity scale rather than kinetic energy to account for the near-wall damping of eddy viscosity [17].

2.1.1 Total Pressure Loss Coefficient and Mixing-Out Procedure

Arguably, the most useful definition of turbine loss coefficient, for design purposes, is the measure of entropy generation throughout the passage. Entropy generation occurs from at least three different areas; one, through a reduction in total pressure from inlet to outlet, two, an increase in static enthalpy at the outlet, and three, a decrease in the velocity at the outlet. Unfortunately, entropy is a not a directly measurable quantity, therefore various loss coefficient formulations have been proposed; for a detailed description of the definitions see Denton [4].

To maintain consistency with the experiments, a mass-averaged loss coefficient

(Y_P), defined as the total pressure loss normalized by the outlet dynamic pressure, was used in line with Kind et al. [18].

$$Y_P = \frac{P_{oi} - P_{oe}}{q_e} \tag{2.1}$$

Here subscripts i, e denote values of the total pressure (P_o) at the inlet and mixed-out exit measuring planes, respectively, and q represents the dynamic pressure; all quantities were mass-averaged using the formulations of Ligrani [19].

To fully capture the entropy generated by mixing downstream of the evaluation plane, a procedure originally proposed by Oldfield et al. [20] and later modified by Amecke and Safarik [21], was employed. In these calculations, a theoretical outlet plane is defined as the point at which the flow becomes fully mixed and is uniform along the pitch-wise direction. Using a control volume extending from the measuring plane to the theoretical mixed-out plane, the conservation of mass, momentum and energy can be simultaneously solved to determine the fully mixed quantities.

2.1.2 Critical Flow Areas

As mentioned earlier, losses within turbine cascades can be categorized into three areas; that accumulated within boundary layers, that generated through shocks and that caused by mixing [3]. It has been shown that the degree of influence of each component varies with Reynolds number, exit Mach number and free stream turbulence [3, 22]. In preparation for subsequent analyses, the following section highlights the essential physics affecting each component as well as their dependence on one another. The critical areas of interest are the boundary layer development on the airfoil surface, the shock-boundary interaction on the suction surface, and the base pressure region at the trailing edge.

2.1.2.1 Shock-Boundary Layer Interaction

Shocks are both unwanted and unavoidable processes within transonic turbine cascades. They are innately irreversible and direct sources of entropy generation. Depending on inlet flow angle and blade geometry, regions of supersonic flow can begin at exit Mach numbers (M_2) as low as 0.6. As M_2 approaches unity, the region of supersonic flow shifts downstream eventually ending at the trailing edge, whereupon the pressure and suction flows expand through the base pressure region ultimately coalescing into an oblique shock propagating from the trailing edge [23]. The boundary layer loss along the suction surface is directly related to the magnitude and direction of the shock propagating from the adjacent blade, due to the possible shock-boundary layer interactions.

Depending on the shock strength, the boundary layer separation can be complete or partial. It has been shown for compressors that an upstream flow of Mach 1.4 will cause complete boundary layer separation [24], whereas for weaker shocks, as is the case for most turbines, the flow creates a small separation bubble. This causes an increase in dissipation both within and downstream of the separation bubble causing an increase in boundary loss; for a thorough description see the work of Graham and Kost [25] or the technical report by Delery and Marvin [26].

2.1.2.2 Base Pressure Region

The speed of the expansion around the trailing edge of the suction- and pressure-side flows is directly related to the magnitude of the blade base pressure [2]. It has been shown that the contribution of the trailing edge loss for transonic cascades ($M_2 \sim 0.8$ - 1.2) is nearly 1/3 of the total loss [3]. Therefore, quantification of this phenomenon is critical for a full understanding and prediction of losses within a transonic cascade. Using the approach of Denton [4], the stagnation pressure loss coefficient can be expressed as:

$$Y_{te} = -\frac{C_{P_b} t}{w} + \frac{2\theta}{w} + \left(\frac{\delta^* + t}{w}\right)^2 \tag{2.2}$$

Where t and w are the trailing edge thickness and the throat width. θ and δ^* are the displacement and momentum thickness of the boundary layer just upstream of the trailing edge. C_{P_b} is the base pressure coefficient and is defined below:

$$C_{P_b} = \frac{(P_b - P_2)}{q_2} \tag{2.3}$$

here P_b is the average pressure acting along the trailing edge within the base region, and P_2 and q_2 are values taken at the cascade outlet. An evaluation of the ability of each turbulence model to predict the base pressure coefficient will provide a better understanding of the mechanisms effecting loss generation.

2.2 Governing Equations

2.2.1 Mass, Momentum and Energy Conservation

For turbulent compressible flow, the steady-state Favre-Averaged Navier-Stokes equations can be written as,

$$\frac{\partial}{\partial x_j}\left(\overline{\rho}\widetilde{u_j}\right) = 0 \tag{2.4}$$

$$\frac{\partial}{\partial x_j}\left(\widetilde{u_i}\overline{\rho}\widetilde{u_j}\right) = -\frac{\partial p}{\partial x_i} + \frac{\partial}{\partial x_j}\left(\overline{\sigma_{ij}} + \tau_{ij}\right) \tag{2.5}$$

$$\frac{\partial}{\partial x_j}\left(\widetilde{u_j}\overline{\rho}\widetilde{H}\right) = \frac{\partial}{\partial x_j}\left(\overline{\sigma_{ij}}\widetilde{u_i} + \overline{\sigma_{ij}u_i''}\right) - \frac{\partial}{\partial x_j}\left(\overline{q_j} + c_p\overline{\rho u_j'' T''} - \widetilde{u}\tau_{ij} + \frac{1}{2}\overline{\rho u_i'' u_i'' u_j''}\right) \tag{2.6}$$

Here an overbar, $\overline{u}$, denotes a conventional time-averaged mean, an overtilde, $\widetilde{u}$, a density-averaged (Farve-average) mean, expressed as $\widetilde{u} = \overline{\rho u}/\overline{\rho}$, and a double prime,

u'', the fluctuating component of a density-average. The symbols u, p, T, and x all have their conventional meanings, k_T the thermal conductivity, c_p the heat capacity at constant pressure and Pr the Prandtl number. The viscous stress tensor, $\overline{\sigma_{ij}}$, for a Newtonian fluid is given by

$$\overline{\sigma_{ij}} = 2\widetilde{\mu}\left(\widetilde{S_{ij}} - \frac{1}{3}\frac{\partial \widetilde{u_k}}{\partial x_k}\delta_{ij}\right) \tag{2.7}$$

where δ_{ij} is the Kronecker delta, $\widetilde{S}_{ij}$, the density-averaged deviatoric rate-of-strain tensor, given by

$$\widetilde{S_{ij}} = \frac{1}{2}\left(\frac{\partial \widetilde{u_i}}{\partial x_j} + \frac{\partial \widetilde{u_j}}{\partial x_i}\right) \tag{2.8}$$

The dynamic viscosity (μ) and density (ρ) are calculated using the Sutherland's law and ideal gas law, respectively.

Looking at Eqs. 2.5 and 2.6, there exist a number of correlations that must be modeled to ensure proper closure. These are the Reynolds-stress tensor τ_{ij}, the turbulent heat-flux vector $c_p\overline{\rho u_j'' T''}$, and the molecular diffusion and turbulent transport $\overline{\sigma_{ij}u_i''} - \frac{1}{2}\overline{\rho u_i'' u_i'' u_j''}$. For two-equation turbulence models, the Reynolds-stress tensor is modeled using the Boussinesq approximation which incorporates the eddy viscosity μ_t,

$$\tau_{ij} = 2\widetilde{\mu_t}\left(S_{ij} - \frac{1}{3}\frac{\partial \widetilde{u_k}}{\partial x_k}\delta_{ij}\right) - \frac{2}{3}\overline{\rho}k\delta_{ij} \tag{2.9}$$

Initially, a number of eddy viscosity turbulence models were explored which included: (a) the Spalart-Almaras model, (b) the Standard, Realizable, AKN, and $v^2 - f$ $k-\varepsilon$ models, (c) the Standard and SST $k-\omega$ models, and (d) the SST $k-\omega$ model with γ - Re_θ transition. After evaluating the predictive capabilities of these models, the investigation was focused on the shear stress transport (SST) $k-\omega$ with γ - Re_θ transition model developed by Langtry and Menter [15] and two variants of the

$k-\varepsilon$ model, the Abe-Kandoh-Nagano (AKN) [16] and v^2-f (V2F) [17]. The selection process was decided based on the following attributes: 1) more realistic aerodynamic prediction capabilities as seen in the existing literature, 2) potential to account for laminar-to-turbulent transition as expected in the particular turbine flow field under investigation and 3) similarity amongst the numerical stability and convergence rate under these operating conditions. Specifically, the SST model provides an additional correlation based transition function to provide a means to emulate the mechanisms of transition onset, the AKN model utilizes a Kolmogorov velocity scale rather than friction velocity to account for near-wall and low-Reynolds number effects, and the V2F model employs a turbulent velocity scale rather than kinetic energy to account for the near-wall damping of eddy viscosity.

2.2.2 Turbulence Models

2.2.2.1 Shear-Stress Transport $k-\omega$ (SST)

The SST $k-\omega$ model proposed by Menter et al. [15] is one of the most commonly used turbulence models for CFD of turbomachinary [27, 8, 9]. Compared to the standard $k-\omega$ model [28], the SST model incorporates an additional non-conservative, cross-diffusion term containing the dot product, $\nabla k \cdot \nabla \omega$, into the ω transport equation. Furthermore, utilization of a blending function, F_1, that incorporates the cross-diffusion term far from the wall, allows for the advantages of the $k-\varepsilon$ model to be applied throughout the far field while maintaining the local boundary layer calculations within the near wall region. A summary of the expressions for the transport equations of turbulent kinetic energy, k, and its specific dissipation rate, ω, as well as the eddy viscosity, μ_t, are given in Eqs. 2.10 thru 2.13:

$$\frac{\partial}{\partial t}(\rho k) + \nabla \cdot (\rho k \overline{u}) = \nabla \cdot \left(\left(\mu + \sigma_k \mu_t \right) \nabla k \right) + P_k - \rho \beta^{\star} \omega k \tag{2.10}$$

$$\frac{\partial}{\partial t}(\rho\omega) + \nabla\cdot(\rho\omega\overline{u}) = \nabla\cdot((\mu+\sigma_\omega\mu_t)\nabla\omega) + P_\omega - \rho\beta\omega^2 \tag{2.11}$$

$$\mu_t = \rho\frac{a_1 k}{\max(a_1\omega, SF_2)} \tag{2.12}$$

$$S = \sqrt{2S_{ij}S_{ij}} \tag{2.13}$$

Here the terms P_k and P_ω are the production terms of kinetic energy and specific dissipation rate respectively; the function F_2 is a blending function; S is the modulus of the mean strain rate tensor (S_{ij}); f_c is a curvature correction factor; and a_1, β, β^*, σ_k and σ_ω are closure coefficients as defined by Menter et al. [29].

In addition, a correlation-based transition model was incorporated into the k equation to provide a semi-local approach to predicting transition. Here two additional transport equations, one for intermittency and the other for transition momentum thickness Reynolds number, were employed as given in Eqs. 2.14 and 2.15

$$\frac{\partial}{\partial t}(\rho\gamma) + \nabla\cdot(\rho\gamma\overline{u}) = \nabla\cdot\left(\left(\mu+\frac{\mu_t}{\sigma_f}\right)\nabla\gamma\right) + P_\gamma - E_\gamma \tag{2.14}$$

$$\frac{\partial}{\partial t}\left(\rho\overline{Re_{\theta t}}\right) + \nabla\cdot\left(\rho\overline{Re_{\theta t}}\overline{u}\right) = \nabla\cdot\left(\mu+\mu_t\nabla\overline{Re_{\theta t}}\right) + P_{\theta t} \tag{2.15}$$

For a detailed description on how the transition equations are incorporated into the SST model refer to the STAR-CCM+ documentation [30]. It should, however, be noted that the formulation of the transition correlations within STAR-CCM+ is slightly different than that of the original proposal by Menter et al. [31]. The original formulation provided in [31] was incomplete for a proper implementation in a turbulence model due to proprietary constraints; therefore, STAR-CCM+ allows the user to specify a custom field function for the definition of the free-stream edge.

This edge determines the position where the transition momentum thickness Reynolds number in the free-stream diffuses into the boundary layer. For this study, the free-stream edge was defined as the edge of the prism layers for the transition model; the authors acknowledged that the proper definition of this edge requires further exploration.

2.2.2.2 Abe-Kondoh-Nagano $k-\varepsilon$ (AKN)

The transport equations for the turbulent kinetic energy k and its dissipation rate ε for the AKN model are:

$$\frac{\partial}{\partial t}(\rho k) + \nabla \cdot (\rho k \overline{u}) = \nabla \cdot \left[\left(\mu + \frac{\mu_t}{\sigma_k}\right)\nabla k\right] + P_k - \rho\varepsilon \tag{2.16}$$

$$\frac{\partial}{\partial t}(\rho \varepsilon) + \nabla \cdot (\rho \varepsilon \overline{u}) = \nabla \cdot \left[\left(\mu + \frac{\mu_t}{\sigma_\varepsilon}\right)\nabla \varepsilon\right] + C_{\varepsilon 1} P_\varepsilon \frac{\varepsilon}{k} - C_{\varepsilon 2} f_2 \rho \frac{\varepsilon^2}{k} \tag{2.17}$$

where

$$\mu_t = \rho C_\mu f_\mu k T \tag{2.18}$$

and the damping functions f_2 and f_μ are defined as

$$f_2 = \left(1 - e^{-\frac{Re_\varepsilon}{3.1}}\right)^2 \left[1 - 0.3 e^{-\left(\frac{R_t}{6.5}\right)^2}\right] \tag{2.19}$$

$$f_\mu = \left(1 - e^{-\frac{Re_\varepsilon}{14}}\right)^2 \left[1 + \frac{5}{Re_t^{3/4}} e^{-\left(\frac{R_t}{200}\right)^2}\right] \tag{2.20}$$

with $T = \left[\max(k/\varepsilon, C_t\sqrt{\mu/\varepsilon})\right]$, $Re_\varepsilon = (\nu\varepsilon)^{1/4} y/\nu$ and $R_t = k^2/\nu\varepsilon$.

The main improvement of the AKN model is in the usage of the Kolmogorov velocity scale, u_η $\left[u_\eta \equiv (\upsilon\varepsilon)^{1/4}\right]$ instead of the friction velocity, u_τ, to account for the near-wall and low-Re effects for separated flows [16]. The values of the model coefficients are reevaluated and damping functions are introduced in the dissipation equation and in the definition of the eddy viscosity (μ_t). The introduction of the damping functions ensures two things; one, the effect of the presence of multiple length scales in shear flows are taken care of, and, two, the solution meets the requirement of the near-wall limiting turbulence behavior. Aside from the ability of the AKN model to predict separating and reattaching flows, the model has been shown to provide good predictions of heat transfer [32] as well as low-pressure turbine aerodynamics [33].

2.2.2.3 Nonlinear Model $v^2 - f\ k - \varepsilon$ (V2F)

In addition to the equations for turbulent kinetic energy and its dissipation rate, shown in Eqs. 2.16 and 2.17, the V2F model solves for the wall-normal Reynolds stress, v^2 and the elliptic relaxation function, f. Incorporating these equations into the calculation of the turbulent viscosity allows the anisotropic behaviour of turbulence in the near-wall region to be captured while eliminating the need for a wall damping function. The transport equations for the wall-normal stresses v^2 and the elliptic function f are shown below:

$$\frac{\partial}{\partial t}\left(\rho\overline{v^2}\right) + \nabla \cdot \left(\rho\overline{v^2}\overline{u}\right) = \nabla \cdot \left[\left(\mu + \frac{\mu_t}{\sigma_{\overline{v^2}}}\right)\nabla\overline{v^2}\right] + P_{\overline{v^2}} - \frac{6\rho\overline{v^2}\varepsilon}{k} \tag{2.21}$$

$$\nabla \cdot \left(L^2 \nabla f\right) - f + P_f = 0 \tag{2.22}$$

where the turbulent eddy viscosity μ_t and length scale L are

$$\mu_t = \rho \min\left(C_\mu k T, C_{\mu_{v^2}} v^2 T\right) \tag{2.23}$$

$$L = C_L \max\left(\frac{k^{3/2}}{\varepsilon}, C_\eta\left(\frac{\nu^3}{\varepsilon}\right)^{1/4}\right) \tag{2.24}$$

The implementation of the V2F model in STAR-CCM+ uses the modifications of Davidson et al. [34].

2.3 Computational Details

2.3.1 Airfoil Description

Two transonic high pressure airfoils, shown in Fig. 2.1, were taken from the work of Sooriyakumaran [10] and Duan et al. [9]. These proprietary profiles were supplied by Siemens Energy; the cylindrical and axial coordinates of the two profiles are.

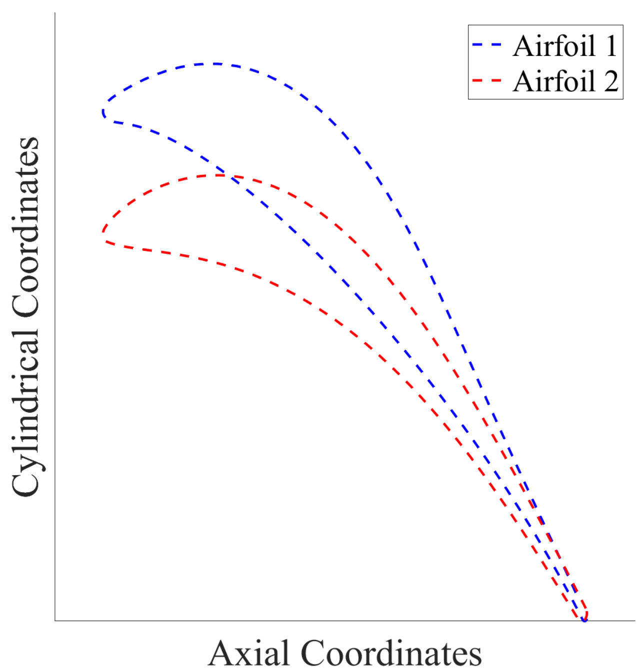

Figure 2.1: Normalized profiles of the two airfoils.

A few notable differences between the profile geometries are shown in Table 2.1. Airfoil 1 has a slightly thinner trailing edge, a much larger throat as well as half the unguided turning angle of airfoil 2. Pitch-to-chord ratios are roughly the same, and the span-to-chord aspect ratios (h/c) are over 1.5, ensuring end-wall effects can be ignored [11] and the midspan flow can be assumed to be fully two-dimensional.

Table 2.1: Geometric parameters.

	Airfoil 1	Airfoil 2
Aspect Ratio, h/c	1.54	1.50
Pitch-to-Chord Ratio, s/c	0.678	0.658
Trailing Edge Blockage, t/o	0.021	0.045
Stagger Angle, ζ	38.6°	27.1°
Unguided Turning Angle, θ_{UG}	4.6°	9.1°

2.3.2 Computational Domain and Grid

Similar to the work of Duan et al. [9], the computational domain was designed as a two-dimensional cascade midspan and is shown in Fig. 2.2. To ensure uniform, fully developed and mixed-out flow, the inlet boundary was placed three axial chord lengths ahead of the leading edge and the outlet boundary was placed seven axial chord lengths behind the leading edge. The top and bottom surfaces, located a half-pitch from the airfoil pressure and suction surfaces, were periodic, and the mesh connectivity was one to one for greater than 99 percent of the boundary surface.

To ensure minimal variance in mixed-out quantities as well as to fully capture the critical flow areas near the airfoil surface, an extensive grid convergence study was preformed. Initially, the near region of the airfoil (one axial-chord-length (C_{ax}) before the leading edge and $2C_{ax}$ behind the leading edge) was isotropically refined. This, as shown in the results section, was not computationally efficient, and even at the highest level of refinement is not grid independent. As one of the major goals of this work was to create an efficient modeling approach for a broad range of flow conditions, an adaptive mesh refinement (AMR) scheme became the most realistic solution.

Two studies were preformed to ensure that the AMR scheme was numerically converged, grid independent and computationally efficient. The first adapted the base level of the isotropic refinement, A0, based on local cell gradients for 1,2,3, 4 and 5 cycles. The lower levels of isotropic refinement, A0-A3, were then adapted for two cycles in an attempt to reduce the number of AMR cycles required for spatial con-

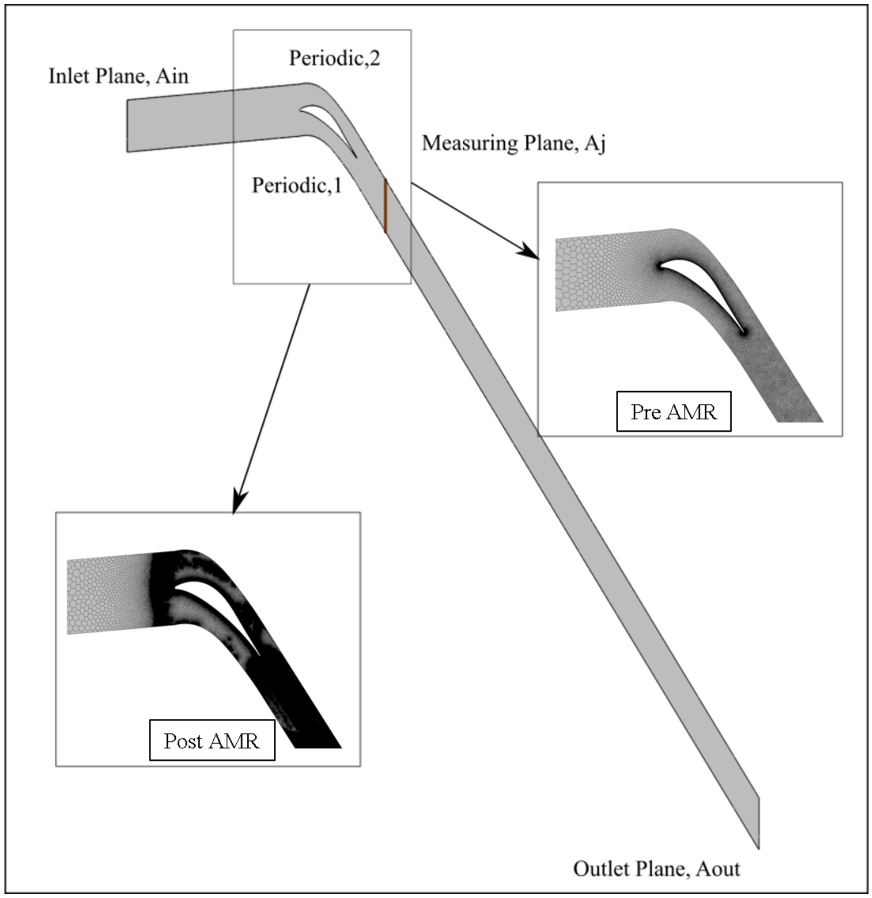

Figure 2.2: Computational domain with and without adaptive mesh refinement (AMR).

vergence. In summary, as will be expanded further in the results section, the A2 isotropic grid adapted for two AMR cycles produced the most efficient computational approach while maintaining grid independence. The conditions used in the refinement procedure is shown below:

$$\text{If} \quad \left|\frac{\nabla\phi}{\phi}\right| > 0.02 \qquad \text{CellArea} \rightarrow \max\left(\frac{A_o}{2}, A_{LPL}\right) \tag{2.25}$$

Here ϕ denotes the scalar quantity of interest (pressure, temperature, density and turbulent kinetic energy), the operator ∇ a local cell gradient, A_o the original cell area prior to adaptation, and A_{LPL} is the area of the last prism layer. This was used as the limiter of refinement to ensure a one to one ratio between the prism layers and the core grid. For clarification, one adaptive cycle begins from a converged simulation (discussed in the next section) is then adapted based on local cell gradients, and rerun to convergence.

2.3.3 Boundary and Initial Conditions

Boundary conditions used in this study replicate the experimental conditions of Sooriyakumaran [10]. The inlet boundary was prescribed a constant total pressure, the outlet a constant static pressure, the top and bottom as periodic surfaces, and the airfoil as a no-slip, adiabatic wall. The inlet total pressure and temperature were different between airfoils but constant across turbulence models; for airfoil 1, $P_{o1} =$ 207 kPa, $T_t = 1008$ K and airfoil 2, $P_{o1} = 170$ kPa, $T_t = 1030$ K. Outlet static pressure was adjusted depending on the desired exit Mach number and was determined from the governing equations of isentropic compressible flow. Turbulence generation was specified at the inlet using an intensity and length scale with $TI\% = 10\%$ and $l = 36$ or 14 mm depending on the airfoil maximum thickness. Reynolds number, based on inlet velocity and true chord, was approximately constant across simulations at $Re_c \sim 1.3 \times 10^6$. Inlet flow direction was specified as the design incidence, $\alpha = 6°$and 9°for Airfoil 1 and Airfoil 2, respectively [10].

The inlet conditions were used to initialize the solution; however, it should be noted that these simulations employed grid sequencing, so how the flow is initialized is not expected to influence the subsequent rate of convergence. After initialization, 10 levels of successively finer grids were solved using a first order invisicid solution algorithm. Each grid level was allowed to either reach convergence (residuals < 0.005) or a maximum number of iterations (200). The solution was then interpolated onto the next finer grid and the process was continued until the finest grid level. This greatly reduced the overall time for convergence.

As mentioned earlier, current CFD predictions will also be validated against the work of Stastny and Safarik [13] which used similar boundary and initial conditions with the exception of the inlet total temperature and pressure, $P_{o1} = 100$ kPa, $T_t = 300$ K.

2.3.4 Solver and Convergence

A coupled, implicit compressible algorithm in steady-state solves the equations for mass, momentum energy. A second-order discretization was used for the source and diffusion terms and a second-order upwind scheme for the convection terms of momentum and turbulence equations. The inviscid, convective fluxes were calculated using the Weiss-Smith preconditioned Roe flux-difference splitting (FDS) scheme. The algebraic multi-grid (AMG) linear solver with a V-cycle, Gauss-Siedel relaxation scheme and bi-conjugate gradient stabilizer acceleration method was employed. For additional information, refer to the manual provided by STAR-CCM+ [30]. All simulations were run until the flow had reached full convergence such that the normalized residuals of all transport quantities dropped at least four order of magnitude and were steady, and the local total pressure loss coefficient did not show fluctuations over 0.0001 for 750 iterations, which typically occurred around 2500 to 3500 iterations depending on turbulence model.

2.4 Results and Discussion

2.4.1 Grid Convergence

Initially it was was believed that grid independent results would be possible using local isotropic refinement within the near region of both airfoils, $1C_{ax}$ upstream and $2C_{ax}$ downstream of the leading edge. Starting with a base simulation of roughly 40,000 cells, the target isotropic cell size was reduced such that the total cell count would approximately double. The distribution of prism layers normal to the surface of the airfoil remained constant (40 prism layers, hyperbolic growth rate, near wall thickness achieving a max $y^+ < 0.5$, and a total thickness $= 0.4t$) only the distribution along the tangential direction of the airfoil surface was changed to maintain an aspect ratio less than two.

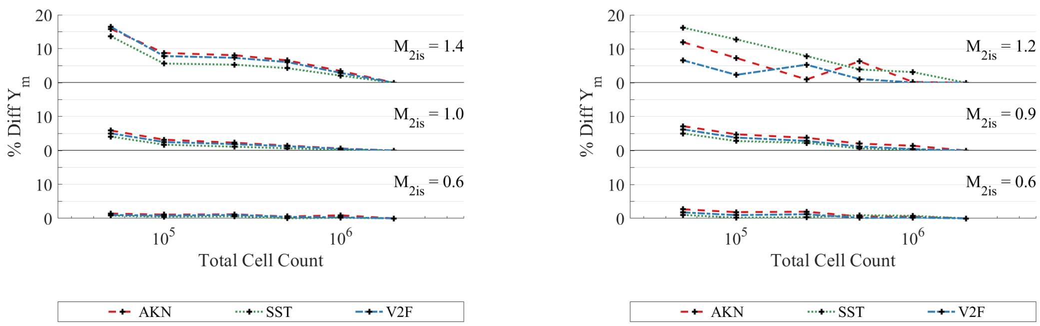

(a) Airfoil 1

(b) Airfoil 2

Figure 2.3: Convergence of mixed-out total pressure loss for different Mach number without AMR.

As shown in Fig. 2.3, grid convergence is highly sensitive to exit Mach number while fairly consistent between turbulence models. At lower exit Mach numbers, both airfoils reach grid independent results, defined as a variance in total mixed-out loss coefficient of less than 1%, by the third level of isotropic refinement A3 or ∼300,000 cells. As exit Mach number is increased, however, grid independence becomes more difficult to obtain. Shown for the highest levels of exit Mach number, both airfoils have a variation of roughly 5% between the A4 and A5 grid levels. This was considered as insufficient to provide verified grid independent results. Therefore, to ensure an accurate and efficient computational model, it was concluded that adaptive mesh refinement (AMR) was the most logical approach.

Two studies were preformed to ensure the AMR scheme was computationally efficient and grid independent. The first adapted a base isotropic mesh, A0, for 1, 2, 3, 4 and 5 cycles in an effort to determine the limit of the effectiveness of the AMR scheme. Effectiveness here is defined as the ability of the AMR scheme to improve the simulation through an adaptive cycle. As cycles were preformed, less cells required refinement; therefore, further AMR cycles became ineffective if there were no cells to be refined. To monitor this, the percentage of flagged (or to be refined cells) to total cells was tracked. If this percentage fell below 1% the AMR scheme was deemed ineffective and unnecessary. At lower Mach numbers with no major shock presence, AMR cycles were ineffective and unnecessary; for higher Mach numbers with multiple shocks, it was seen that 4 or 5 passes were needed to achieve the desired limit.

The second study was geared towards two objectives: 1) to ensure no quantities influencing the total pressure loss were missed during adaptation and 2) to improve the efficiency of the overall AMR process by reducing the total number of required cycles. To do so the lower levels of isotropic refinement, A0-A4, were adapted for two cycles. The results of the change in mixed-out loss coefficient for this investigation are shown in figure 2.4.

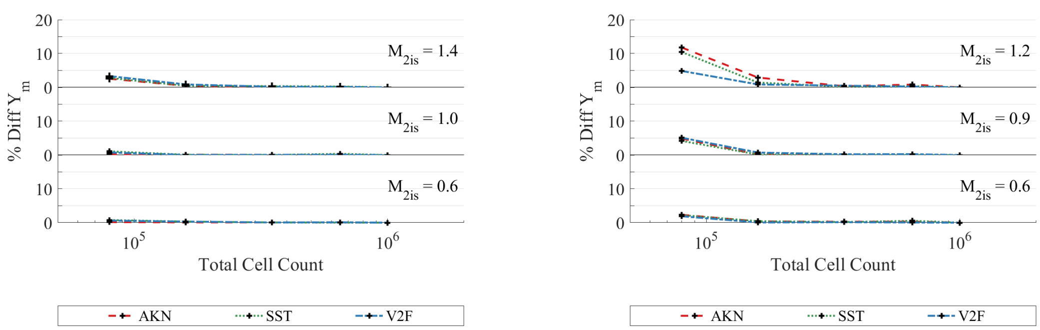

(a) Airfoil 1 (b) Airfoil 2

Figure 2.4: Convergence of mixed-out total pressure loss for different Mach number with AMR.

As a reminder, one adaptive cycle begins from a converged simulation, is then adapted based on local cell gradients (Eq. 2.25), and rerun to convergence. The results show that two levels of refinement, using the A2 isotropic grid as a starting point, ensured a variance of less than 1% for the total mixed-out loss coefficient and that the simulations were adequately, spatially converged. Therefore, this procedure was used for each simulation hereafter.

2.4.2 Solution Validation

2.4.2.1 Comparison to Sooriyakumaran

As a means to validate the simulation methodology, computationally predicted values were compared to the experimental work of Sooriyakumaran [10]. Figure 2.5 shows the experimental and computational mixed-out total pressure loss coefficients for each airfoil at design incidence.

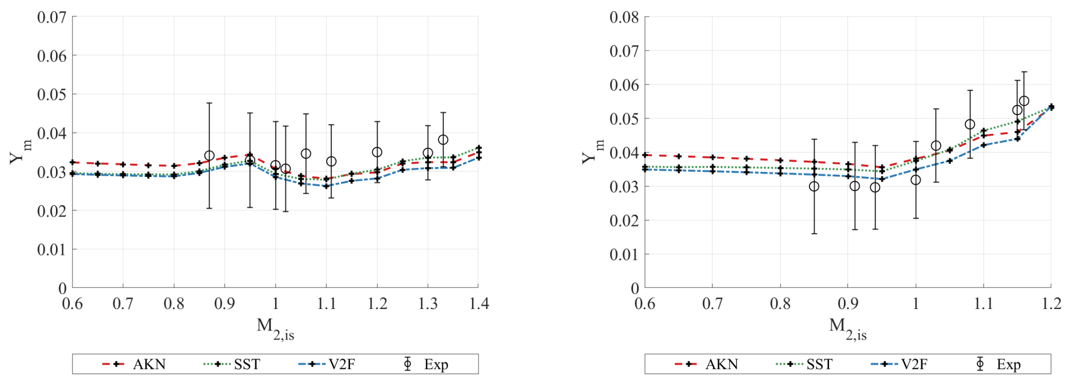

(a) Airfoil 1

(b) Airfoil 2

Figure 2.5: Mixed-out total pressure loss (Y_m) over exit Mach number at design incidence.

Results indicate, as anticipated from Duan et al. [9], that RANS modeling is successful, to a reasonable accuracy, in determining the loss variation over exit isentropic Mach number for these airfoils. Although all results lie within the experimental uncertainty, discrepancies between models are still somewhat significant, specifically between SST and AKN at subsonic exit Mach numbers, and SST and V2F at supersonic exit Mach numbers. Shown in Fig. 2.6 is a comparison of the percent difference of predicted total pressure loss coefficient relative to the SST model for airfoils 1 and 2; AKN is shown in red and V2F in blue. As exit Mach number is increased, the V2F model steadily deviates from the SST predictions, while the AKN model displays more of a parabolic trend, with larger deviation in both the subsonic and supersonic regimes. In addition, the V2F model displays the most dependence on airfoil geom-

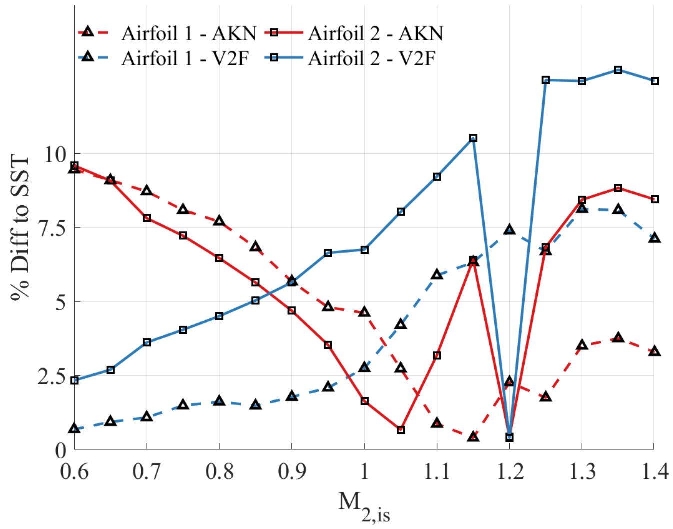

Figure 2.6: Percent difference of mixed-out total pressure loss (Y_m) between models compared to SST.

etry, seen by the consistent deviation over exit Mach contrary to the AKN model. As the airfoil profile becomes more aggressive, a higher sensitivity to the turbulence model choice is seen in the prediction of total pressure loss.

Figure 2.7 compares the computationally predicted surface distributions of isentropic Mach number compared to the work of Sooriyakumaran for airfoil 2. It was found that the distribution was captured well for all models, with the exception of the slight offset along the suction surface. This deviation was consistent across turbulence models, grid resolution, as well as slight deviation of incidence ($\pm 5°$).

2.4.2.2 Comparison to Stastny and Safarik

Due to the deviation of the simulation results from experiment along the suction surface of the second airfoil, a comparison to the work of Stastny and Safarik [13] was used to further validate the simulation methodology. Fig. 2.8 presents the results of the comparison, indicating good agreement along both the suction and pressure surfaces. There is, however, a slight difference in the prediction of the influence of the shock on the suction surface at $\sim 0.8C_{ax}$. This is believed to be caused by how each

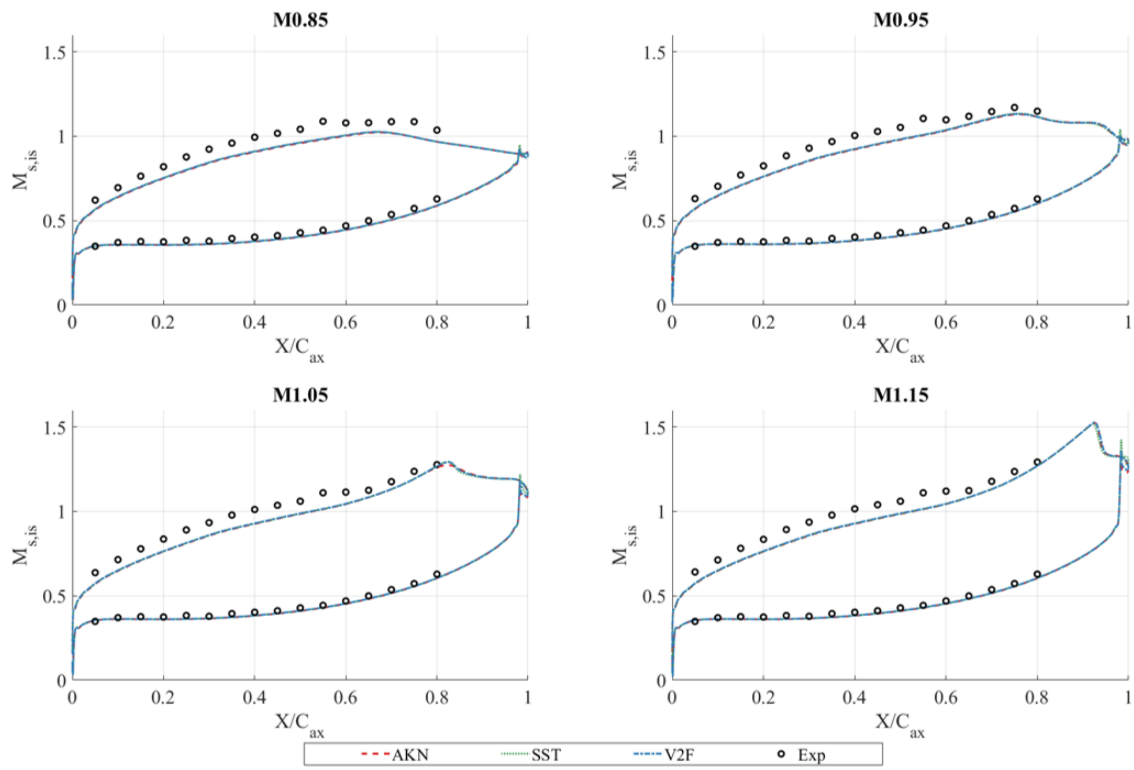

Figure 2.7: Surface isentropic Mach number ($M_{s,is}$) distributions for Airfoil 2 compared to CFD.

model is predicting the shock-boundary interaction. As a reminder, the conditions of this comparison were similar to the previous airfoils with the exception of the inlet total temperature and pressure, $P_{o1} = 100$ kPa, $T_t = 300$ K.

2.4.3 Turbulence Model Effects

2.4.3.1 Mixed-Out Pressure Loss Coefficient

Shown in Fig. 2.9 are downstream pitchwise distributions of the local total pressure loss for airfoil 1. Results indicate a strong lack of mixing within the simulations; both the AKN and V2F models greatly under predict the amount of diffusion within the wake while the SST model, although still showing a high pressure deficit compared to experiment, shows a slightly better prediction. This trend is exemplified as the exit Mach number is increased. Each model is able to capture a reduction in total loss; however, the relative reduction compared to experiment is significantly less.

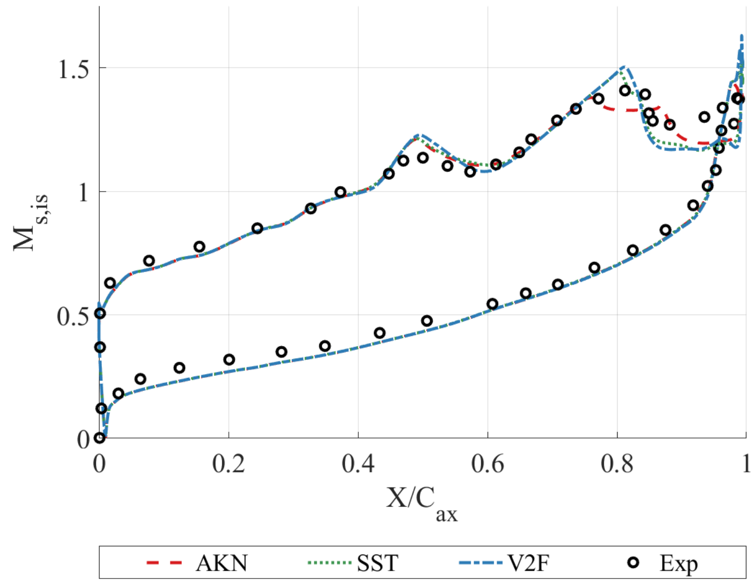

Figure 2.8: Surface isentropic Mach number ($M_{s,is}$) distributions for Airfoil 3 compared to CFD.

The airfoil shape has a noticeable influence on the ability of each turbulence model to accurately predict the total pressure loss within the wake. Duan et al. [9] provides a detailed description of the shock structures of these two airfoils for a broad range of exit Mach numbers. Figure 2.10 shows that for lower exit Mach numbers, airfoils with higher blockage ratios provide a better prediction of total pressure loss. As exit Mach number is increased and the shock more pronounced, overall prediction of pressure loss is significantly reduced.

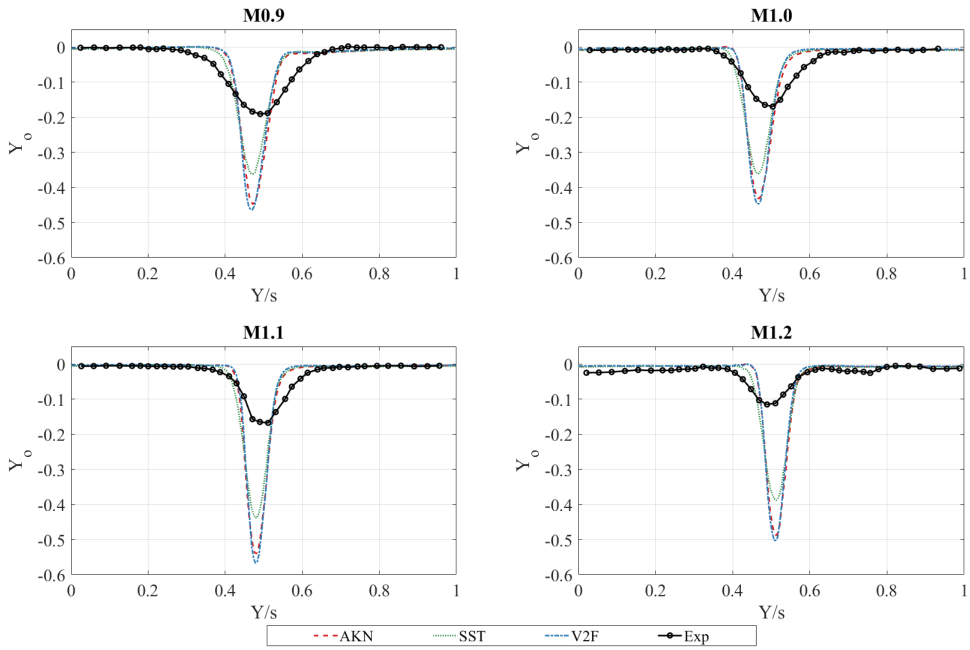

Figure 2.9: Pitchwise variation of total pressure loss coefficient (C_{po}) for Airfoil 1.

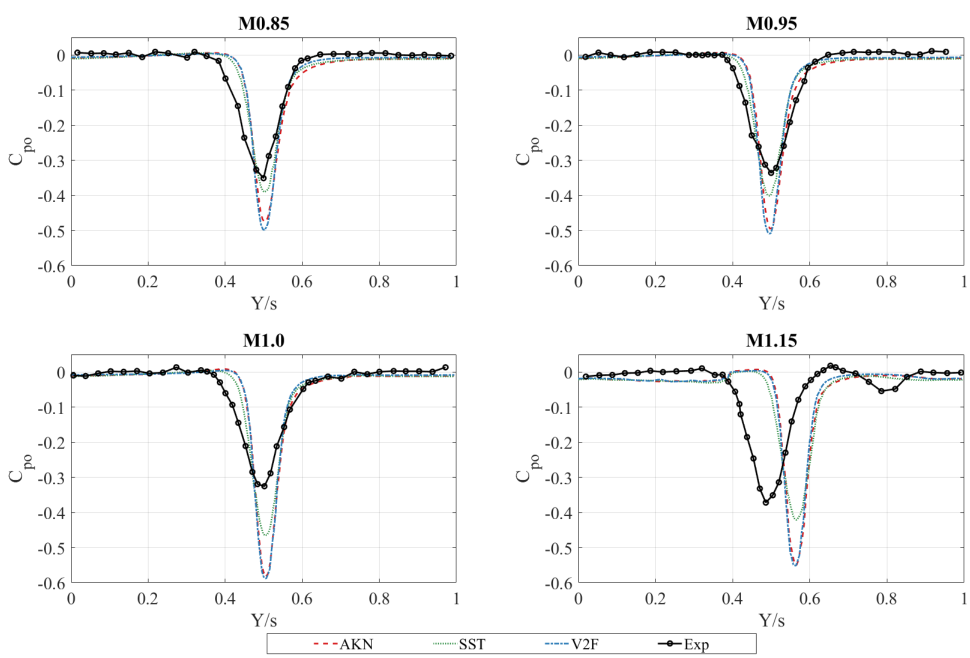

Figure 2.10: Pitchwise variation of total pressure loss coefficient (C_{po}) for Airfoil 2.

2.4.3.2 Surface Distributions

The surface isentropic Mach number distributions for airfoil 1 at increasing exit Mach numbers is shown in Fig. 2.11. For subsonic exit conditions, surface distributions across turbulence models are identical, as exit Mach number increases predictions of the latter portion of the suction surface begin to deviate slightly amongst models, depiction of the shock specifically.

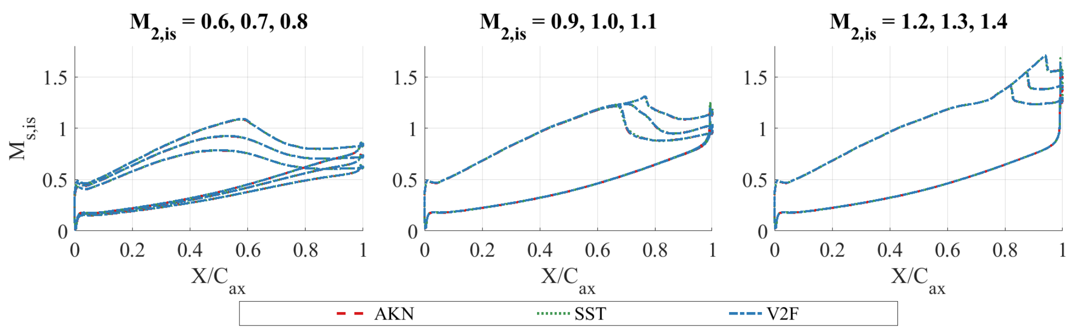

Figure 2.11: Surface isentropic Mach number ($M_{s,is}$) distributions for Airfoil 1.

Figure 2.12 shows a highlighted view of the surface Mach distributions for the second half of the airfoil 1. For an exit Mach number of 0.9 (Fig. 2.12b) the SST model, similar to what was seen in the wake only with less significance, begins to smear the influence of the shock. As the exit Mach number is increased and the shock presence within the vane more pronounced, the smearing length along the airfoil surface is reduced. Overall the distributions between models are near identical.

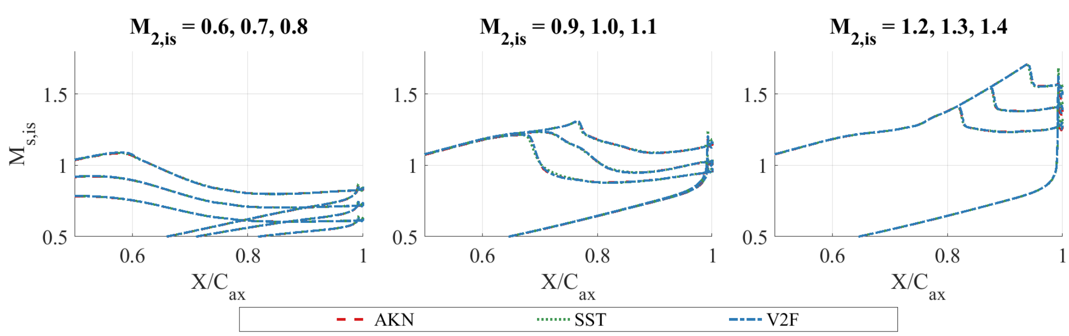

Figure 2.12: Surface isentropic Mach number ($M_{s,is}$) distributions for Airfoil 1 at suction peak.

Airfoil 2 surface pressure distributions show a similar trend (Fig. 2.13); with the minor exception to the shock, predictions are near identical between turbulence models for this range of conditions.

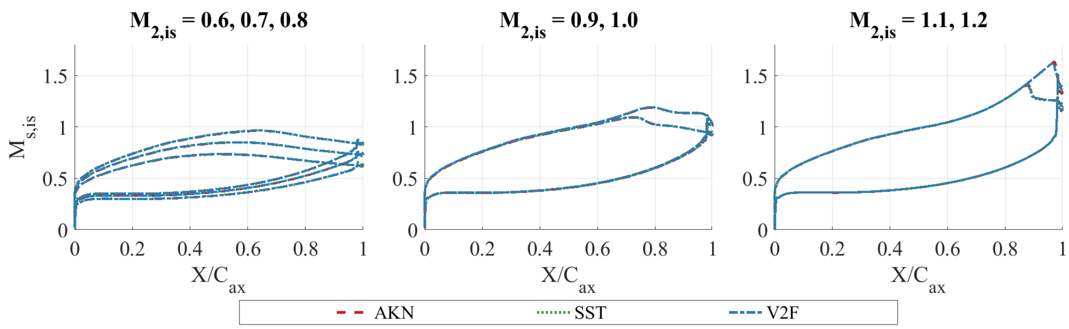

Figure 2.13: Surface isentropic Mach number ($M_{s,is}$) distributions for Airfoil 2.

2.4.3.3 Shock Location and Wake Size

Prediction of the magnitude and position of the oblique shock caused by the expansion of the pressure and suction flows around the trailing edge is critical to the calculation of total pressure loss. Figure 2.14 shows a comparison of predicted density distributions near the surface of airfoil 1 for exit Mach numbers of 0.6, 1.0 and 1.4. As seen, results are nearly identical for all cases.

As shown in Fig. 2.13, the prediction of the shock location on the suction surface is highly dependent on exit Mach number. Figure 2.15 shows the density contours for the second airfoil at exit Mach numbers of 0.8, 1.0 and 1.2. The most notable difference is seen for an exit Mach number of 1.2, in which both $k-\varepsilon$ models predict the shock missing the suction surface of the adjacent airfoil. This is believed to be a nonphysical result, potentially caused by the differences in how each model predicts separation and reattachment, turbulent production, skin friction and the Reynolds stresses; a detailed analyses on these is reserved as a future work.

2.5 Conclusion

The results from three steady-state RANS eddy viscosity turbulence models were analyzed to investigate their ability to predict the total pressure loss for two transonic, high pressure turbine airfoils. First, it was found that to obtain grid independent results an adaptive mesh refinement scheme based on the local cell gradients of density, temperature, pressure and turbulent kinetic energy is recommended. This greatly reduced the computational cost of each simulation, eliminating over refinement in areas of low gradients while refining in areas of high gradients. This recommendation applies to all three turbulence models investigated here, the degree of influence of the refinement procedure has been reviewed and was shown to be fairly consistent across models. Simulation methodology has been verified through comparison to experimental rig test results. It was shown that each model predicted mixed-out total pressure loss within the error of the experiment. Surface pressure distributions and density contours were compared for airfoil 1 and airfoil 2, showing no dominant model prediction over the next. Both $k-\varepsilon$ turbulence models showed nonphysical predictions of the airfoil 2 trailing edge shock for an exit Mach number of $M_{2,is} = 1.2$. Additional analysis of the surface normal distributions of turbulent kinetic energy, eddy viscosity and pressure ratio can provide insight into the exact mechanisms creating the differences seen at higher exit Mach numbers. In conclusion, all models predict the flow within two transonic, high pressure airfoils with similar degrees of accuracy; the shear-stress transport $k-\omega$ with $\gamma{-}\mathrm{Re}_\theta$ transition model is perhaps more reliable given the more realistic flow prediction of airfoil 2 at higher Mach numbers, attributed to the ability of the model to maintain the location of the shock on the suction surface.

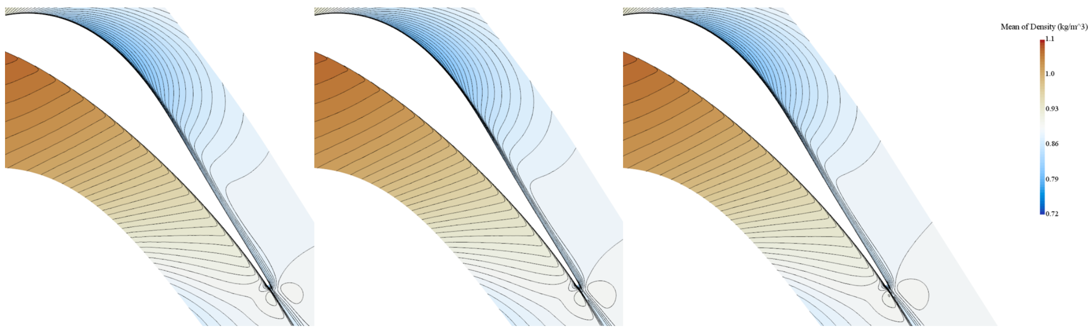

(a) $M_{2,is} = 0.6$

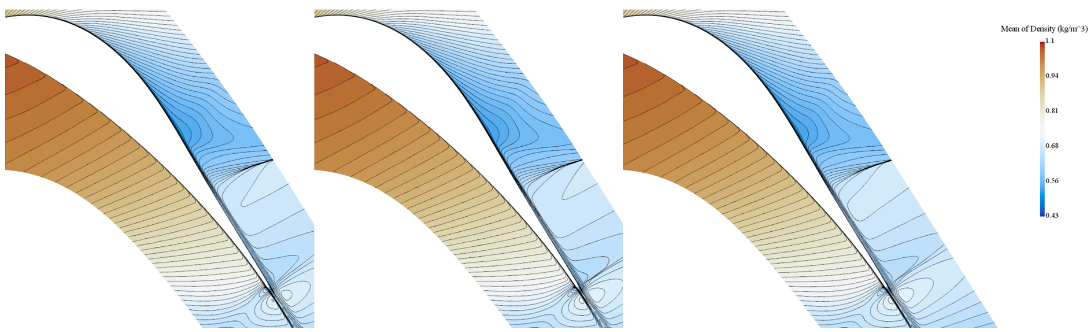

(b) $M_{2,is} = 1.0$

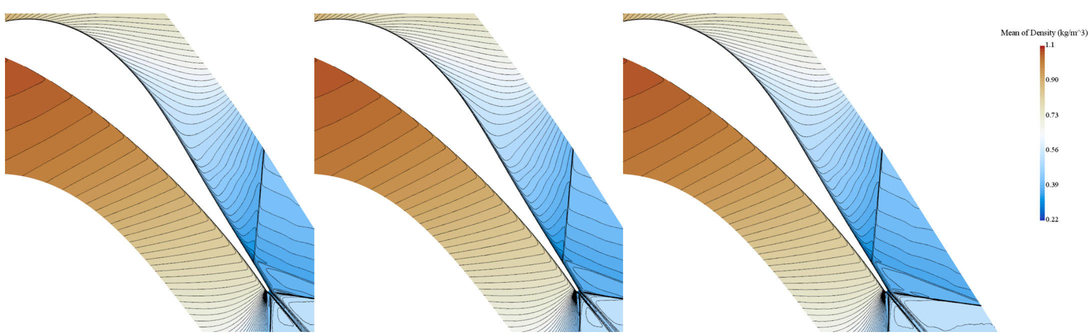

(c) $M_{2,is} = 1.4$

Figure 2.14: Averaged density contours for Airfoil 1 at exit Mach numbers: $M_{2,is} = 0.6, 1.0, 1.4$. Shown from left to right: AKN, SST, V2F

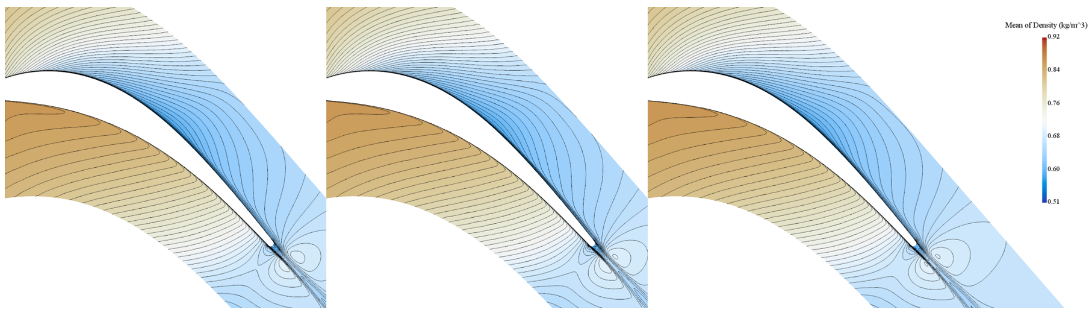

(a) $M_{2,is} = 0.8$

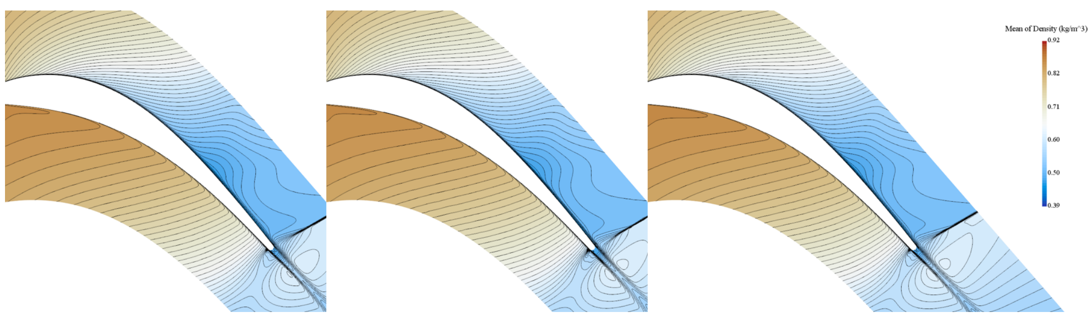

(b) $M_{2,is} = 1.0$

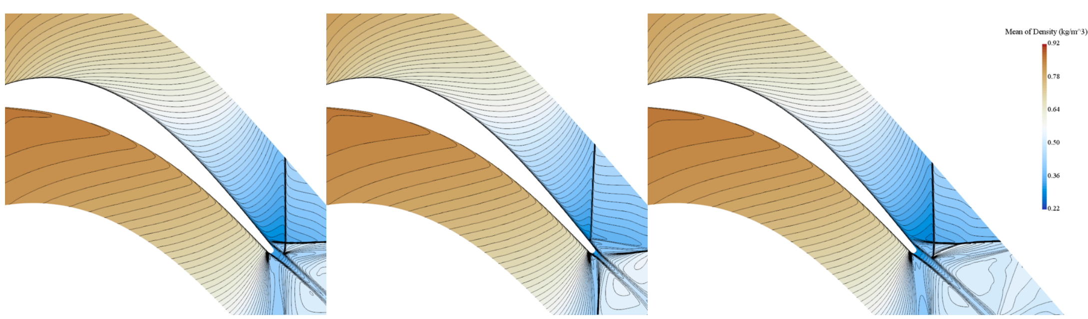

(c) $M_{2,is} = 1.2$

Figure 2.15: Averaged density contours for Airfoil 2 at exit Mach numbers: $M_{2,is} = 0.8, 1.0, 1.2$. Shown from left to right: AKN, SST, V2F

REFERENCES

[1] H. Hoheisel, R. Kiock, H.-J. Lichtfuss, and L. Fottner, "Influence of free stream turbulence and blade pressure gradient on boundary layer and loss behaviour of turbine cascades," in *ASME 1986 International Gas Turbine Conference and Exhibit*, pp. V001T01A102–V001T01A102, American Society of Mechanical Engineers, 1986.

[2] L. Xu and J. Denton, "The base pressure and loss of a family of four turbine blades," *Journal of turbomachinery*, vol. 110, no. 1, pp. 9–17, 1988.

[3] D. Mee, N. Baines, M. Oldfield, and T. Dickens, "An examination of the contributions to loss on a transonic turbine blade in cascade," in *ASME 1990 International Gas Turbine and Aeroengine Congress and Exposition*, pp. V005T16A012–V005T16A012, American Society of Mechanical Engineers, 1990.

[4] J. D. Denton, "Loss mechanisms in turbomachines," in *ASME 1993 International Gas Turbine and Aeroengine Congress and Exposition*, pp. V002T14A001–V002T14A001, American Society of Mechanical Engineers, 1993.

[5] R. E. Mayle, "The role of laminar-turbulent transition in gas turbine engines," in *ASME 1991 International Gas Turbine and Aeroengine Congress and Exposition*, pp. V005T17A001–V005T17A001, American Society of Mechanical Engineers, 1991.

[6] V. Michelassi, W. Rodi, and P.-A. Giess, "Experimental and numerical investigation of boundary-layer and wake development in a transonic turbine cascade," in *ASME 1997 International Gas Turbine and Aeroengine Congress and Exhibition*, pp. V001T03A095–V001T03A095, American Society of Mechanical Engineers, 1997.

[7] M. G. Dunn, "Convective heat transfer and aerodynamics in axial flow turbines," in *ASME Turbo Expo 2001: Power for Land, Sea, and Air*, pp. V004T06A001–V004T06A001, American Society of Mechanical Engineers, 2001.

[8] G. A. Ledezma, G. M. Laskowski, and A. K. Tolpadi, "Turbulence model assessment for conjugate heat transfer in a high pressure turbine vane model," in *ASME Turbo Expo 2008: Power for Land, Sea, and Air*, pp. 489–499, American Society of Mechanical Engineers, 2008.

[9] P. Duan, C. S. Tan, A. Scribner, and A. Malandra, "Loss generation in transonic turbine blading," *Journal of Turbomachinery*, vol. 140, no. 4, p. 041006, 2018.

[10] C. Sooriyakumaran, "Experimental study of profile losses in three transonic turbine cascades," masters thesis, Carelton University, 2014.

[11] D. Corriveau and S. Sjolander, "Influence of loading distribution on the performance of transonic high pressure turbine blades," *Journal of Turbomachinery(Transactions of the ASME)*, vol. 126, no. 2, pp. 288–296, 2004.

[12] F. Taremi, *Endwall flows in transonic turbine cascades.* PhD thesis, Carleton University, 2013.

[13] M. Šťastnỳ and P. Šafařík, "Experimental analysis data on the transonic flow past a plane turbine cascade," in *ASME 1990 International Gas Turbine and Aeroengine Congress and Exposition*, pp. V001T01A098–V001T01A098, American Society of Mechanical Engineers, 1990.

[14] W. Rodi, "European research community on flow, turbulence and combustion."

[15] F. R. Menter, R. B. Langtry, S. Likki, Y. Suzen, P. Huang, and S. Völker, "A correlation-based transition model using local variables - part 1: model formulation," *Journal of Turbomachinery*, vol. 128, no. 3, pp. 413–422, 2006.

[16] K. Abe, T. Kondoh, and Y. Nagano, "A new turbulence model for predicting fluid flow and heat transfer in separating and reattaching flows. - 1. flow field calculations," *International journal of heat and mass transfer*, vol. 37, no. 1, pp. 139–151, 1994.

[17] P. A. Durbin, "Separated flow computations with the k-epsilon-v-squared model," *AIAA journal*, vol. 33, no. 4, pp. 659–664, 1995.

[18] R. J. Kind, P. J. Serjak, and M. W. Abbott, "Measurements and prediction of the effects of surface roughness on profile losses and deviation in a turbine cascade," in *ASME 1996 International Gas Turbine and Aeroengine Congress and Exhibition*, pp. V001T01A067–V001T01A067, American Society of Mechanical Engineers, 1996.

[19] P. Ligrani, "Aerodynamic losses in turbines with and without film cooling, as influenced by mainstream turbulence, surface roughness, airfoil shape, and mach number," *International Journal of Rotating Machinery*, vol. 2012, 2012.

[20] M. Oldfield, D. Schultz, and J. Nicholson, "Loss measurements using a fast traverse in an ilpt transient cascade(isentropic light piston cascade tunnel)," *Measuring techniques in transonic and supersonic flows in cascades and turbomachines*, pp. 17–1, 1982.

[21] J. Amecke and P. Šafařik, *Data Reduction of Wake Flow Measurements with Injection of an Other Gas.* Deutsche Forschungsanstalt für Luft- und Raumfahrt Köln: Forschungsbericht, DLR, Abt. Operative Planung, 1995.

[22] Q. Zhang, D. Sandberg, and P. M. Ligrani, "Mach number and freestream turbulence effects on turbine vane aerodynamic losses," *Journal of propulsion and power*, vol. 21, no. 6, pp. 988–996, 2005.

[23] J. Denton and L. Xu, "The trailing edge loss of transonic turbine blades," in *ASME 1989 International Gas Turbine and Aeroengine Congress and Exposition*, pp. V001T01A097–V001T01A097, American Society of Mechanical Engineers, 1989.

[24] C. Atkin and C. SQUIRE, "A study of the interaction of a normal shock wave with a turbulent boundary layer at mach numbers between 1. 30 and 1. 55," *European Journal of Mechanics, B/Fluids*, vol. 11, no. 1, pp. 93–118, 1992.

[25] C. Graham and F. Kost, "Shock boundary layer interaction on high turning transonic turbine cascades," in *ASME 1979 International Gas Turbine Conference and Exhibit and Solar Energy Conference*, pp. V01AT01A037–V01AT01A037, American Society of Mechanical Engineers, 1979.

[26] J. Délery, J. G. Marvin, and E. Reshotko, "Shock-wave boundary layer interactions," tech. rep., Advisory Group for Aerospace Research and Development Neuilly-sur-Seine (France), 1986.

[27] Z. Wang, Z. Liu, and Z. Feng, "Influence of mainstream turbulence intensity on heat transfer characteristics of a high pressure turbine stage with inlet hot streak," *Journal of Turbomachinery*, vol. 138, no. 4, p. 041005, 2016.

[28] D. C. Wilcox *et al.*, *Turbulence modeling for CFD*, vol. 2. DCW Industries La Canada, CA, 1998.

[29] F. R. Menter, "Two-equation eddy-viscosity turbulence models for engineering applications," *AIAA journal*, vol. 32, no. 8, pp. 1598–1605, 1994.

[30] Siemens, "Star-ccm+ user manual," 2021. Last accessed 10 Oct. 2021.

[31] F. Menter and M. Kuntz, "Adaptation of eddy-viscosity turbulence models to unsteady separated flow behind vehicles," in *The aerodynamics of heavy vehicles: trucks, buses, and trains*, pp. 339–352, Springer, 2004.

[32] A. A. Igci and M. E. Arici, "A comparative study of four low-reynolds-number k-ε turbulence models for periodic fully developed duct flow and heat transfer," *Numerical Heat Transfer, Part B: Fundamentals*, vol. 69, no. 3, pp. 234–248, 2016.

[33] B. M. Arko and M. McQuilling, "Computational study of high-lift low-pressure turbine cascade aerodynamics at low reynolds number," *Journal of Propulsion and Power*, vol. 29, no. 2, pp. 446–459, 2013.

[34] L. Davidson, P. Nielsen, and A. Sveningsson, "υ2- f modifications of the υ2- f model for computing the flow in a 3d wall jet, turbulence," *Heat Mass Transfer*, vol. 4, pp. 577–584, 2003.

CHAPTER 3: (PAPER 2) EFFECT OF INFLOW CONDITIONS ON TRANSONIC TURBINE AIRFOIL LIMIT LOADING

3.1 Introduction

One of the primary objectives in gas turbine engineering is to maximize the total work output of a turbine stage through a combination of airfoil design and pressure ratio. As the pressure ratio across a specific stage is increased beyond critical, where the axial Mach number equals unity at the throat, a Prandtl-Meyer expansion around the trailing edge causes the exit Mach number to become supersonic [1]. As the pressure ratio is further increased this expansion process creates an upper limit to the tangential velocity within the blade passage leading to a limit on the force which the airfoil can produce, defined as airfoil limit loading [2]. Although additional work may be extracted by increasing the mass flow rate through the turbine, this requires a significant increase in inlet total pressure leading to a large drop in turbine efficiency, which is not desirable.

Airfoil limit loading was first documented in a National Advisory Committee for Aeronautics (NACA) Research Memorandum in the early 1950's [3, 4]. It was shown that the airfoil outlet metal angle was the dominant geometric factor to influence the point of limit loading. Since then numerous studies have proposed numerical methods to predict the pressure ratio required to reach limit loading [2, 1, 5] to name a few. Although these methods predict the onset of limit loading fairly well there has yet to be a robust method that provides detailed flow characteristics [6]. Computational fluid dynamics (CFD) provides the gas turbine community with an efficient and reliable method to analyze this condition allowing for a better understanding of the overall flow, potentially extending a turbine airfoil design envelope and reducing the

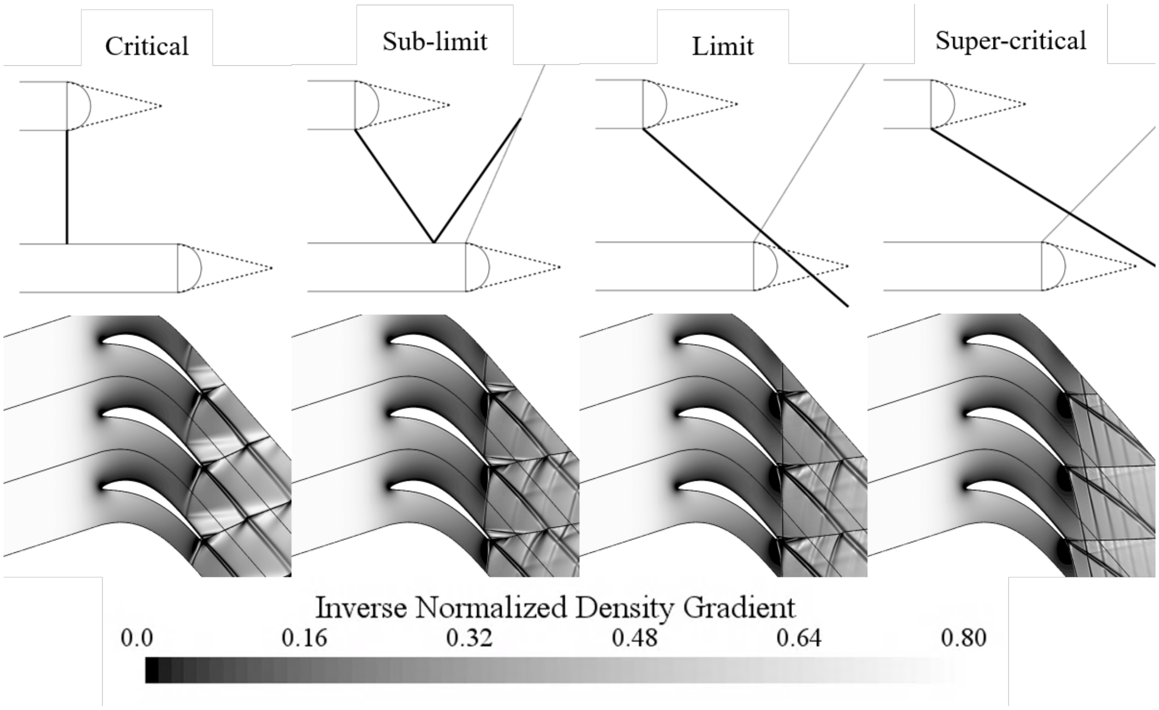

Figure 3.1: Stages to limit loading: terminology.

total number of stages required to produce a specific power demand.

Presented in Figure 3.1 is the terminology used to describe the various stages of airfoil limit loading. The left most image shows the critical loading condition, defined as the onset of choking within the blade passage. The bold solid line represents the throat or region where the flow has reached Mach one. As the pressure ratio is increased a pressure surface shock, caused by the Prandtl-Meyer expansion near the trailing edge, impinges on the suction surface of the adjacent airfoil, referred to as the sub-limit loading period as it spans over a range of pressure ratios. Further increase of the pressure ratio moves the pressure surface shock past the trailing edge and into the base pressure region, shown with a dotted line. This is defined as airfoil limit loading as the flow upstream of the shock is fully choked resulting in a limit to the maximum blade force. Given the complex flow conditions at the trailing edge caused by unsteady trailing edge vortex shedding and subsequent interaction with shock structures this is difficult to predict computationally [7]. Super-critical loading is the fourth and final stage, with the trailing edge pressure surface shock completely departing the base pressure region and the flow within the passage becoming completely choked.

Modern compressible flow theory states that for a convergent-divergent nozzle, similar to the passage between two airfoils, the point at which choking occurs is solely dictated by the area and pressure ratio of the nozzle [8]. Although this provides a good estimate of the general flow features for a simple system, these formulations assume the flow to be quasi-one dimensional and include no influence of turbulence variation. The flow within a turbine passage, specifically during ramping procedures experiences a wide range of both incidence and turbulence variation [9]. This is not included in these assumptions; therefore, it is unclear how these will affect the onset of choking or limit loading.

The purpose of this work is to 1. investigate and determine the sensitivities of inflow conditions on airfoil limit loading characteristics and 2. provide a detailed analysis of the entire flow domain during limit loading for a set of four different transonic turbine airfoils. Focus is given to the potential boundary conditions exhausted by a combustor; variation of inlet flow angle and turbulence quantities: intensity and length scale.

All simulations presented in this paper were performed using a commercial finite volume code, StarCCM+, with the shear-stress transport (SST) $k-\omega$ with γ transition (Menter et al. [10]) steady-state Reynolds-Averaged Navier-Stokes (RANS) eddy viscosity turbulence model. Quantitative data of mass-flow averaged Mach numbers, mass-flow averaged flow angles, surface isentropic Mach number distributions and mass-flow averaged total pressure loss coefficients were collected and are presented alongside flow visualizations of numerical Schlieren images to provide insight into the influence of inflow conditions on airfoil limit loading.

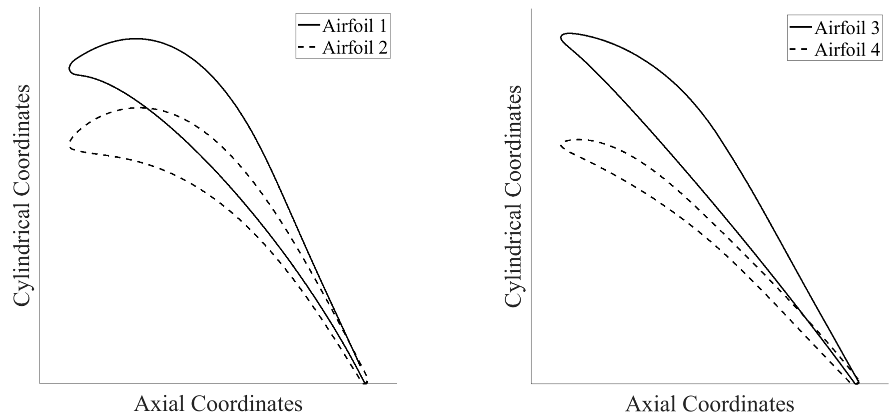

(a) AIRFOILS 1 & 2

(b) AIRFOILS 3 & 4

Figure 3.2: Airfoil normalized profiles.

3.2 Simulation Setup

The simulation methodology was previously validated using data collected at the Pratt & Whitney Canada (PWC) high-speed wind tunnel (HSWT) at Carleton University in Ottawa, Canada by Sooriyakumaran [11]. For a detailed description of the validation process or the wind tunnel apparatus, the reader is referred to the work of Owen [12] and Taremi [13] respectively.

3.2.1 Airfoil Description

Four transonic airfoils, shown in Figure 3.2, were taken from the work of Sooriyakumaran [11]. The purpose of using these airfoils is that they have a broad range of variability allowing for an adequate test bank for this investigation. These proprietary profiles were supplied by Siemens Energy, Inc.

A few notable differences between the profile geometries are shown in Table 3.1. Airfoils 1 and 3 have slightly thinner trailing edges as well as much larger throats compared to airfoils 2 and 4. The unguided turn angle of airfoil 1 is much smaller than the other airfoils with airfoil 4 having nearly three times more turning. The stagger angle of airfoil 2 is roughly half airfoil 4 and the pitch-to-chord ratio of airfoils

1 and 2 are much smaller than airfoils 3 and 4. Lastly the airfoils span-to-chord aspect ratios (h/C_t) for wind-tunnel testing were over 1.5, ensuring end-wall effects could be ignored [14] and the midspan flow assumed to be fully two-dimensional.

Table 3.1: Airfoil geometric parameters.

Airfoil	1	2	3	4
Aspect Ratio, h/C_t	1.54	1.50	1.54	1.77
Pitch-to-Chord Ratio, s/C_t	0.678	0.658	0.843	1.072
Blockage Ratio, t/o	0.021	0.045	0.024	0.035
Stagger Angle, ζ	39°	27°	60°	49°
Inlet Metal Angle, β_1	6°	18°	−32°	−13°
Outlet Metal Angle, β_2	−58°	−49°	−66°	−58°
Unguided Turning, θ_{UG}	5°	9°	10°	14°

3.2.2 Computational Domain and Grid

The computational domain was modeled as a two-dimensional cascade midspan and extends from one and a half axial chord lengths ahead of the leading edge to seven axial chord lengths behind the trailing edge, shown in Figure 3.3. The inlet boundary location was selected to ensure fully developed uniform flow and the downstream boundary was located an adequate distance away from the airfoil to ensure no shock reflections were felt in the predictions as well as to observe the effects of the mixing process within the passage [12]. The top and bottom surfaces located a half-pitch from the airfoil pressure and suction surfaces were periodic and the mesh connectivity was one to one along the periodic interface.

The core mesh comprised an unstructured, polyhedral grid with prismatic layers along the airfoil surface. The distribution of prisms normal to the airfoil remained constant with 40 prism layers, a hyperbolic growth rate, a near wall thickness achieving a max $y^+ < 0.5$, and a total thickness = 0.4t. The distribution along the tangential direction of the airfoil surface was changed with increasing refinement to maintain an aspect ratio of less than two.

To ensure minimal numerical variance in mixed-out quantities as well as to fully

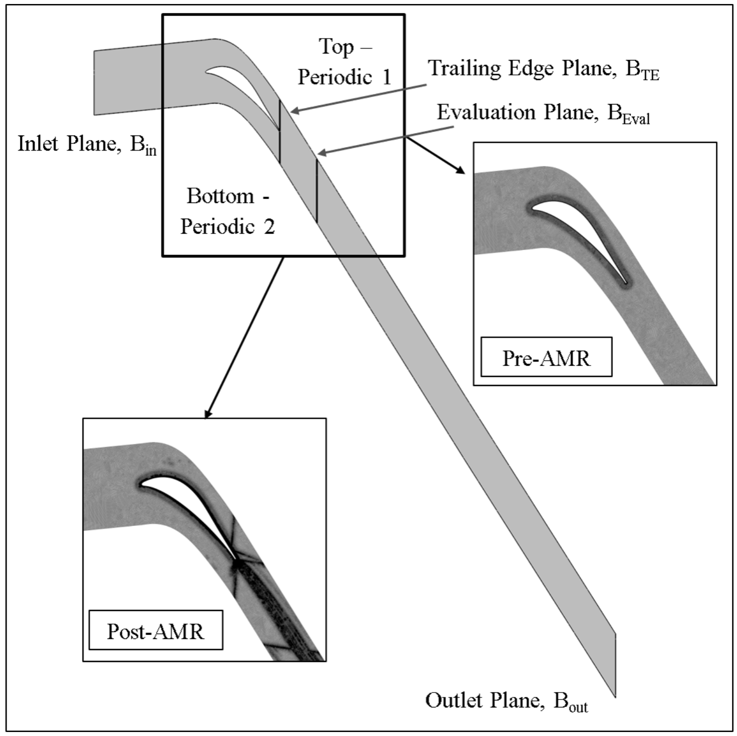

Figure 3.3: Computational domain and grid.

capture the critical flow areas near the airfoil surface, an extensive grid convergence study was preformed [12]. Initially, the near region of the airfoil (one axial-chord-length (C_x) before the leading edge and 2.5 C_x behind the leading edge) was isotropically refined. However, as the pressure ratio was increased this mesh refinement approach resulted in a very high computational cost and at the finest level of refinement did not produce a grid independent solution, defined as a variance in mixed-out total pressure loss coefficient of less than 1%. Therefore, an adaptive mesh refinement (AMR) scheme was selected to achieve the desired grid independent solution with minimum computational effort.

$$\text{If} \quad \left|\frac{\nabla\phi}{\phi}\right| > 0.02 \quad \text{Area} \rightarrow \max\left(\frac{A_o}{2}, A_{LPL}\right) \tag{3.1}$$

Equation 3.1 shows the governing process of the AMR scheme. Here ϕ denotes the scalar quantity of interest (total pressure, total temperature, density and turbulent kinetic energy), the operator ∇ a local cell gradient, A_o the original cell area prior to adaptation, and A_{LPL} is the area of the last prism layer. This was used as the limiter of refinement to ensure a one to one ratio between the prism layers and the core grid. For clarification, one adaptive cycle begins from a converged simulation, which is then adapted based on local cell gradients, and rerun to convergence.

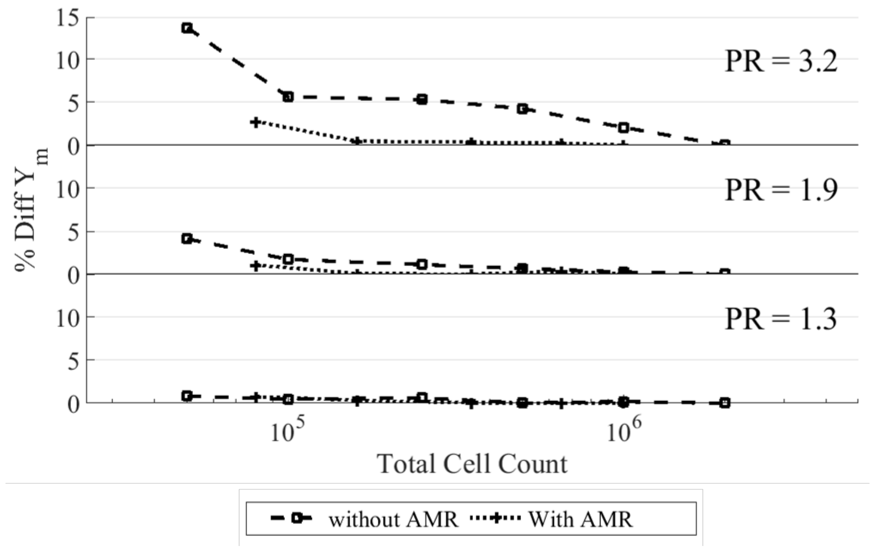

Figure 3.4: Convergence of mixed-out total pressure loss for different pressure ratios - Airfoil 1.

Figure 3.4 shows an example of the grid convergence study employed for each airfoil. A comparison of loss coefficient variance was preformed for each pressure ratio with respect to the finest grid simulated for both the isotropic refinement and adaptive refinement procedures. As can be seen grid convergence is highly sensitive to total pressure ratio. At lower pressure ratios grid independent results are achieved for both the isotropic and adaptive refinement procedures. However, as the pressure ratio is increased grid independence becomes more difficult to obtain. Shown for a high sublimit pressure ratio, is a variation of roughly 4% between the densest isotropic refinements and a variance of less than 1% for the adapted mesh after only two cycles. This provided a saving of roughly 5x in number of total computational cells.

3.2.3 Boundary and Initial Conditions

Boundary conditions for model validation were set to replicate the experimental conditions of Sooriyakumaran [11]. The inlet boundary was prescribed a constant total pressure and total temperature, the outlet boundary an average static pressure, the top and bottom surfaces set as periodic, and the airfoil surface as a smooth, no-slip adiabatic wall. A fixed incidence angle (α) was set at the inlet plane with turbulence generation specified using a constant turbulence intensity (TI) and length scale (l) dependent on the test case, $\alpha = \pm 20°$, $TI\% = 5 - 20\%$, and $l = 1 - 100\%$ of the airfoil pitch. Outlet average static pressure was adjusted depending on the desired inlet-total to outlet-static pressure ratio. Reynolds number, based on the velocity taken at the evaluation plane and true chord, ranged between $Re_c \sim 1.0 \times 10^6$ and 2.0×10^6.

The inlet conditions were used to initialize the solution of the lowest pressure ratio; however, it should be noted that these simulations employed grid sequencing so, the domain initialization approach did not significantly influence the convergence rate. Each subsequent increase in pressure ratio used the converged solution of the simulation prior. As an example, the initial conditions of the pressure ratio case of 1.5 used the converged solution of the case of pressure ratio 1.25. This greatly reduced the overall time for convergence as well as increased the stability of the simulations. A detailed description of the grid sequencing process has been documented by Owen [12].

3.2.4 Numerical Methods

After evaluating the predictive capabilities of a number of eddy viscosity turbulence models, it was determined that the shear stress transport (SST) $k{-}\omega$ with γ transition model developed by Menter et al. [10] provided the most accurate prediction of the limit loading condition [12]. The SST $k - \omega$ model is one of the most commonly used turbulence models for CFD of turbomachinery [15, 16, 17]. A summary of the expressions for the transport equations of turbulent kinetic energy, k, and its specific dissipation rate, ω, as well as the eddy viscosity, μ_t, are given in [18]. For a detailed description on how the transition equation is incorporated into the SST model refer to the STAR-CCM+ documentation [19].

A coupled, implicit compressible algorithm in steady state solves the equations for mass, momentum, and energy. A second-order discretization was used for the source and diffusion terms and a second-order upwind scheme for the convection terms of momentum and turbulence equations. The inviscid, convective fluxes were calculated using Roe's flux-difference splitting scheme, adapted for use with Weiss-Smith preconditioning for all-speed flows. The algebraic multi-grid (AMG) linear solver with a V-cycle, Gauss-Siedel relaxation scheme and bi-conjugate gradient stabilizer acceleration method were employed. For additional information, refer to the manual provided by STAR-CCM+ [19]. All simulations were run until the flow had reached full convergence such that the normalized residuals of all transport quantities dropped at least four order of magnitude and were steady, and the local total pressure loss coefficient did not show fluctuations over $\pm$ 0.0001 for 1500 iterations, which typically occurred around 3500 iterations.

3.3 Results and Discussion

First a sweep of pressure ratios from 1.25 to 10 was performed for each airfoil at base conditions; 0° incidence, 10% turbulence intensity and 10% airfoil pitch for turbulent length scale. This was done to observe the path to limit loading as well as to document the effects of excessive supercritical loading. Numerical Schlieren images and blade surface pressure forces are included to fully characterize the flow domain with a review of the main flow features at limit loading presented and discussed in regard to airfoil geometry. The investigation was then extended for a range of incidence and turbulence variations; positive and negative 20° incidence, 5 to 20% turbulence intensity and 1 to 100% airfoil pitch for turbulent length scale. Quantities of mass-flow averaged flow angle, limit loading pressure ratio and mass-flow averaged total pressure loss coefficient are presented alongside pitchwise loss distributions to provide a detailed description of the effects of inflow conditions on airfoil exit conditions.

To maintain consistency with the experiment used for validation, a mass-flow averaged loss coefficient (Y_p), defined as the total pressure loss normalized by the dynamic pressure was used.

$$Y_p = \frac{P_{oi} - P_{oe}}{P_{oe} - P_{se}} \tag{3.2}$$

Here subscripts i, e denote values of the total pressure (P_o) at the inlet and outlet evaluation planes, respectively, and the subscript se represents the static pressure at the evaluation plane; total pressure quantities were mass-flow averaged and static pressure quantities were area-averaged using the formulations of Ligrani [20].

Table 3.2: Comparison of mass-averaged losses and mixed-out losses at limit loading.

Airfoil	Pressure Ratio	$Y_{p,Eval}$	$Y_{p,Outlet}$	$Y_{m,Eval}$
1	3.6	0.037	0.065	0.065
2	2.6	0.043	0.070	0.070
3	5.3	0.055	0.188	0.189
4	3.3	0.040	0.091	0.092

It should be noted that the authors regularly observe mass averaged losses at a number of planes throughout the domain as well as mixed-out quantities; however, as to not include an extensive amount of data in the publication we did not include them in this report. However, as a means of transparency we have provided a table comparing the mass averaged losses at the evaluation plane, the mixed-out losses calculated from the evaluation plane and the mass averaged losses at the domain outlet for each airfoil at limit loading 3.2. As expected, losses increase greatly as the flow mixes downstream towards the outlet.

3.3.1 Performance at Base Conditions

The results at base conditions are shown in Figure 3.5 with a summary presented in Table 3.3. Here α_2 is the mass-flow averaged outlet flow angle, M_x is the mass-flow averaged axial component of Mach number, PR_{LL} is the pressure ratio at limit loading and Y_p is the mass-flow averaged total pressure loss coefficient. The subscripts TE and $Eval$ represent the location where mass-flow averaging was preformed, the trailing edge and evaluation planes respectively.

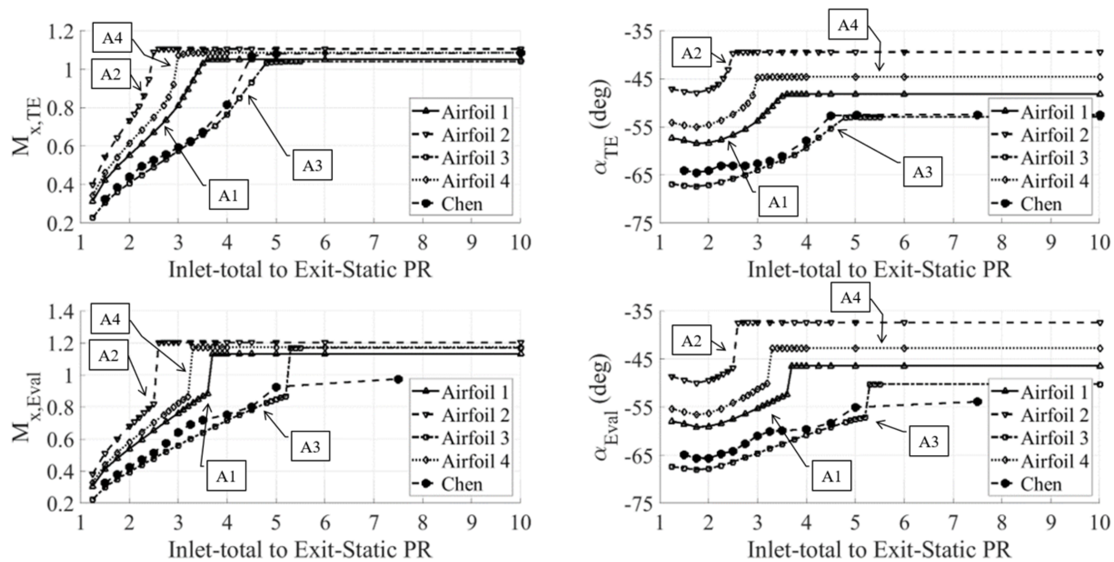

Figure 3.5: Mass-flow averaged quantities of axial Mach number and flow angle.

Similar to the work of Chen [6], as limit loading is reached both mass-flow averaged axial component of Mach number and mass-flow averaged flow angle reach an asymptotic limit when evaluated at the trailing edge. The pressure surface shock that originates from the rapid expansion around the trailing edge becomes increasingly oblique until it no longer impacts the suction surface of the adjacent airfoil. The flow upstream of the pressure surface shock becomes fully choked and any further increase in pressure ratio has no effect on the upstream solution. Contrary to previous work the results measured at the downstream evaluation plane, although at a slightly higher-pressure ratio, show a similar trend to those at the trailing edge. As supercritical loading is reached the entire passage appears to become choked and the complete flow solution remains unchanged by any further decrease in outlet pressure.

Table 3.3: Airfoil performance summary.

Airfoil	1	2	3	4
$\alpha_{2,TE}$	$-48°$	$-39°$	$-53°$	$-45°$
$M_{x,TE}$	1.05	1.11	1.04	1.09
$\alpha_{2,Eval}$	$-46°$	$-37°$	$-50°$	$-43°$
$M_{x,Eval}$	1.13	1.20	1.17	1.17
PR_{LL}	3.6	2.6	5.3	3.3
Y_p	0.037	0.043	0.055	0.040

For the case of simulating trailing edge shock waves, placement of the outlet boundary is critical to obtain non-reflected shock patterns that can intrude on the predicted solution near the planes of assessment [12]. When the outlet boundary is positioned too near the trailing edge shock structures numerical reflections can occur that potentially contaminate simulation results. The current work positioned the outlet boundary specifically to ensure numerical reflections did not influence measurements. As a result two phenomena occurred in contrast to the study conducted by Chen [6]; 1. The mass-flow averaged axial component of Mach number and the mass-flow averaged exit flow angle increase from the trailing edge to the evaluation plane and 2. The values at the evaluation plane reach an asymptotic limit, similar to the predictions at the trailing edge.

The deflection angle calculated as the difference in mass-flow averaged exit flow angle and airfoil outlet metal angle was similar for each case and found to be consistent with the experimental results of Hauser [3], within 10 and 13 degrees. As previously mentioned, Hauser found none of the six analytical methods presented in their work to be adequate at predicting deflection angles [3], supporting the use of CFD to aid in the understanding of airfoil limit loading. Additional flow turning, calculated as the difference of mass-flow averaged flow angle at the trailing edge and evaluation planes was near identical for the airfoils considered. Roughly 2.5 degrees of additional turning is experienced downstream of the trailing edge.

Focusing on the mass-flow averaged predictions at the trailing edge it is clear that the path to limit loading is different for each airfoil. Airfoil 2 experienced limit loading much earlier than the other profiles considered, reaching limit loading at a pressure ratio of 2.6; airfoil 3 in contrast reached limit loading much more gradually at a pressure ratio of 5.3. This is consistent with the results of Hauser [4], who showed that the point of limit loading is strongly dependent on the airfoil outlet metal angle. As the outlet metal angle is more aggressive the range of pressure ratios prior to limit loading is improved. However, an exception is seen for airfoils 1 and 4 which have the same outlet metal angle but different limit loading pressure ratios, implying that the outlet metal angle is not the only geometric factor influencing limit loading onset. It is believed that the airfoil unguided turn angle and trailing edge blockage ratio play a significant role. However, an additional investigation isolating the specific differences between the airfoil geometries is required to provide a complete explanation.

Similar to the onset of limit loading, the range of sub-limit pressure ratios is dependent on the airfoil geometry. The smallest range of pressure ratios is observed for airfoils 2 and 4, with only a rise of 0.5 and 1.0 ΔPR respectively from critical to limit loading. Airfoils 1 and 3 exhibited the largest predicted ranges with 1.6 and 2.8 ΔPR, showing a much larger series of efficient working pressure ratios than the other profiles. This increase is believed to be caused by a combination of outlet metal angle and trailing edge blockage ratio. As previously mentioned, the results of Hauser showed the onset of limit loading as strongly correlated with the outlet metal angle; a more aggressive outlet metal angle leads to a higher limit loading pressure ratio. Similarly, trailing edge blockage ratio appears to play a role in the determination of the critical loading pressure ratio. As the trailing edge blockage ratio is increased the pressure ratio required to reach critical loading is decreased. The combination of contrasting effects causes the sub-limit loading range to shrink for airfoils 2 and 4.

Airfoil 2 shows the smallest range due to the largest trailing edge blockage and least aggressive outlet metal angle.

As a method to qualitatively inspect the flow characteristics at the various stages from critical to supercritical loading; numerical schlieren images, shown in Figure 3.6, are presented for each of the four airfoils. These images were produced as an inverse normalized density gradient and are computed using Equation 3.3. Here c_1 and c_2 are constants equal to 0.8 and 1000 respectively; $\nabla\rho$ is the density gradient and the subscripts *max* and *min* are the maximum and minimum values of the density gradient throughout the flow domain.

$$f(y) = c_1 e^{\left(-c_2 \frac{|\nabla\rho| - |\nabla\rho|_{min}}{|\nabla\rho|_{max} - |\nabla\rho|_{min}}\right)} \tag{3.3}$$

As a reminder, critical loading is the pressure ratio at which the flow within the throat of the blade passage reaches unity, sub-limit loading is between critical and limit loading, limit loading is the pressure ratio at which the blade loading does not change and supercritical loading is any pressure ratio beyond. From top to bottom the airfoils are shown in increasing numerical order. The left most image shows the pressure ratio of critical loading, followed by a point of sub-limit loading, then the pressure ratio at limit loading and lastly a point of supercritical loading. Specific pressure ratios are listed for critical and limit loading allowing for inference of the ranges of sub-limit and supercritical loadings.

Overall, the shock patterns of each airfoil are quite similar for each stage of loading. The point of critical loading shows a trailing edge pressure surface shock (TEPSS) impacting the suction surface of the adjacent airfoil, reflecting off, then dissipating before the trailing edge suction surface shock (TESSS) of the next airfoil. Sub-limit loading causes the TEPSS to turn downstream while increasing in magnitude; the reflected shock is able to maintain strength to propagate downstream ultimately coalescing with the TESSS of the adjacent airfoil. As limit loading is reached the TEPSS

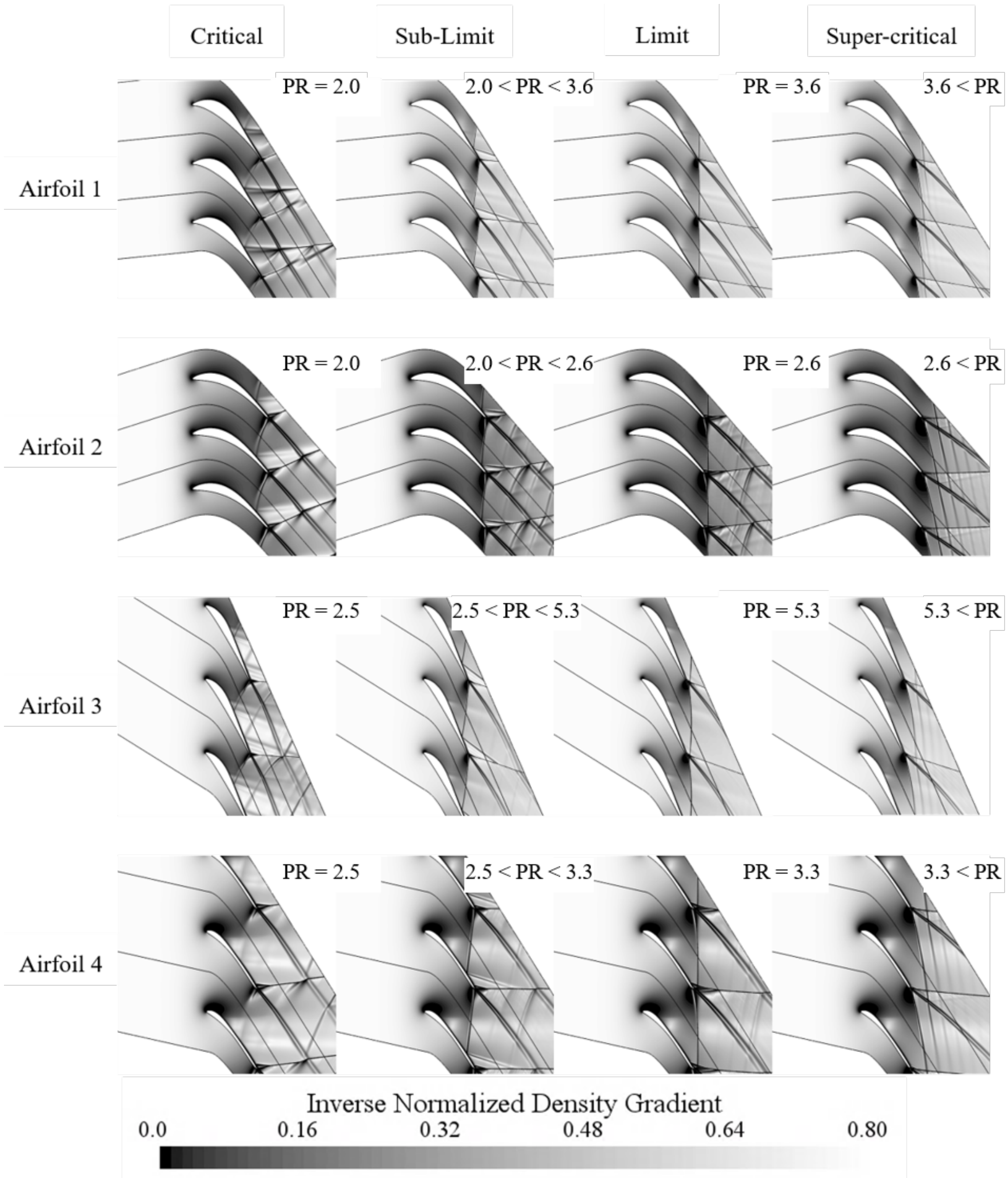

Figure 3.6: Numerical Schlieren images for each airfoil at different load cases.

has achieved sufficient turning to miss the trailing edge of the adjacent airfoil becoming nearly parallel to the tangential flow direction and choking the flow within the blade passage; and supercritical loading shows the TEPSS reaching maximum turning, completely missing the adjacent airfoil and propagating un-reflected downstream completely choking the full flow domain.

Throughout the stages of limit loading slight differences are observed within the blade passage as well as the strength and direction of the two trailing edge shock structures. During critical loading airfoils 1 and 3 both display smooth flow profiles within the blade passage, showing relatively small regions of compression near the leading-edge and no flow separation until the point of shock impingement. Contrastingly, airfoils 2 and 4 show large stagnation regions near the leading edge with airfoil 4 showing a slight period of flow separation along the suction surface. As these were run with zero incidence, variance here is caused by the difference in airfoil design incidence and inlet metal angle. Looking downstream there is a noticeable change in the location of trailing edge shock impingement between profiles. Airfoil 3 shows the point of impingement nearly halfway through the blade passage, whereas airfoil 2 shows the location much further downstream at roughly 0.7 C_x. The airfoil stagger angle is directly responsible for this change. As airfoil stagger is increased the point of shock impingement moves further aft of the adjacent airfoil. This trend is continued until limit loading and will be discussed in more detail later.

Although the flow within the blade passage upstream of the TEPSS remains unchanged as pressure ratio is increased, the strength of the shock structures downstream grows significantly for all profiles considered. Increased periods of flow expansion, observed near the trailing edge pressure surface, manifest into larger strength TEPSS that are able to reflect and propagate downstream. The total amount of strength increase is dependent on the range of sub-limit pressure ratios experienced by each profile. Airfoils 1 and 3 exhibit larger periods of sub-limit loading allowing for increased variance in density gradient magnitude compared to airfoils 2 and 4, shown by lighter color within the blade passage. As previously mentioned, the difference in range of sub-limit pressure ratios is due to contrasting effects of outlet metal angle and trailing edge blockage ratio. More pronounced outlet metal angle allows for higher limit loading pressure ratios while increased trailing edge blockage results in lower critical pressure ratios. With the exception in the total magnitude of density gradient limit and super-critical loading flow characteristics are similar between profiles, the TEPSS turns past the suction surface of the adjacent airfoil and propagates un-reflected downstream.

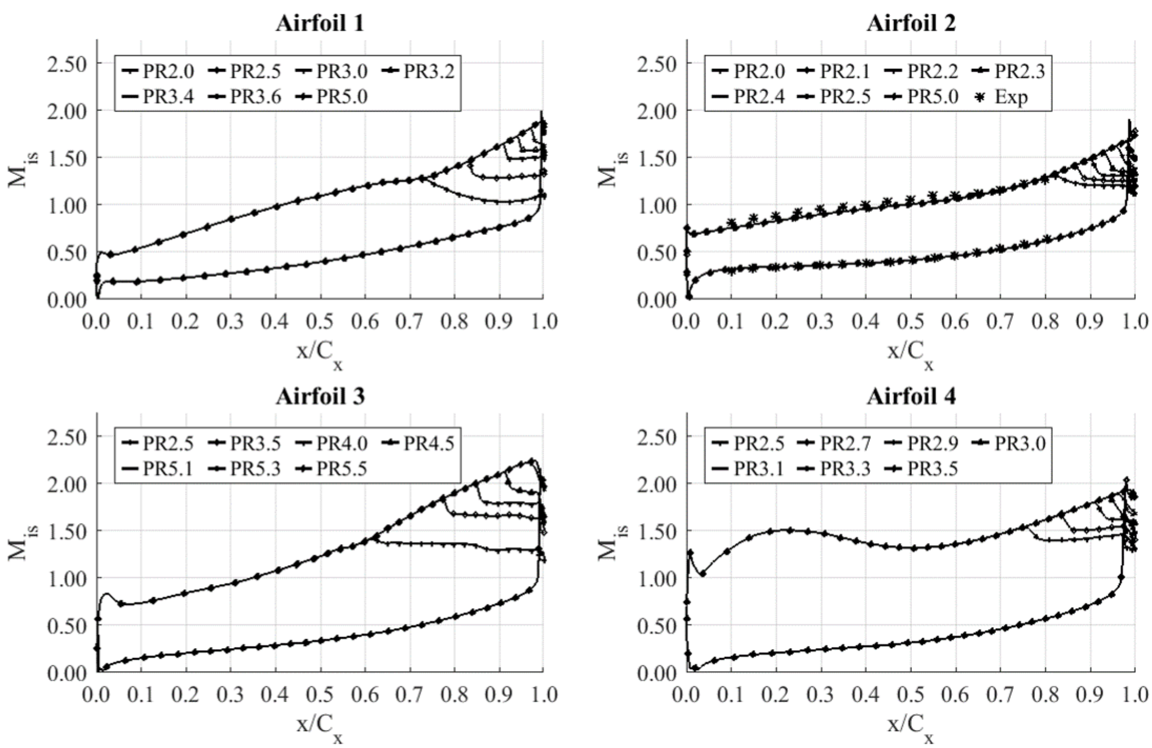

Figure 3.7: Surface isentropic Mach number distributions for each airfoil.

The computed distributions of surface isentropic Mach number are presented in Figure 3.7 as a function of axial distance (x/C_x). For each profile the number of surface distributions is limited to seven and only every 25th point is displayed. The lowest pressure ratio presented is the point of critical loading and the highest is the point of limit loading. As expected, no change in surface isentropic Mach number was seen past limit loading. Also included for airfoil 2 is the available validation data as used in [12]. It should be noted that the validation preformed previously was done at the design incidence rather than the baseline incidence of this study, the inlet metal angle. Although at slightly different flow angles, surface pressure distributions are in very good agreement providing a brief look at the validation process.

With the exception of the leading and trailing edge, surface isentropic Mach number distributions are similar for the pressure surface of all airfoils and pressure ratios considered. At critical loading the flow along the pressure surface is fully choked, therefore no change in loading is seen with increasing pressure ratio. The flow remains subsonic with a gradual rise in surface isentropic Mach number towards the trailing edge, implying a favorable pressure gradient for the majority of the pressure surface.

Not including airfoil 4, which will be discussed separately, distributions along the first half of the suction surface are similar between profiles. A strong favorable pressure gradient is predicted as the flow is accelerated around the leading edge, then as the curvature meets the suction surface a slight dip implies a slight pressure increase. Past the leading-edge a gradual rise in surface isentropic Mach number is predicted, implying a favorable pressure gradient towards the center of the airfoil. Airfoil 4 shows an abrupt rise and fall in surface isentropic Mach number towards the center of the profile. This is due to a difference between the design incidence and the inlet metal angle or zero incidence. As the design incidence was much shallower than the inlet metal angle, a rapid acceleration around the leading-edge causes flow separation. A large increase in the surface isentropic Mach number, caused by a large favorable pressure gradient is experienced as the flow separates, then as the flow reattaches there is a pressure recovery towards the center of the profile.

For critical and sub-limit pressure ratios loading distributions along the aft portion of each profile were highly dependent on the location of initial choking and the point of shock impingement. During critical loading the throat of the blade passage is shown as a point of inflection in the suction surface isentropic Mach number. Predictions for airfoil 3 show this to be roughly 0.6 C_x aft of the leading edge while airfoils 1, 2 and 4 show this location to be roughly 0.7 to 0.8 C_x. As previously mentioned, the location of shock impingement is strongly correlated with the airfoil stagger angle. As stagger angle is increased the location of choking is moved forward along the profile, with a limit of approximately 0.6 C_x for airfoil 3.

Further increase of the pressure ratio through sub-limit loading causes the point of isentropic Mach number inflection to move downstream. The TEPSS becomes increasingly oblique and pronounced, resulting in a strong adverse pressure gradient near the shock front causing a rapid reduction in surface isentropic Mach number of the adjacent airfoil at shock impingement. Similar to the onset of choking during critical loading, increased airfoil stagger angle moves the location of the shock impingement further upstream of the airfoil profile. Past this inflection point surface pressure shows an abrupt recovery followed by a period of consistency towards the trailing edge. Once limit loading is reached the shock no longer impacts the suction surface of the adjacent airfoil and the blade loading reaches a maximum. Any further increase in pressure ratio does not change the airfoil loading distribution.

3.3.2 Effect of Inflow Conditions

Next the effects of incidence, turbulence intensity and turbulent length scale on the flow characteristics of each airfoil are summarized and discussed, Figures 3.8 to 3.13. Figures 3.8, 3.10 and 3.11 show plots of mass-flow averaged flow turning, limit loading pressure ratio and mass-flow averaged total pressure loss coefficient at limit loading for each set of inflow variation. Figures 3.9, 3.12, and 3.13 show pitchwise total pressure loss distributions taken at the evaluation plane as a means to provide additional insight into specific loss generation mechanisms.

3.3.3 Incidence Variation

Shown top of Figure 3.8 is the amount of predicted flow turning during negative, zero and positive incidence. Change in flow turning is directly proportional to the change in incidence, suggesting that the difference here is not a product of incidence variation but rather airfoil geometry. Subtracting incidence from flow turning, it is clear that there is no change in the mass-flow averaged outlet flow angle with incidence. Similarly, the pressure ratio required to reach limit loading is unaffected, remaining nearly constant across flow cases. This agrees with the findings of Hauser [3], that the dominant factor in the prediction of outlet flow direction and the limit loading pressure ratio remains purely geometrical, specifically the airfoil outlet metal angle.

Table 3.4: Incidence effect - loss summary.

Airfoil	$-20°$	$+20°$
1	-1.9%	+9.1%
2	-3.9%	+25.4%
3	+2.9%	+4.0%
4	-0.2%	+6.2%

Of the flow parameters presented, the most notable difference between cases is in the prediction of mass-flow averaged total pressure loss coefficient. Results as a percent difference from the baseline case are summarized in Table 3.4.

As can be seen, negative incidence variation results in a slight reduction in loss for airfoils 1 and 2, relatively no change for airfoil 4 and a slight increase for airfoil 3 whereas positive incidence variation increases losses significantly for each profile. It should be noted that the design incidence of these profiles is different than the incidence angles tested; therefore, the change in losses for these cases should not be specifically attributed to a phenomena of limit loading but rather a combination of limit loading effects and leading edge suction surface boundary layer size, caused by a change in the leading edge pressure gradient.

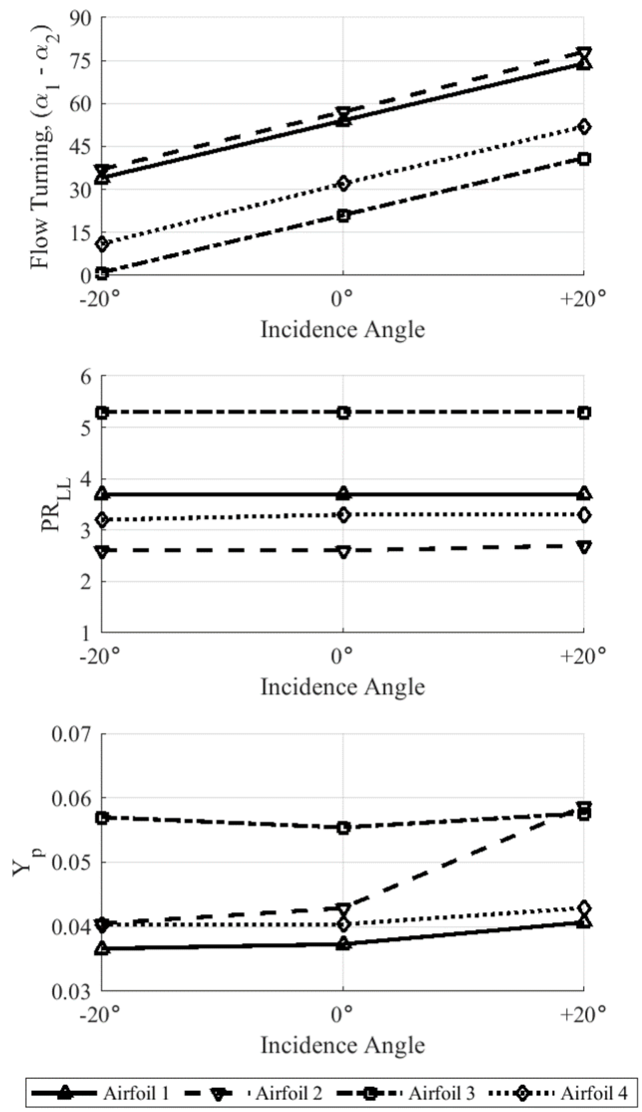

Figure 3.8: Incidence effect on limit loading.

Figure 3.9 shows the pitchwise distribution of losses downstream of the cascade collected at the evaluation plane 1.5 axial chord lengths downstream of the leading edge. The plots are centered at the top periodic interface, with positive values of y/s moving towards the adjacent airfoil above and negative values moving through the wake below. Three loss categories are defined from these plots; 1. the "freestream" losses or the high-pressure mid-passage region upstream of the trailing edge suction surface shock (TESSS), 2. the "shock" losses or the low-pressure mid-passage region on the downstream side of the TESSS and 3. the "wake" region shown as the loss peak.

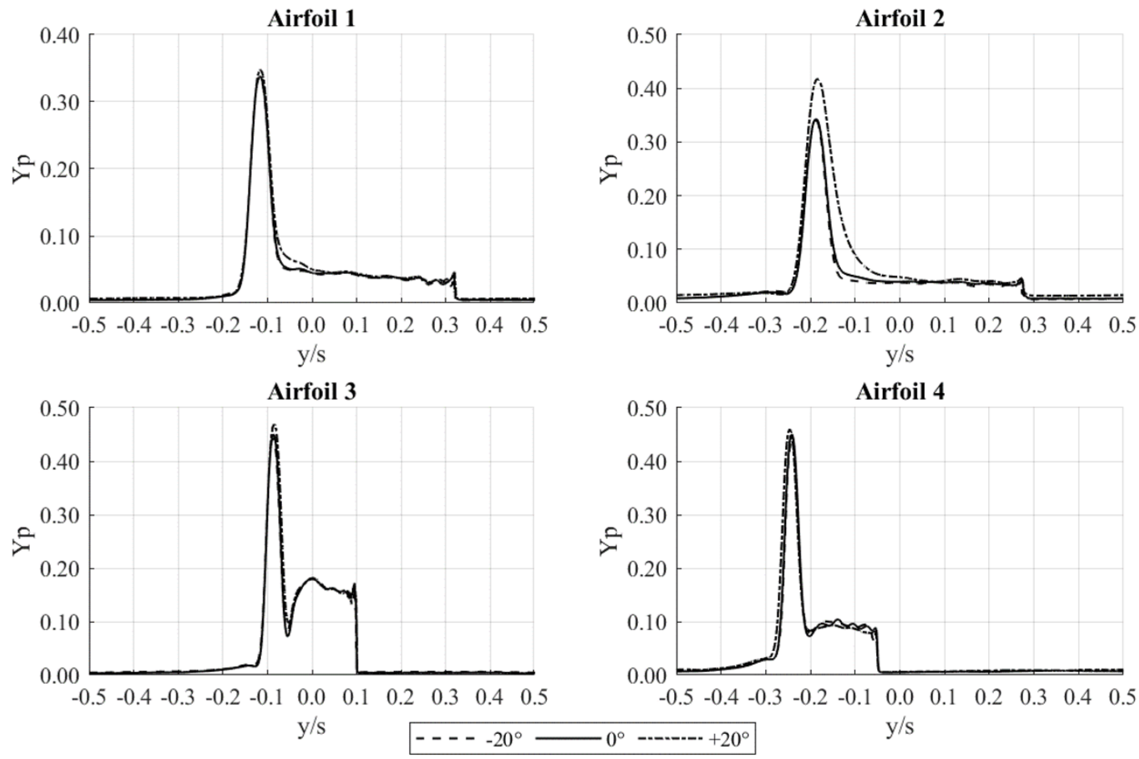

Figure 3.9: Incidence effect on local total pressure loss.

For each of the airfoils considered, the freestream losses are minimal compared to the wake and shock losses. During limit loading the shock losses increase significantly and can account for nearly 50% of the losses within the passage [17].

Isolating the differences between pitchwise loss profiles it is clear that for positive incidence the predicted total pressure loss increases due to growth in the wake width and depth. The aggressive inlet flow angle causes a large stagnation region along the pressure side, leading to a favorable pressure gradient along the leading-edge suction surface. This causes rapid flow expansion around the leading-edge allowing for sufficient momentum to grow the suction surface boundary layer leading to potential flow separation, as is the case for airfoil 2. Airfoils 1, 3 and 4 experience similar flow characteristics; however, the flow remains attached to the airfoil surface. Nevertheless, the increase in momentum around the leading-edge causes a large growth in the suction side boundary layer leading to increased profile losses. The combination of increased suction surface boundary layer thickness and decreased freestream total pressure causes the wake to grow in width and depth.

3.3.4 Turbulence Variation

Next, the results for variation of inlet turbulence intensity and turbulent length scale are shown in Figures 3.10 and 3.11. Similar to the impact of incidence, the effect of inflow turbulence on flow turning and limit loading pressure ratio is overall insignificant. The predicted mass-flow averaged total pressure loss coefficient grew drastically for both changes of turbulence intensity and length scale and is discussed in the following section.

Summarized in Table 3.5 are the changes in loss coefficient as a percent difference of baseline losses. Results show a direct correlation between inflow turbulence level and local mass-flow averaged total pressure loss coefficient. Similar to the experimental results of Folk [21], increases in turbulence intensity caused an increase in roughly 20 to 40% of the mass-flow averaged total pressure loss coefficient. Interestingly, changes in turbulence intensity from 5 to 10% and turbulent length scale from 1 to 10% airfoil pitch show near identical significance. This suggests that the impact of mid-level turbulence variation is balanced between both turbulent length and velocity scales. As turbulence level is further increased it is clear that the impact of turbulence intensity becomes much more significant.

Table 3.5: Intensity and length scale effect - loss summary.

Airfoil	$TI = 5\%$	$TI = 20\%$	$l = 1\%$	$l = 100\%$
1	-9%	+23%	-9%	+7%
2	-8%	+15%	-8%	+3%
3	-6%	+16%	-6%	+3 %
4	-12%	+31%	-12%	+6%

Figures 3.12 and 3.13 show the pitchwise distribution of total pressure loss coefficient downstream of the cascade. For the case of increased turbulence intensity, there is a significant change in the predicted suction side wake profile as well as the high-

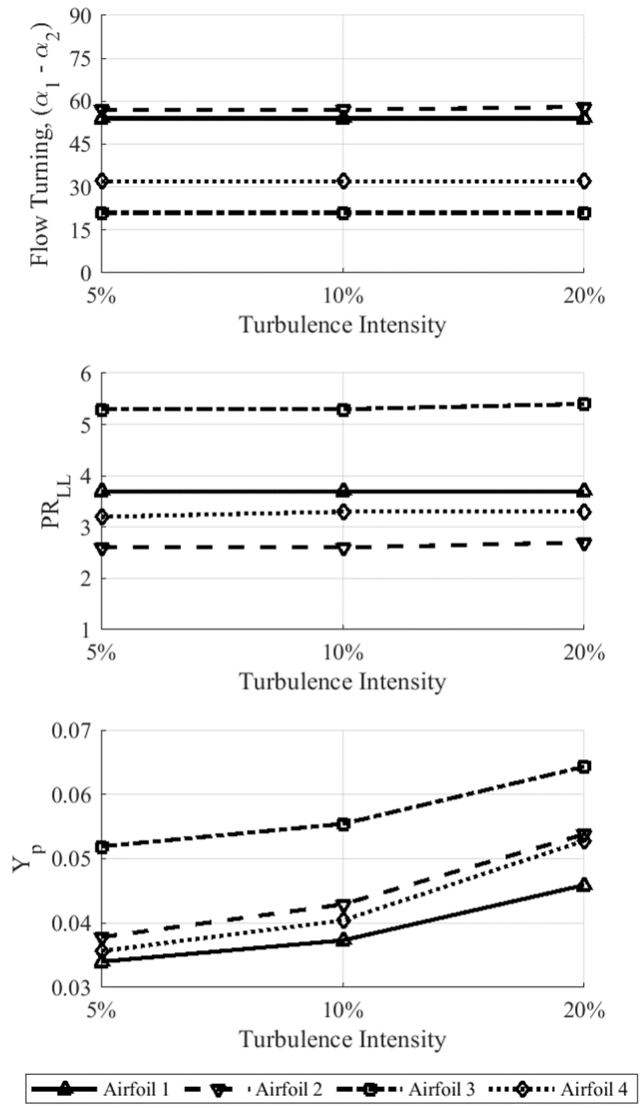

Figure 3.10: Intensity effect on limit loading.

pressure "shock" section of the mid-passage region for each airfoil, the pressure side remains relatively unchanged. As discussed by Folk [21] this is a product of a change in shape factor for the suction surface boundary layer near the trailing edge. As inlet turbulence intensity is increased, the amount of turbulent penetration into the suction surface boundary layer is increased. This causes the production of turbulent kinetic energy to rise as the turbulence is stretched from the high shear stress within the boundary layer. Freestream losses are also predicted to increase with increased turbulence intensity; however, with a much lower significance.

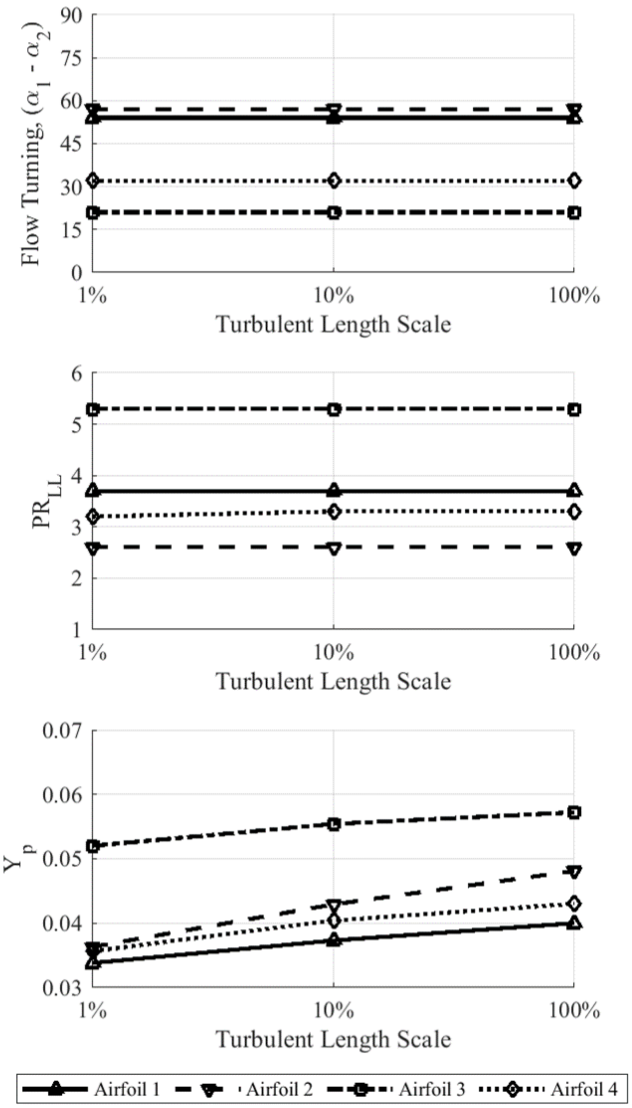

Figure 3.11: Length scale effect on limit loading.

Similarly, variation of turbulent length scale resulted in a change in the predicted suction side wake profile, little change is seen in the mid-passage shock losses. As inlet turbulent length scale is reduced, turbulent penetration into the boundary layer diminishes while also occurring further downstream of the blade surface. The decrease in turbulence kinetic energy production along the suction surface results in a decrease in boundary layer thickness reducing the total profile loss and subsequent wake profile.

Last a review of the impact on blade loading is shown for airfoil 1 as an example of the influence for each of the profiles considered, Figure 3.14. As can be seen there is

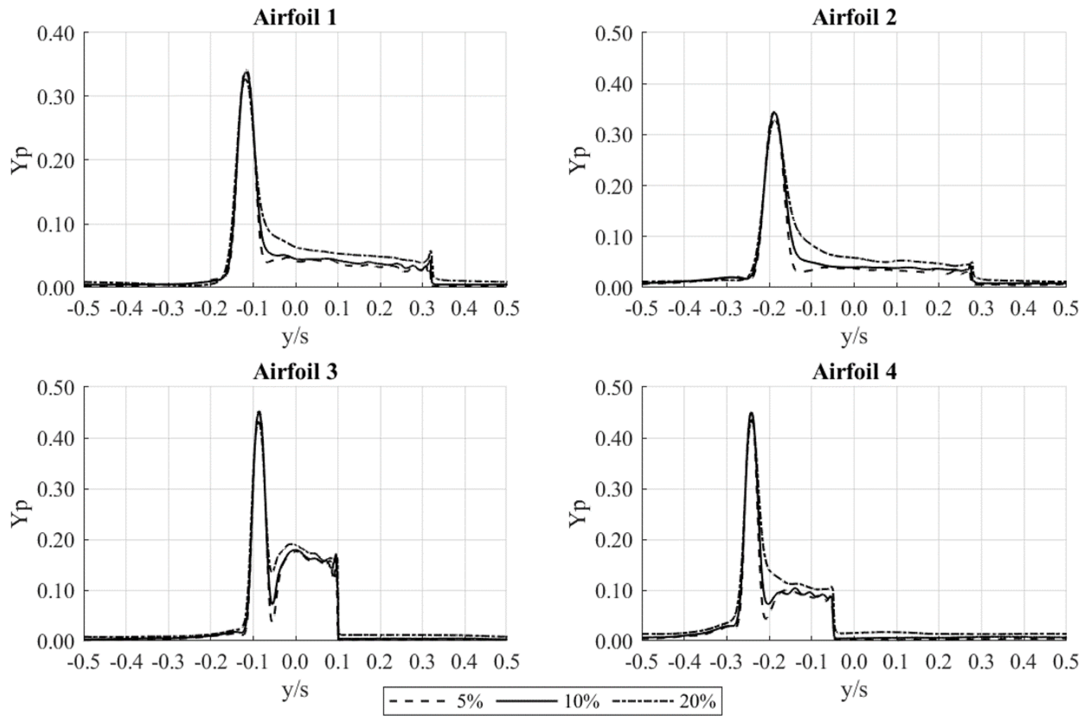

Figure 3.12: Turbulence intensity effect on local total pressure loss.

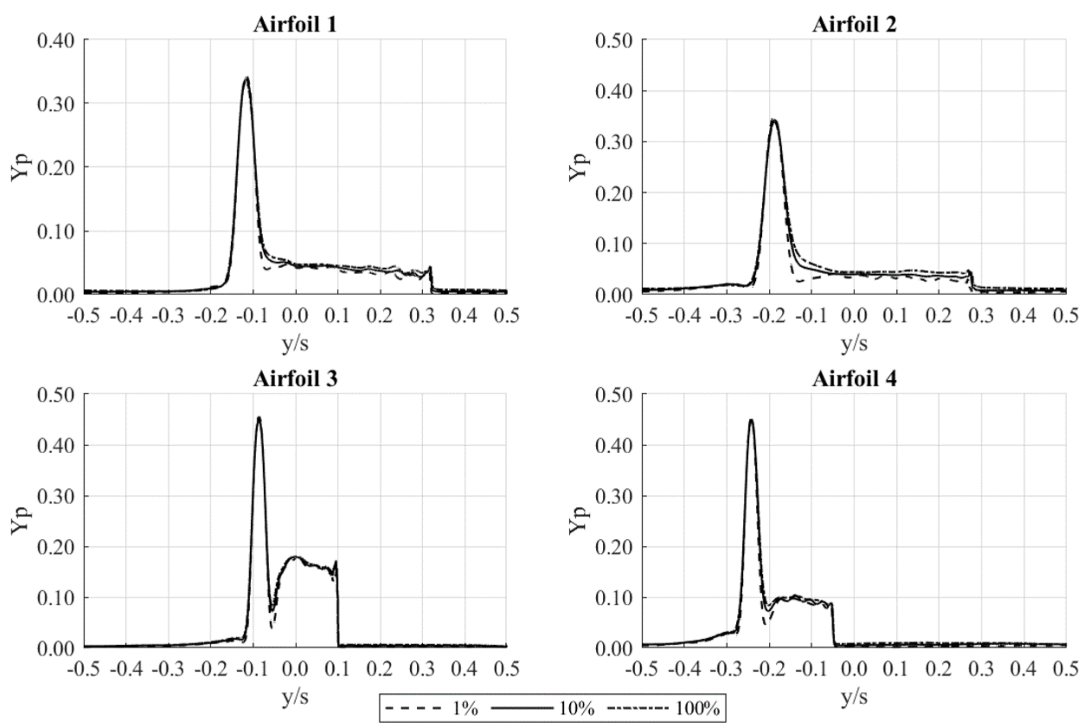

Figure 3.13: Turbulent length scale effect on local total pressure loss.

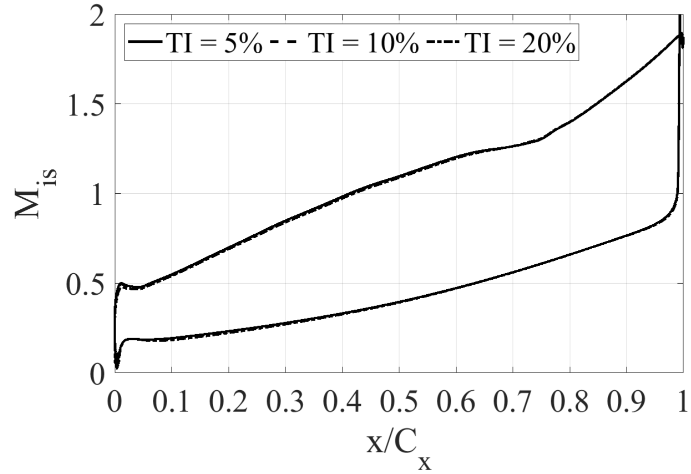

Figure 3.14: Turbulence level impact on blade loading.

little to no change in the surface isentropic Mach number distribution for the majority of the blade surface. This implies that the impact of inflow turbulence level on the net work output of the profiles considered is negligible. It should be noted that all of the profiles displayed this trend, and are therefore not presented.

3.4 Conclusion

To better understand the onset of airfoil limit loading and its relation to inflow conditions a computational fluid dynamic investigation was performed for four different turbine airfoils under sub-critical, critical and super-critical conditions.

Similar to previous work [2, 6], as limit loading is reached the flow within the airfoil passage becomes fully choked and any further increase in pressure ratio fails to change the channel output. Contrary to the work of Chen [6], the results taken at the evaluation plane, although delayed, show a similar trend to those at the trailing edge. This difference is believed to be a result of numerical contamination caused by reflected shock waves from the domain outlet boundary. Consistent with the results of Hauser [3], the outlet metal angle was found to be the dominant geometric parameter to influence the limit loading pressure ratio as well as the mass-flow averaged outlet flow angle. An exception was seen for airfoils 1 and 4 which have the same outlet metal angle but different limit loading pressure ratios. It is believed that airfoil unguided turning, trailing edge blockage ratio and airfoil stagger angle play a significant role; however, an additional investigation isolating the specific differences between airfoil geometries is required to provide a complete explanation. Analogous to previous experimental results [3]; flow deflections were predicted to be within 10 and 13 degrees, with additional flow turning downstream of the trailing edge being roughly 2.5 degrees for all profiles considered.

The influence of inflow conditions on the mass-flow averaged outlet flow angle and the limit loading pressure ratio were found to be insignificant. Predictions of the mass-flow averaged local total pressure loss coefficient were found to be highly sensitive to inflow variation, specifically during positive incidence variation and higher turbulence levels.

For positive incidence variation a large stagnation region on the airfoil pressure side lead to a strong favorable pressure gradient along the leading-edge suction surface. The increase in momentum, caused by flow expansion around the leading-edge, resulted in significant growth of the suction side boundary layer leading to increased profile losses.

Similar to previous experimental work, the effect of combustor turbulence on turbine losses was significant and lead to a drastic rise in local total pressure loss coefficient (20-40%). This was found to be a product of increased turbulent penetration into the suction surface boundary layer, resulting in a change in downstream wake profile. An increase in turbulent kinetic energy production along the suction surface resulted in an increase in suction surface boundary layer thickness drastically increasing total pressure losses.

REFERENCES

[1] A. J. Glassman, "Estimating turbine limit load," *NASA CR-191105*, 1993.

[2] I. Fruchtman, "The limit load of transonic turbine blading," in *Turbo Expo: Power for Land, Sea, and Air*, vol. 79788, p. V01AT01A080, American Society of Mechanical Engineers, 1974.

[3] C. H. Hauser, H. W. Plohr, and G. Sonder, "Study of flow conditions and deflection angle at exit of two-dimensional cascade of turbine rotor blades at critical and supercritical pressure ratios," *NACA-RM E9K25*, 1950.

[4] C. H. Hauser and H. W. Plohr, "Two-dimensional cascade investigation of the maximum exit tangential velocity component and other flow conditions at the exit of several turbine blade designs at supercritical pressure ratios," *NACA-RM E51F12*, 1951.

[5] S. S. Chen, "Axial-flow turbine rotor discharge-flow overexpansion and limit-loading condition. part 2; method of analysis and performance evaluation of computer code axod2," *NASA/TM-2018-219911*, 2018.

[6] S. S. Chen, "Axial-flow turbine rotor discharge-flow overexpansion and limit-loading condition, part 1: Computational fluid dynamics (cfd) investigation," *NASA/TM-2017-219506*, 2017.

[7] D. Mimic, P. Sauer, M. Oettinger, and F. Herbst, "Shock-vortex interaction in a transonic turbine cascade," *Proceedings of Global Power and Propulsion Society Beijing Conference. GPPS-BJ-2019-0008*, 2019.

[8] P. A. Lee and J. D. Anderson, *Modern Compressible Flow, with Historical Perspective*. McGraw-Hill Science, Engineering & Mathematics, 1982.

[9] M. Folk, *The Impact of Combustor Turbulence on Loss Mechanisms in the High Pressure Turbine*. PhD thesis, University of Cambridge, 2020.

[10] F. R. Menter, P. E. Smirnov, T. Liu, and R. Avancha, "A one-equation local correlation-based transition model," *Flow, Turbulence and Combustion*, vol. 95, no. 4, pp. 583–619, 2015.

[11] C. Sooriyakumaran, "Experimental study of profile losses in three transonic turbine cascades," masters thesis, Carelton University, 2014.

[12] S. Owen, F. Taremi, and M. Uddin, "Turbulence modeling effects of transonic, high pressure airfoils near design incidence," in *AIAA Aviation 2019 Forum*, p. 2965, 2019.

[13] F. Taremi, *Endwall flows in transonic turbine cascades.* PhD thesis, Carleton University, 2013.

[14] D. Corriveau and S. Sjolander, "Influence of loading distribution on the performance of transonic high pressure turbine blades," *Journal of Turbomachinery(Transactions of the ASME)*, vol. 126, no. 2, pp. 288–296, 2004.

[15] Z. Wang, Z. Liu, and Z. Feng, "Influence of mainstream turbulence intensity on heat transfer characteristics of a high pressure turbine stage with inlet hot streak," *Journal of Turbomachinery*, vol. 138, no. 4, p. 041005, 2016.

[16] G. A. Ledezma, G. M. Laskowski, and A. K. Tolpadi, "Turbulence model assessment for conjugate heat transfer in a high pressure turbine vane model," in *ASME Turbo Expo 2008: Power for Land, Sea, and Air*, pp. 489–499, American Society of Mechanical Engineers, 2008.

[17] P. Duan, C. S. Tan, A. Scribner, and A. Malandra, "Loss generation in transonic turbine blading," *Journal of Turbomachinery*, vol. 140, no. 4, p. 041006, 2018.

[18] F. R. Menter, R. B. Langtry, S. Likki, Y. Suzen, P. Huang, and S. Völker, "A correlation-based transition model using local variables - part 1: model formulation," *Journal of Turbomachinery*, vol. 128, no. 3, pp. 413–422, 2006.

[19] Siemens, "Star-ccm+ user manual," 2021. Last accessed 10 Oct. 2021.

[20] P. Ligrani, "Aerodynamic losses in turbines with and without film cooling, as influenced by mainstream turbulence, surface roughness, airfoil shape, and mach number," *International Journal of Rotating Machinery*, vol. 2012, 2012.

[21] M. Folk, R. J. Miller, and J. D. Coull, "The impact of combustor turbulence on turbine loss mechanisms," in *Turbo Expo: Power for Land, Sea, and Air*, vol. 58561, p. V02BT40A002, American Society of Mechanical Engineers, 2019.

CHAPTER 4: (PAPER 3) A CHARACTERIZATION OF UNSTEADY EFFECTS ON AIRFOIL LIMIT LOADING

4.1 Introduction

To stay competitive within the gas turbine community, turbine aero designers strive to maximize the total work output of each turbine stage through a combination of pressure ratio increase and airfoil design improvements. Although the higher power target could be achieved by increasing mass flow rate, the corresponding increase in turbine annulus area would result in structural limitations due to longer blades which cause increased strain on the blade root as well as amplified flutter and rotor dynamic excitation. An alternative path to achieving higher power output is to maximize the loading of each turbine stage through increased pressure ratio, but this may also lead to airfoil limit loading and high aerodynamic losses.

The limit loading condition was first documented by Hauser and Plohr in a National Advisory Committee for Aeronautics (NACA) Research Memorandum in the 1950s [1, 2]. They identified the blade outlet metal angle as the dominant geometric parameter to influence limit loading behavior. Following their review, numerous studies set out to provide a numerical method to predict the onset of airfoil limit loading [3, 4, 5]. These investigations proved to predict the required limit loading pressure ratio reasonably well, but they failed to provide detailed flow characteristics [5].

Recently computational fluid dynamics (CFD) has been used to provide a more in-depth analysis of the flow dynamics within a gas turbine blade passage giving designers a better understanding of the limit loading condition. Chen preformed the first detailed CFD investigation for a range of pressure ratios from sub-critical to super-critical loading [5]. Quantitative data of mean-flow Mach number, flow angle, blade forces, mass flux and total pressure loss coefficient were determined and presented alongside contours of total pressure and flow streamlines. It was shown, contrary to prior studies, that CFD provided a sufficient tool for predicting the onset of airfoil limit loading. Chen also provided a formal definition of the limit-loading condition based on channel flow theory. Expanding on this work, Owen investigated the effects of off-design inflow conditions for four different transonic turbine airfoils over a similar range of pressure ratios by varying inflow boundary conditions: incidence from $\pm 20°$, turbulence intensity from 5-20% and turbulent length scale from 1-100% of the airfoil pitch [6]. Similar to previous experimental work, it was shown that the limit loading pressure ratio and the mass-flow averaged outlet flow angle were strongly correlated with the airfoil outlet metal angle. The influence of inflow conditions on the exit flow profile was found to be minimal with the exception of the mass-flow averaged total pressure loss coefficient. Results showed that variation of incidence affected the total pressure loss coefficient of each airfoil differently, whereas increasing turbulence level resulted in higher loss coefficients for all airfoils.

These studies also showed that CFD has the ability to accurately predict the onset of limit loading as well as to provide increased understanding into the steady-state flow picture. However, there has yet to be an investigation documenting the effects of transient phenomena on the limit loading state. This paper provides a review of common unsteady simulation approaches, allowing for an assessment of the influence of transient phenomena on airfoil performance as well as an analysis of the capabilities and limitations of each modeling approach.

Shown in Figure 4.1 is a visual description of the terminology used to describe the stages of airfoil loading from critical to supercritical conditions. The set of images along the top show a simplified representation of the trailing edge shock structure for a transonic turbine airfoil, while the bottom provides a realistic contrast of numerical Schlieren RANS CFD predictions for the airfoil studied in this paper.

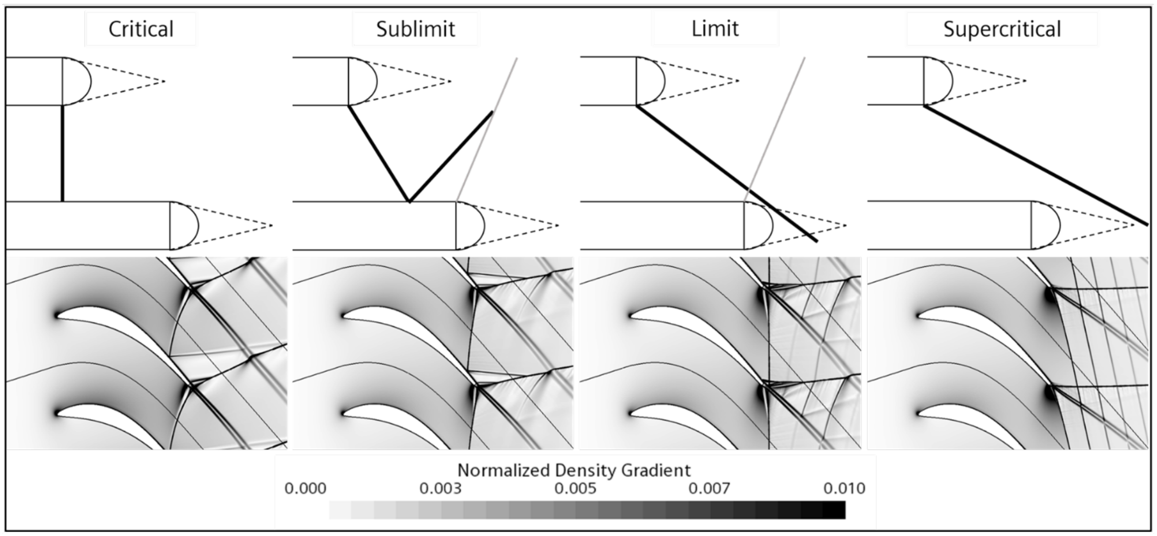

Figure 4.1: Limit loading: terminology.

The left most image, characterized by a strong Trailing Edge Pressure Side Shock (TEPSS) normal to the airfoil surface, describes the critical loading condition. At this point the pressure ratio across the airfoil results in choking of the flow upstream of the throat. As the pressure ratio is increased the TEPSS becomes oblique due to the Prandtl-Meyer expansion near the trailing edge. The TEPSS impinges on the adjacent airfoil suction surface and reflects downstream, ultimately coalescing with the weaker Trailing Edge Suction Side Shock (TESSS) and further propagating downstream towards the wake. It should be noted that for any turbine airfoil there is a range of pressure ratios from critical to limit loading, here defined as the sublimit loading range. The size of this pressure ratio range has been discussed by Owen and shown to be dependent on the airfoil geometry, specifically the airfoil stagger angle and trailing edge blockage ratio [6]. Further increase of the pressure ratio causes the TEPSS to obtain sufficient flow turning to completely miss the surface of the adjacent airfoil, moving into the base pressure region downstream of the trailing edge. This is the point of maximum loading and is defined as the limit loading condition. Super critical loading is the fourth and final loading condition, shown as the right most set of images in 4.1. Here a strong oblique TEPSS is produced that propagates downstream of the base pressure region of the adjacent airfoil and into the flow passage, causing the entire domain to become choked.

The objectives of this work are to (1) identify the effects of vortex shedding on the nature of the trailing edge shock system during airfoil limit loading, specifically on the impact to the base pressure distribution, upstream boundary layer state and downstream total pressure loss, and (2) document an assessment of the ability of each modeling approach to aid in the decisions of turbine aero designers. All simulations were preformed using a commercial finite volume code, Star-CCM+. Quantitative data of mass-flow averaged total pressure loss coefficient, mass-flow averaged flow angles, surface isentropic Mach number distributions, surface base pressure distributions, trailing edge boundary layer velocity distributions and vortex shedding frequencies are presented alongside flow visualizations of numerical Schlieren images to provide insight into the influence of transience on airfoil limit loading.

4.2 Numerical Methods

4.2.1 Airfoil and Domain Description

Two transonic turbine airfoils, shown in Figure 4.2 were used in this study: the first from the thesis of Sooriyakumaran at Carleton University in Ottawa, Canada [7], and the second from the work of Sieverding at the European Research Project BRITE/EURAM CT96-0143 on "Turbulence Modeling of Unsteady Flows in Axial Turbines" [8]. The profile adapted from Sooriyakumaran is the main focus of this paper; however, the airfoil profile from Sieverding was also analyzed to ensure adequate validation of the transient nature of the flow dynamics around the trailing edge. Table 4.1 shows the relevant geometric parameters for each profile. As shown, the airfoil from Sieverding's study has a much larger trailing edge thickness as well as higher unguided turning and stagger angle than the profile from Sooriyakumaran; however, the pitch-to-chord ratios for both profiles are similar. The airfoil testing aspect ratio for the results for the wind tunnel testing performed by Sooriyakumaran were over

Table 4.1: Airfoil geometric characteristics.

Airfoil	Sooriyakumaran	Sieverding
Aspect Ratio, h/C_t	1.5	0.7
Pitch-to-Chord Ratio, s/C_t	0.66	0.70
Blockage Ratio, t/o	0.05	0.22
Stagger Angle, ζ	27°	50°
Inlet Metal Angle, β_1	18°	0°
Unguided Turning, θ_{UG}	9°	14.5°

1.5 to ensure end-wall effects could be ignored and the midspan flow assumed to be fully two-dimensional [9].

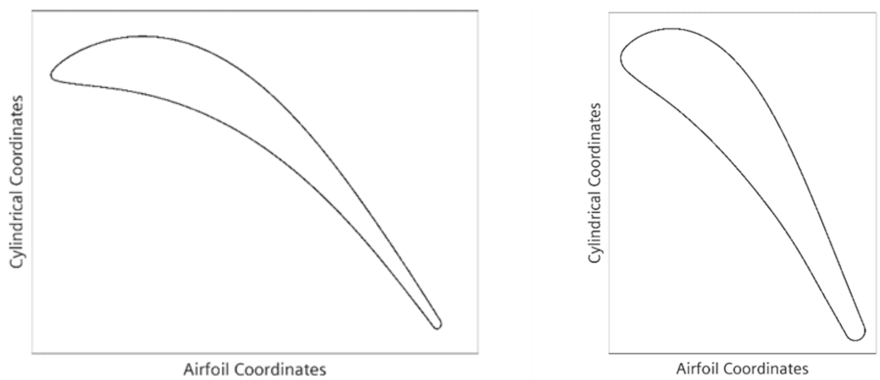

(a) Profile Used by Sooriyakumaran (b) Profile Used by Sieverding

Figure 4.2: Airfoil normalized profiles.

Figure 4.3 shows the computational domain used for this study. The inlet plane was positioned 1.5 axial chord lengths upstream of the airfoil leading edge to ensure uniform and fully developed flow. The extent of the outlet boundary, positioned 7 axial chord lengths downstream of the trailing edge, was chosen specifically for the limit and supercritical loading conditions to ensure numerical reflections did not influence predictions near the evaluation area [10]. The evaluation plane is taken to replicate the experiment used for validation and is positioned 1.5 axial chord lengths downstream of the airfoil leading edge. The top and bottom surfaces located a half pitch above and below the airfoil surface were periodic with a one-to-one mesh connectivity. Similarly, the positive and negative spanwise planes used for 3D predictions were

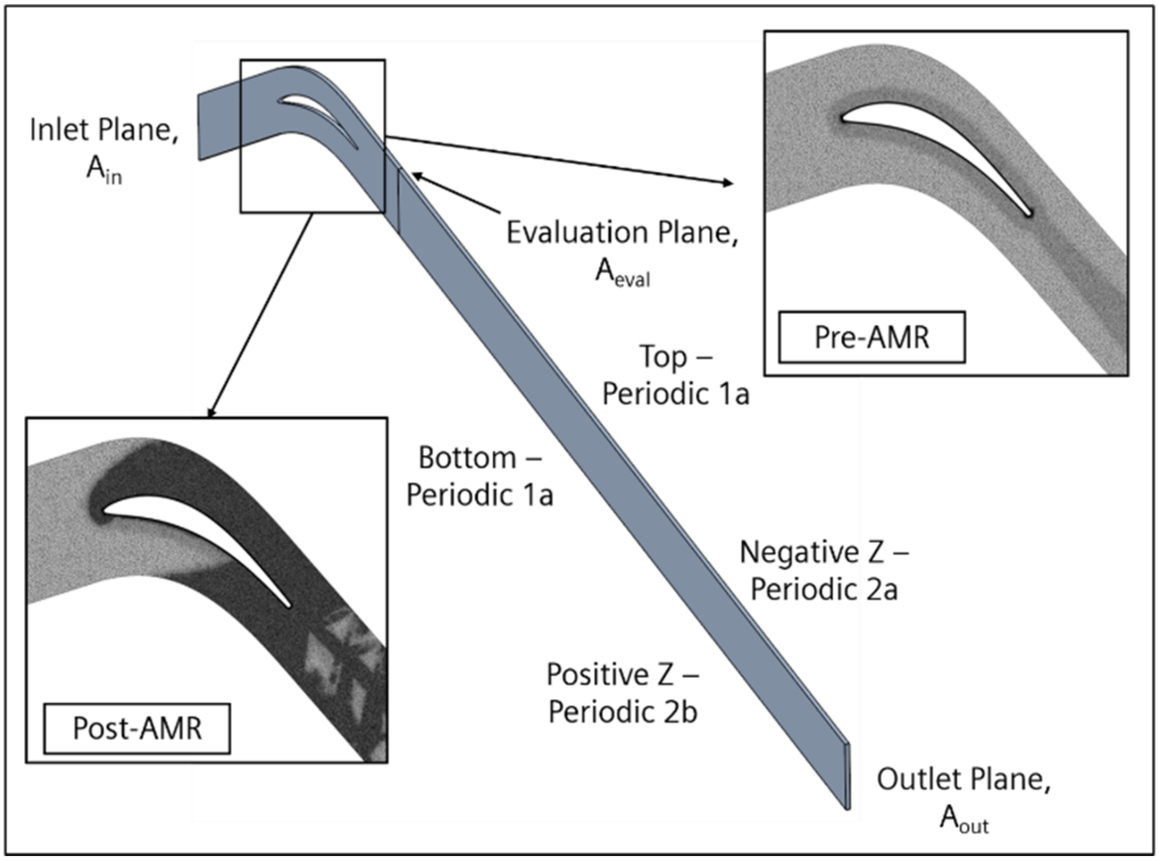

Figure 4.3: Computational domain and grid.

periodic with a total thickness of 10% of the airfoil chord and one-to-one connectivity.

4.2.2 Boundary and Initial Conditions

Boundary conditions used were set to replicate the experimental conditions of Sooriyakumaran [7]. The inlet boundary was prescribed a constant total pressure and total temperature, the outlet boundary an average static pressure, the top and bottom along with the positive and negative spanwise extents were set as periodic, and the airfoil surface a smooth, no-slip adiabatic wall. Incidence angle was set to 14°, and inlet turbulence intensity and length scale were set to 4% and 10% of airfoil pitch, respectively. Outlet average static pressure was adjusted depending on the desired inlet-total to outlet-static pressure ratio. Reynolds number based on the velocity at the evaluation plane and the true chord was $Re_c \sim 1.0 \times 10^6$.

The inlet conditions were used to initialize the RANS simulations. However, it should be noted that these simulations employed grid sequencing, so the domain initialization did not significantly influence the convergence rate. Each transient modeling approach was initialized with the respective RANS solution. For example, the URANS, DES and model free simulations for the critical loading condition were initialized using the RANS converged critical loading solution. A detailed description of the grid sequencing process has been documented by Owen [10].

4.2.3 Modeling Strategies

Although it is well known that the flow within a turbine blade passage is intrinsically unsteady due to vortex formation around the trailing edge, RANS modeling is the most extensively used simulation method in the gas turbine industry due to lower computational cost [11]. The unsteady RANS (URANS) modeling approach provides an improvement to the RANS method by stepping the solution in time to capture vortex formation and other transient phenomena with the smallest amount of increased computational effort. A further improvement in modeling capability is the Detached Eddy Simulation (DES) approach which combines URANS and Large Eddy Simulation (LES) strategies [12].

As mentioned, DES is a hybrid modeling approach that uses a RANS solution within the boundary layer and irrotational flow regions while the detached and freestream flow areas are solved using a modified LES. The LES methodology used is dependent on the specific DES model; here the SST k-omega formulation, obtained by modifying the dissipation term in the transport equation for turbulent kinetic energy, was employed to capture the unsteady separated regions. The delayed DES formulation (DDES) was used to enhance the ability of the model to distinguish between the LES and RANS regions [12].

Lastly, to avoid the empirical nature of the turbulence formulations as well as to ensure simulation fidelity, we tried to solve the flow field using an approach which does not rely on any turbulence modeling approaches. This methodology was similar to a direct numerical simulation approach; however, the simulation domain was kept as two-dimensional. Therefore, the authors have termed this as a pseudo-DNS or model free strategy. Using the results from the URANS simulation the Kolmogorov and Taylor length scales were estimated to be of the order 10^{-5} and 10^{-4} meters respectively. Using these estimates it was determined that the average grid size was roughly half the Taylor length scale and roughly ten times the Kolmogorov length scale. This was determined to be sufficient based on previous numerical investigations [13, 14].

All simulations employed a coupled, implicit compressible algorithm to solve the equations for mass, momentum, and energy. Discretization was second order for the source and diffusion terms for all methods except DES, which was a hybrid second-order upwind/bounded central-differencing scheme. All models used a second-order upwind scheme for calculation of the convection terms for the momentum and turbulence equations. The inviscid, convective fluxes were calculated using Liou's AUSM+ flux-vector splitting scheme [15]. The Algebraic Multi-Grid (AMG) linear solver with a V-cycle, Gauss-Seidel relaxation scheme and bi-conjugate gradient stabilizer acceleration method were employed [16].

4.2.4 Convergence Criterion and Time Step

All precursor RANS solutions were run until the flow had reached full convergence such that the normalized residuals of all transport quantities were steady and dropped to four orders of magnitude; in addition, the local total pressure loss coefficient did not show fluctuations over ± 0.0001 for 1500 iterations which typically occurred around 3500 iterations.

To ensure minimal influence of numerical errors as well as to improve the quality and run-time of each transient simulation an adaptive time stepping algorithm was used for each transient simulation. The adaptive time-stepping algorithm adjusts the time-step automatically during the run to obtain a user specified temporal resolution

Table 4.2: Average required time step.

Model Strategy	Loading Condition	Average Time Step (seconds)
Model Free (MF)	Critical	$6.21 \times 10^{-}8$
	Sublimit	$6.14 \times 10^{-}8$
	Limit	$5.24 \times 10^{-}8$
	Supercritical	$4.87 \times 10^{-}8$
URANS	Critical	$7.04 \times 10^{-}8$
	Sublimit	$6.45 \times 10^{-}8$
	Limit	$5.73 \times 10^{-}8$
	Supercritical	$4.92 \times 10^{-}8$
DES	Sublimit	$2.85 \times 10^{-}8$
	Limit	$2.69 \times 10^{-}8$

throughout the domain. Here an upper limit to the convective CFL number of 0.9 was selected as the criterion to determine the solution time step. Table 4.2 shows a summary of the mean time-step sizes for each simulation. The required time step to maintain sufficient temporal accuracy is dependent both on the loading condition and modeling strategy employed. The range of time step size was found to be 2.6×10^{-8} to 7.0×10^{-8} seconds.

4.2.5 Grid Description and Convergence

As previously mentioned all transient simulations were initialized using a RANS solution. The grid employed for each RANS simulation was generated through an adaptive griding internal algorithm detailed next.

$$\text{If} \quad \left| \frac{\nabla\phi - \nabla\phi_{min}}{\nabla\phi_{max} - \nabla\phi_{min}} \right| > 0.01 \quad \text{Area} \rightarrow \max\left(\frac{A_o}{2}, A_{LPL}\right) \tag{4.1}$$

Equation 4.1 shows the governing process of the adaptive mesh refinement scheme. Here ϕ denotes the scalar quantity of interest (absolute total pressure, total temperature, density, turbulent kinetic energy, turbulent eddy viscosity and the specific dissipation rate of turbulence), A_o the original cell area prior to adaptation, and A_{LPL} is the area of the last prism layer. This was used as the limiter of refinement to ensure a one-to-one ratio between the prism layers and the core grid.

As shown previously [10], the adapted grid algorithm proved robust in capturing the blade loading of four different transonic turbine airfoils at sublimit loading conditions, proving the ability to accurately capture the trailing edge shock system and the subsequent influence on the adjacent airfoil suction side boundary layer. Table 4.3 and Figure 4.4 shows an example of the grid density evolution throughout the AMR process.

Table 4.3: Adaptive mesh refinement cell count - example.

AMR Cycle	Number of Elements	Percent Increase in Elements
0	7.2×10^4	
1	1.0×10^5	40%
2	1.4×10^5	38%
3	1.8×10^5	28%
4	2.2×10^5	24%
5	2.6×10^5	19%
6	3.0×10^5	15%
7	3.3×10^5	11%
8	3.6×10^5	9%
9	3.7×10^5	1%

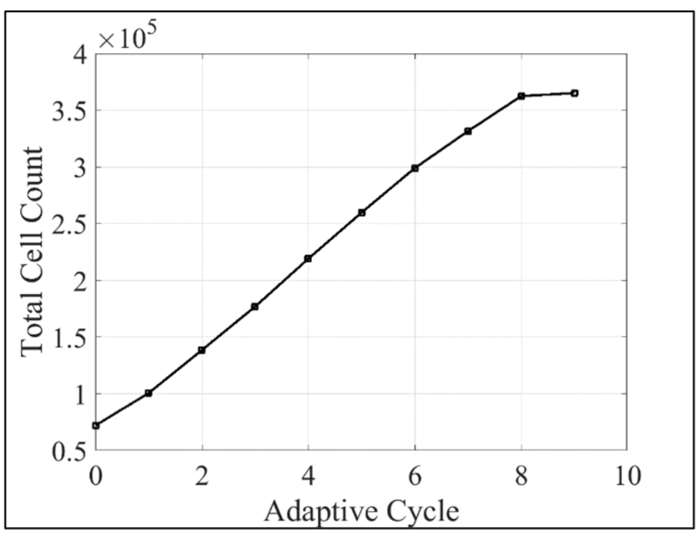

Figure 4.4: Adaptive mesh refinement example.

Each simulation began with a baseline mesh of roughly 70,000 elements. The core grid comprised unstructured, polyhedral elements with prismatic layers along the airfoil surface. The distribution of prisms normal to the airfoil remained constant with 40 layers, a hyperbolic growth rate, a near wall thickness achieving a max y+ less than 0.5, and a total thickness equal to 40% of the trailing edge thickness. It should be noted that the distribution along the tangential direction of the airfoil surface was changed with increasing refinement to maintain an aspect ratio of less than two. Nine AMR cycles were used for each RANS simulation, and additional AMR cycles only proved to increase computational resources unnecessarily as the increase in number of elements was less than 1%.

Although this grid methodology provided a grid independent solution for the RANS simulation approach there was no guarantee that it would suffice for the other models. Therefore, an additional grid independent study was performed for each loading condition and transient modeling strategy. Using the adapted mesh from the RANS solution as a baseline, the grid was isotropically refined by 50 and 25%, roughly doubling the total cell count in each case.

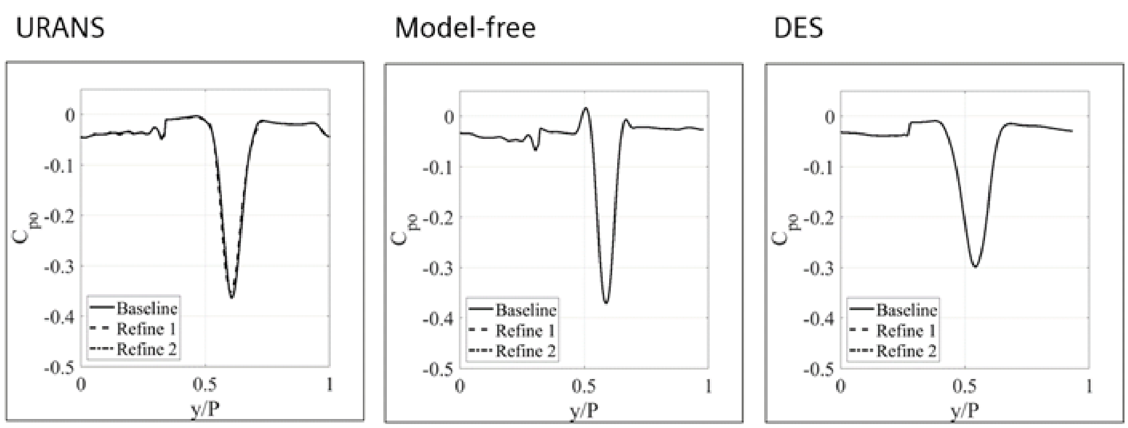

Figure 4.5: Mesh convergence example - downstream total pressure loss distribution - limit loading.

Figure 4.5 illustrates the differences in downstream predicted total pressure loss for each grid level. As can be seen, the change in total pressure loss distribution is minimal between grid refinements, producing a change in mixed-out total pressure loss coefficient of less than 2%. It should be noted that a grid verification procedure was applied to each loading condition for each transient strategy; the image below shows an example. As there was no significant improvement in using the refined grids the adapted grid of the RANS solution was used for each transient simulation.

4.2.6 2D/3D RANS and URANS Comparison

Prior to the main results section, the authors would like to highlight the differences between 2D and 3D RANS and URANS simulations. Given that the computational domain is modeled as periodic in the spanwise direction, the flow is expected to be similar for both 2D and 3D approaches. Figure 4.6 shows the surface isentropic Mach number distribution as well as the downstream pitch-wise total pressure loss distribution for both 2D and 3D simulations. Solid lines are the RANS predictions, dashed lines are the URANS predictions, and solid black squares are experimental data taken from the work of Sooriyakumaran.

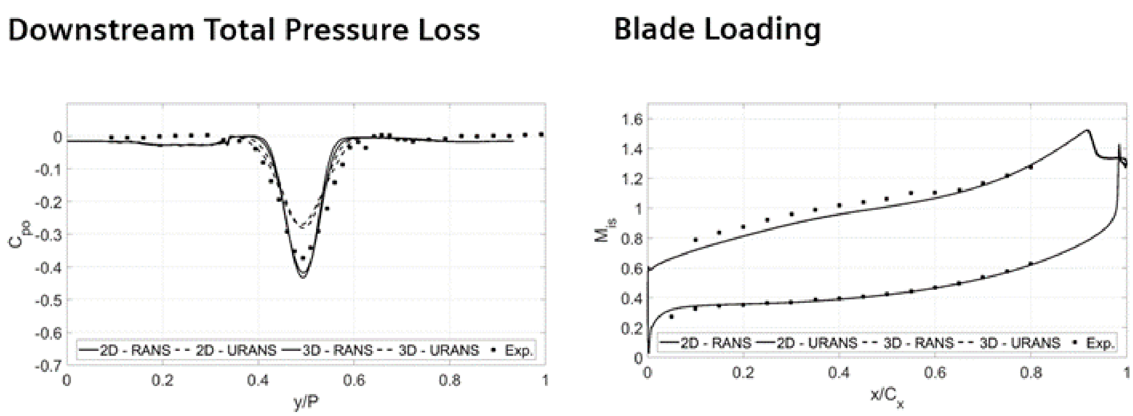

Figure 4.6: 2D and 3D RANS and URANS comparison - downstream total pressure loss and blade loading.

Looking at the blade loading distribution, it is clear there is no noticeable difference between 2D and 3D simulations. On the pressure side the flow accelerates consistently until the trailing edge expansion while the suction side shows a slight deceleration at the leading edge followed by nearly constant acceleration until the point of shock impingement. Following the shock/boundary layer interaction there is a period of nearly constant pressure until the trailing edge. This flow pattern is consistent between modeling domains.

Similarly, the downstream total pressure loss distribution shows only minor deviations between 2D and 3D approaches. The RANS simulations predict a significantly higher loss distribution in the middle of the wake with smaller width compared to URANS. As no major differences were seen between 2D and 3D results for both RANS and URANS modeling approaches, the remainder of the paper will only include the results from the 2D simulations.

4.3 Results

4.3.1 Validation

As previously mentioned, two transonic turbine airfoils were used for numerical validation. Both airfoil geometries have been previously described and are shown in Figure 4.2. The total inlet to outlet static pressure ratio used by Sooriyakumaran was 2.25, a pressure ratio within the sublimit loading range, corresponding to an isentropic exit Mach number of 1.15 and for the profile used by Sieverding PR = 1.5, a subcritical loading condition corresponding to an isentropic exit Mach number of 0.79.

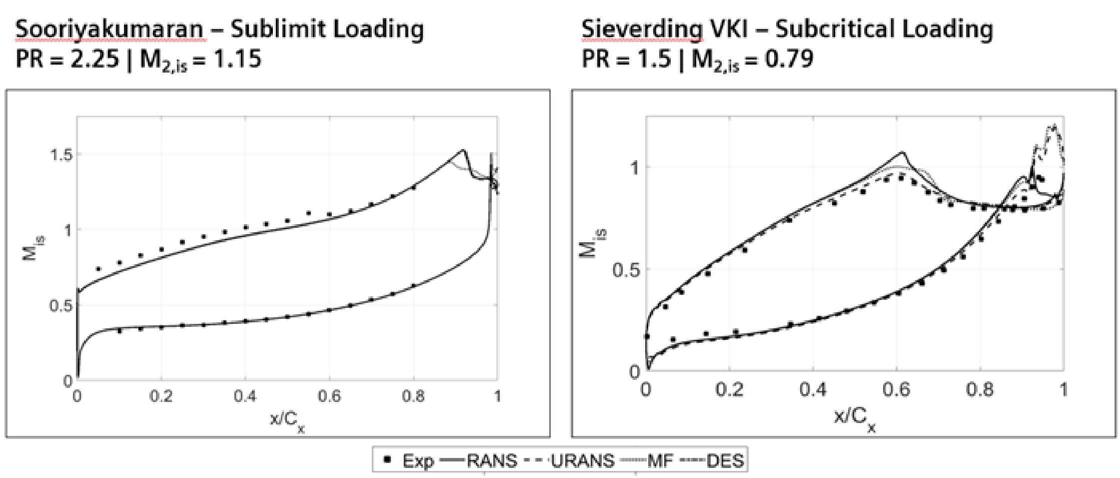

Figure 4.7: Surface isentropic Mach number distributions compared to experiment.

Figure 4.7 illustrates the predicted airfoil surface isentropic Mach number distribution for each profile compared to their respective experimental data. Extracted test information is shown as solid black squares while all simulation results are shown as various line distributions; RANS - solid lines, URANS - dashed lines, model free - dotted lines and DES - dashed dotted lines.

Overall distributions are predicted well for both profiles and loading conditions. Results for the profile taken from the work of Sooriyakumaran show nearly identical predictive capability for the full pressure surface as well as the majority of the suction surface. Differences arise along the suction surface at roughly 0.9 axial chord lengths (C_{ax}) aft of the airfoil leading edge, at which point the model free approach predicts a smearing of the shock impact on the suction surface boundary layer. This is a product of an oscillatory effect caused by the unsteady vortex shedding at the airfoil trailing edge, and additional details will be provided. Similarly, the predicted results for the profile used by Sieverding agree quite will with the experimental test data for the majority of the airfoil surface. Discrepancies between modeling approaches arise at the point of shock impingement along the suction surface similar to what is observed for the profile used by Sooriyakumaran. This is believed to be primarily a product of the unsteady propagation of vortices near the trailing edge.

Next a look at the downstream total pressure loss distribution for the profile used by Sooriyakumaran as well as the base pressure distribution of the profile used by Sieverding are presented in Figure 4.8. Focusing first on the loss distribution for the profile used by Sooriyakumaran, it is clear that neither the URANS nor the model free approach predict the correct minima of total pressure loss. The total wake width is slightly increased compared to the experimental results and the free stream losses are significantly over predicted. This is similar for all modeling approaches; however, in contrast both the RANS and DES strategies show good agreement with the location and magnitude of the loss minima. The DES approach shows the best

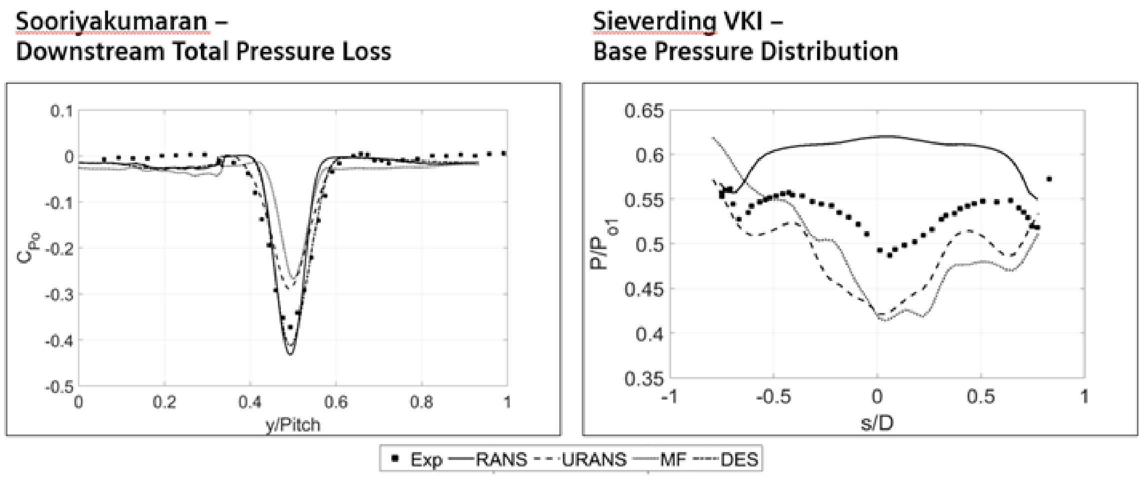

Figure 4.8: Left: Pitchwise total pressure loss distribution compared to experiment | Right: Trailing edge base pressure distribution compared to experiment.

overall agreement of the methods considered, predicting a slightly wider wake width than the RANS approach while maintaining the correct magnitude of loss at the wake centerline.

As described by Sieverding the pressure distribution along the trailing edge is characterized by three pressure minima: two caused by the Prandtl-Meyer expansion around the suction and pressure sides prior to flow separation and a third at the trailing edge center caused by the enrolment of the separating shear layers into a vortex core [17]. In this case, none of the modeling approaches seem to be able to replicate the complex flow phenomena occurring at the trailing edge exactly. RANS modeling shows the largest discrepancy, predicting first a sharp rise in base pressure following the separation of the suction and pressure side shear layers followed up by a large pressure plateau towards the trailing edge centerline. The URANS approach is the only method to successfully predict the location of the three pressure minima, although the magnitude is significantly lower than the experimental data. The model free approach was unable to predict the pressure side expansion location and subsequent pressure minima, but the location of the centerline and suction side minima are correctly captured. It should be noted that the predicted base pressure distributions shown above are similar to previous numerical results using URANS and RANS methods [11].

4.3.2 Mean Flow

Figures 4.9 and 4.10 show the time averaged, mixed-out total pressure loss coefficient as well as the mass flow averaged total flow turning at the evaluation plane for each of the loading and modeling strategies considered. All methods, with the exception of the URANS approach, predict a gradual rise in mixed-out total pressure loss coefficient from critical to limit loading. The sharp rise in loss prediction for the URANS model at the critical loading condition is explored in detail later; however, in summary this is due to the inability of the URANS method to accurately predict the transition from trailing edge dominated vortex formation to shock dominated vortex formation.

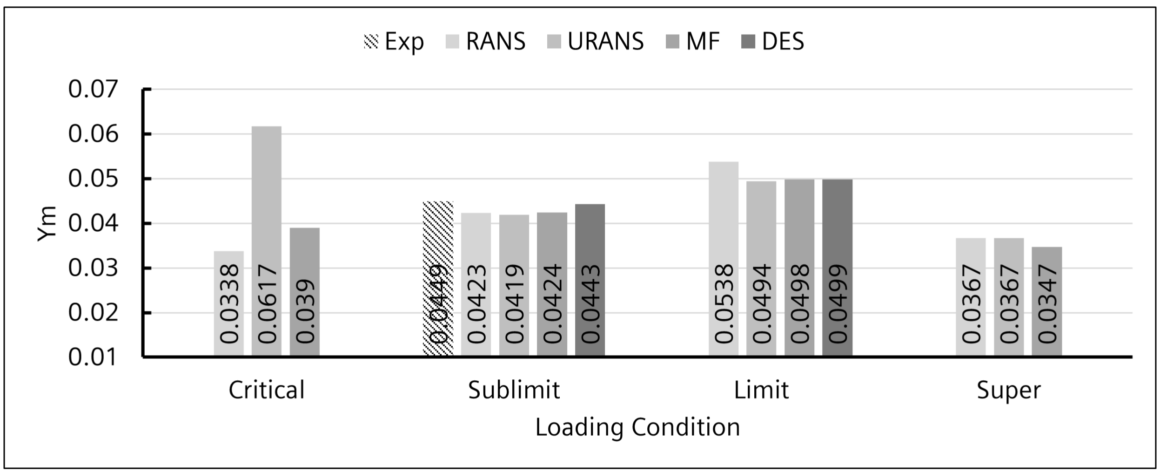

Figure 4.9: Time-averaged, mixed-out total pressure loss coefficient at each loading condition.

For all methods considered there is a sharp decline in loss coefficient from limit to super critical loading. This was unanticipated, as the total pressure loss was expected to increase with pressure ratio [1, 3, 5]. However, as the passage becomes fully choked, the oblique Trailing Edge Pressure Side Shock (TEPSS) caused by the rapid expansion around the trailing edge, completely clears the adjacent airfoil base pressure region

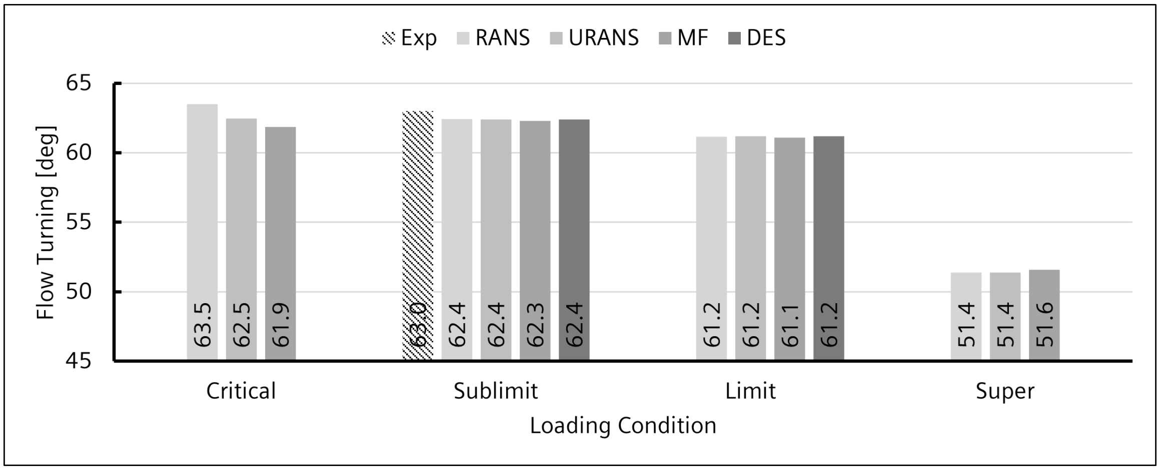

Figure 4.10: Mass-flow averaged total flow turning at each loading condition.

resulting in reduced total pressure loss as well as flow turning. The interactions of the shock system with the blade boundary layer and wake structures becomes small and thus the predicted total pressure loss is reduced. Although a decrease in total pressure loss is desirable, there is a significant detriment in the ability of the airfoil to produce the desired work output, as this is directly related to the total flow turning. Furthermore, the large change in outlet flow angle can drastically decrease the efficiency of downstream blade rows through a change in incidence angle. A quick interpolation of results from Owen [6], shows that for a change of incidence by less than 2 degrees, such as the change from critical to limit loading, total pressure loss is expected to rise by roughly 1%. However, as the incidence angle is significantly changed ($> 9°$), such as is the case for supercritical loading, the estimated loss increase is roughly 25%. Clearly this is not desirable, highlighting the importance for aero designers to understand the limit and supercritical loading conditions.

Shown in Figure 4.11, are the predicted blade loading distributions for each modeling strategy at each loading condition. The available experimental data of Sooriyakumaran has been included for completeness. As a reminder experimental test results are only available for the sublimit loading condition.

Blade loading distributions along the airfoil pressure surface as well as the suction

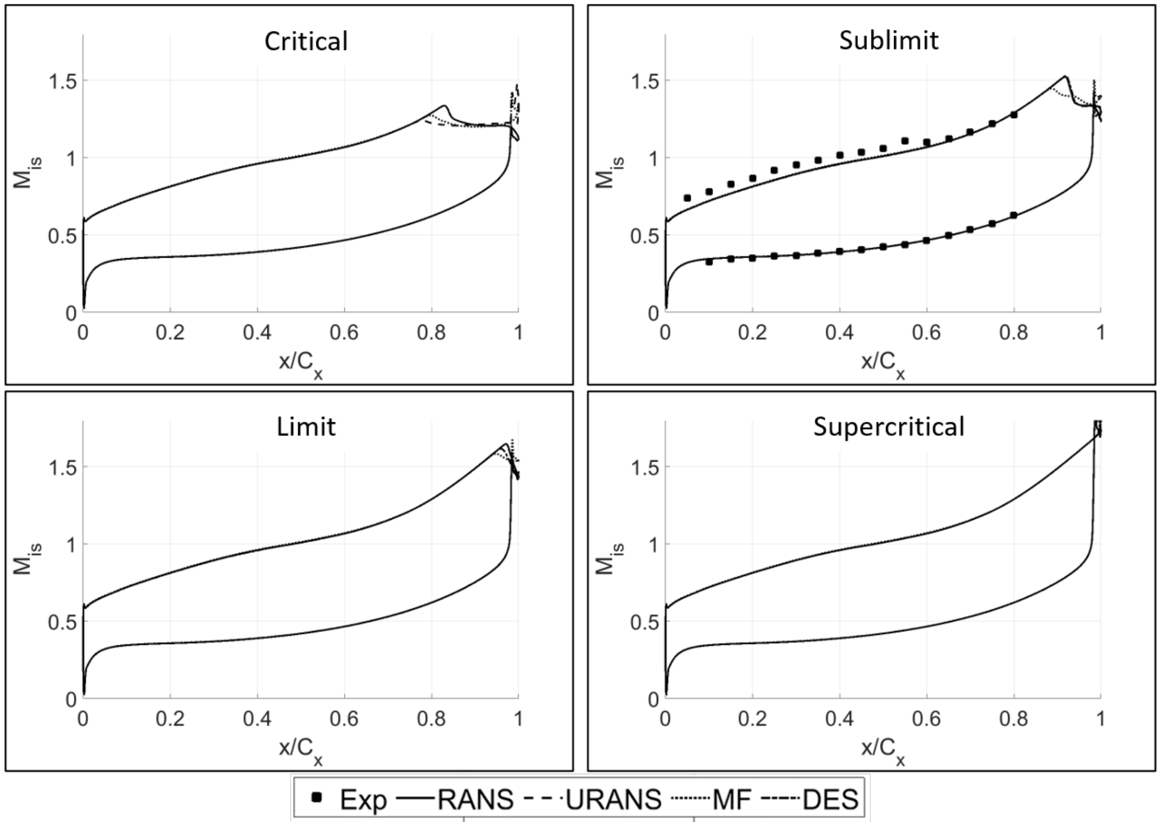

Figure 4.11: Surface isentropic Mach number distributions at each loading.

surface prior to the location of shock interaction ($\sim 0.8C_{ax}$ for critical loading and $\sim 0.9C_{ax}$ for sublimit) are predicted to be identical across loading conditions and modeling approaches. This is a result of flow choking cause by the trailing edge pressure surface shock (TEPSS). The effects of unsteady shock propagation and trailing edge vortex shedding are found to have a minimal effect on the flow field and subsequent blade loading. Downstream of the pressure side shock, highlighted in Figure 4.12, there are clear differences in the ability of each modeling approach to predict the shock propagation and subsequent shock/boundary layer interaction.

Unsteady propagation of the TEPSS caused by the interaction of the shock system with the trailing edge vortex shedding process causes the surface isentropic Mach number distribution to change. As the pressure surface shear layer is shed and rolled into a vortex core the shock system is weakened, resulting in an oscillatory shock effect.

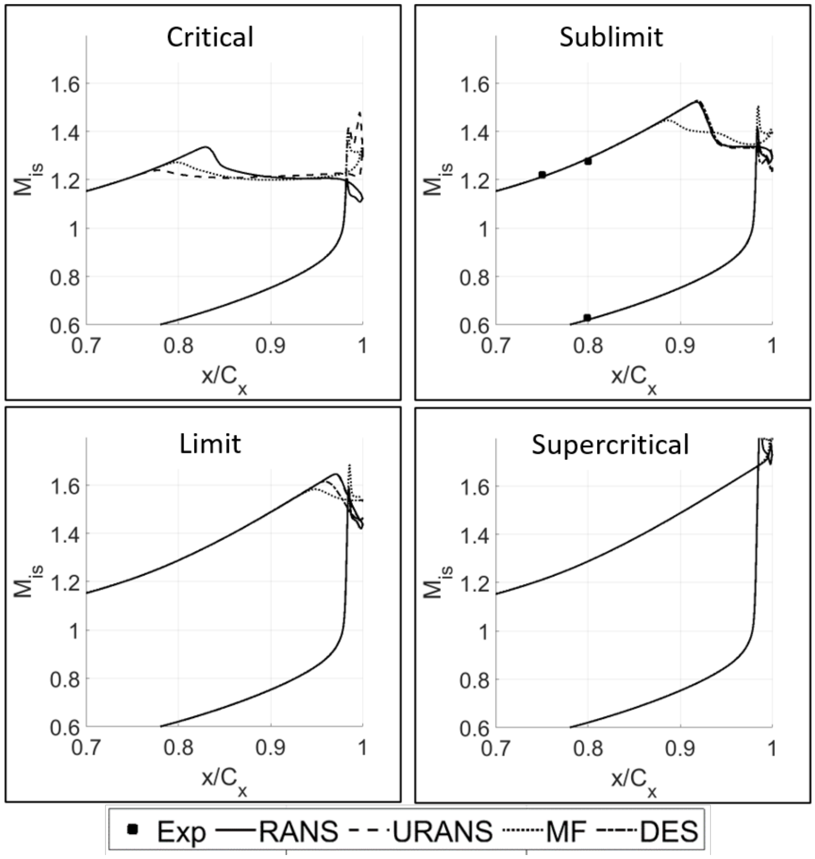

Figure 4.12: Trailing edge surface isentropic Mach number distributions at each loading.

This system is then propagated downstream towards the adjacent airfoil causing a subsequent shock-boundary layer interaction which, in a time averaged sense, results in a smoothing of the shock impact.

This is most significant at lower pressure ratios where the predicted base pressure region is smaller, such as the critical loading condition. As illustrated through numerical Schlieren flow visualizations in a later section, the pressure and suction side shear layers do not achieve sufficient momentum to create a well-established base pressure region. This causes the trailing edge pressure side shock to form nearer the airfoil trailing edge resulting in significant influence from the vortex formation process. As the pressure ratio is increased, the base pressure region becomes established and causes vortex formation to occur downstream of the trailing edge shock system.

All modeling approaches, with the exception of the model free strategy show minimal oscillation of the shock location as the base pressure region becomes established. Therefore, RANS/URANS and DES all predict similar loading distributions for the sublimit loading conditions and above. As will be shown later, the model free approach predicts a much smaller base pressure region than the others, as is apparent in the base pressure distribution as well as flow visualizations. At supercritical loading all models predict near identical surface pressure distributions as the flow upstream of the TEPSS is fully choked and temporally stationary.

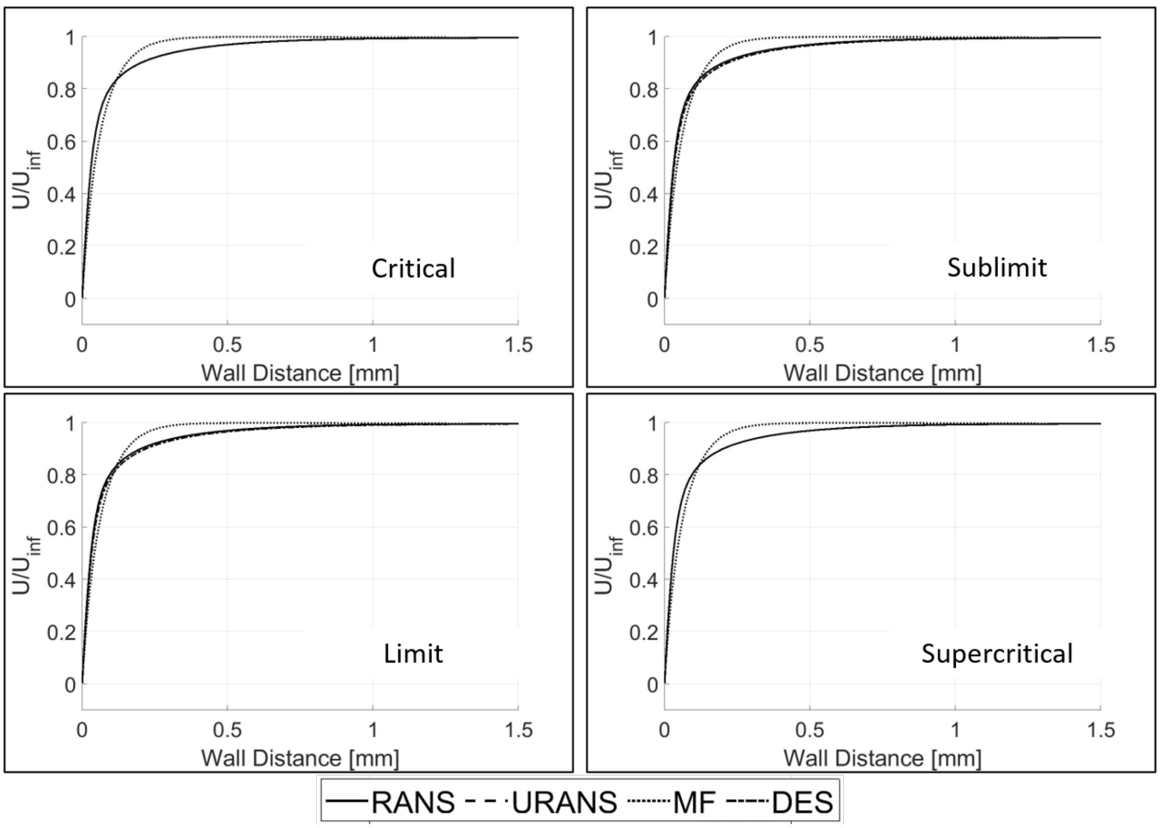

Figure 4.13: Pressure side trailing edge boundary layer profiles at each loading condition.

To further investigate the causes of the differences in vortex formation and subsequent downstream total pressure distributions, plots of the wall normal velocity on both the pressure and suction sides at 98% chord are presented in Figures 4.13 and 4.14. Due to the strong acceleration along the pressure surface, the boundary layer near the trailing edge of the pressure side is predicted to be laminar and near identical across loading conditions. The flow in this region is fully choked; therefore, any increase in pressure ratio only changes the flow downstream of the trailing edge pressure surface shock. The total boundary layer thickness, estimated as 99% of the freestream velocity, was predicted to be roughly 0.92 mm for the RANS, URANS and DES simulations and 0.31 mm for the model free approach.

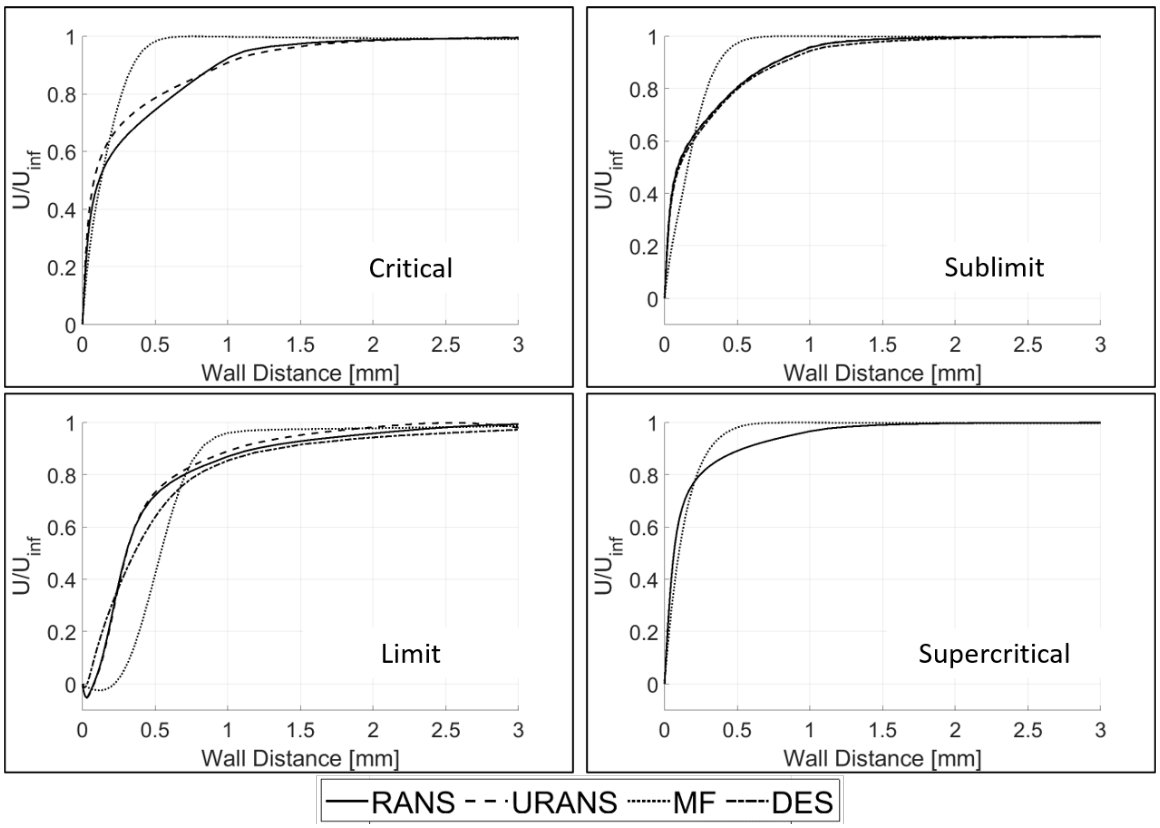

Figure 4.14: Suction side trailing edge boundary layer profiles at each loading condition.

Unlike the pressure side, the suction side of the airfoil surface shows a strong dependence on load condition and modeling strategy, specifically for the limit loading condition. A summary of the predicted boundary layer thickness for each condition and strategy is shown in Table 4.4. At the lowest pressure ratio, the flow is clearly attached and turbulent with the exception of the model free strategy which alludes to a transitionary state. Similar to the pressure side RANS, URANS and DES approaches all show similar boundary layer thickness and distribution for the sublimit loading condition with a total thickness of roughly 1.5 mm.

Table 4.4: Suction side boundary layer thickness summary (mm).

Modeling Approach	Critical	Sublimit	Limit	Supercritical
RANS	2.35	1.49	2.80	1.46
URANS	2.35	1.49	2.16	1.46
MF	0.54	0.60	3.46	0.54
DES		1.49	2.67	

As the pressure ratio is increased to limit loading the boundary layer profile shows a period of separation. This is a product of the influence of the trailing edge pressure side shock interacting with the suction side shear layer that forms one side of the base pressure region. The shock/base pressure interaction causes acoustic waves to propagate upstream creating a brief period of instability in the boundary layer. Although each modeling strategy shows separation, the magnitude is significantly different between strategies with the model free approach showing the largest region of flow recirculation. The approximate size and location of the period of separation requires a deeper look at the full flow picture and is investigated further with flow visualizations later in this report.

Figure 4.15 shows the predicted base pressure distribution for each modeling strategy and loading condition. For critical loading, the flow at the trailing edge is characterized by attached vortices formed by the alternating shedding of the pressure and suction side shear layers. The trailing edge pressure surface shock gains sufficient expansion to create an established base pressure region, resulting in a period of nearly constant pressure towards the trailing edge centerline. Local pressure minima are seen at the locations of the shear layer separation points and are a result of the Prandtl-Meyer expansion around the trailing edge. All modeling approaches predict the general trend of the pressure distribution similarly, although the unsteady formulations show a significantly lower base pressure than the steady RANS simulation for

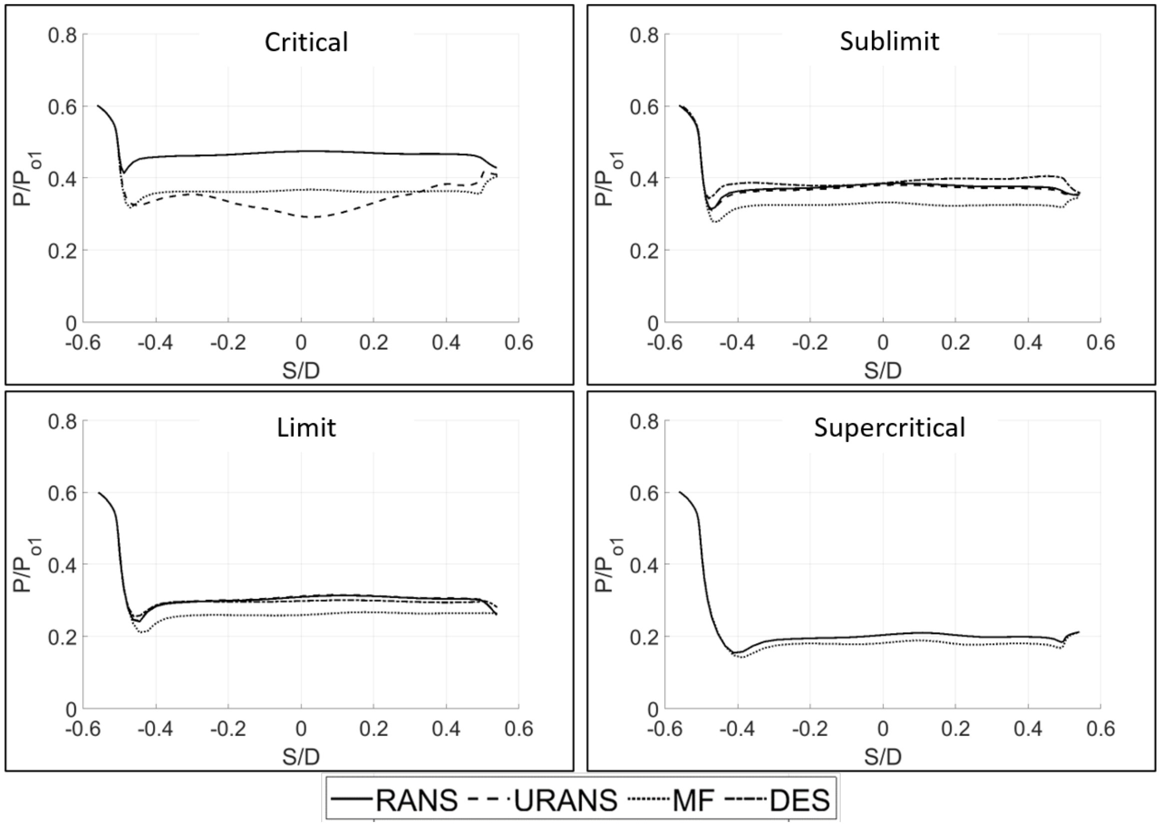

Figure 4.15: Base pressure distributions at each loading condition.

the critical loading condition. As the pressure ratio is increased towards limit loading the magnitude of the base pressure is lowered and is consistent for all modeling approaches. A summary of the normalized time and surface averaged base pressure is listed in Table 4.5 and presented alongside the well-known base pressure correlation created by Sieverding [18] in Figure 4.16.

Results are distinguished as follows: RANS simulations as red squares, URANS simulations as purple diamonds, model free simulations as green triangles and DES as orange circles. The solid lines show the correlation by Sieverding for the geometric properties nearest the investigated airfoil and the dashed line signifies equal base and downstream static pressures to help with analysis.

As the total pressure ratio is increased the predicted base pressure decreases for all modeling approaches. During critical loading each unsteady model predicts a

Table 4.5: Area averaged base pressure summary.

Model Strategy	Loading Condition	P_{s2}/P_{o1}	P_b/P_{o1}
RANS	Critical	0.498	0.466
	Sublimit	0.444	0.374
	Limit	0.408	0.300
	Supercritical	0.257	0.194
URANS	Critical	0.496	0.352
	Sublimit	0.444	0.370
	Limit	0.408	0.302
	Supercritical	0.257	0.194
MF	Critical	0.496	0.362
	Sublimit	0.444	0.323
	Limit	0.408	0.257
	Supercritical	0.259	0.176
DES	Sublimit	0.444	0.390
	Limit	0.408	0.302

significantly lower base pressure than steady RANS. As the pressure ratio is increased to sublimit and limit loadings the base pressure is predicted similarly for each of the wall modeled simulations, suggesting the flow is statistically stationary within the base pressure region. The model free approach predicts a much lower base pressure than the others for each of the loading conditions. This is a product of the size of the base pressure region, which is directly related to the magnitude and state of the pressure and suction side boundary layers near the trailing edge. As shown previously, the predicted model free boundary layers are much smaller than the other approaches. This causes the shear layer separation at the trailing edge to occur more rapidly, creating a stronger pressure side expansion. As the expansion becomes stronger the subsequent base pressure becomes lower.

Figure 4.17 shows the predicated time averaged total pressure loss distributions for each pressure ratio and modeling strategy. As observed in the mixed-out mass flow averaged total pressure loss coefficient, downstream losses increase with an increase in pressure ratio until supercritical loading. This is due to a combination of increased wake and freestream losses. During critical loading freestream losses are predicted to

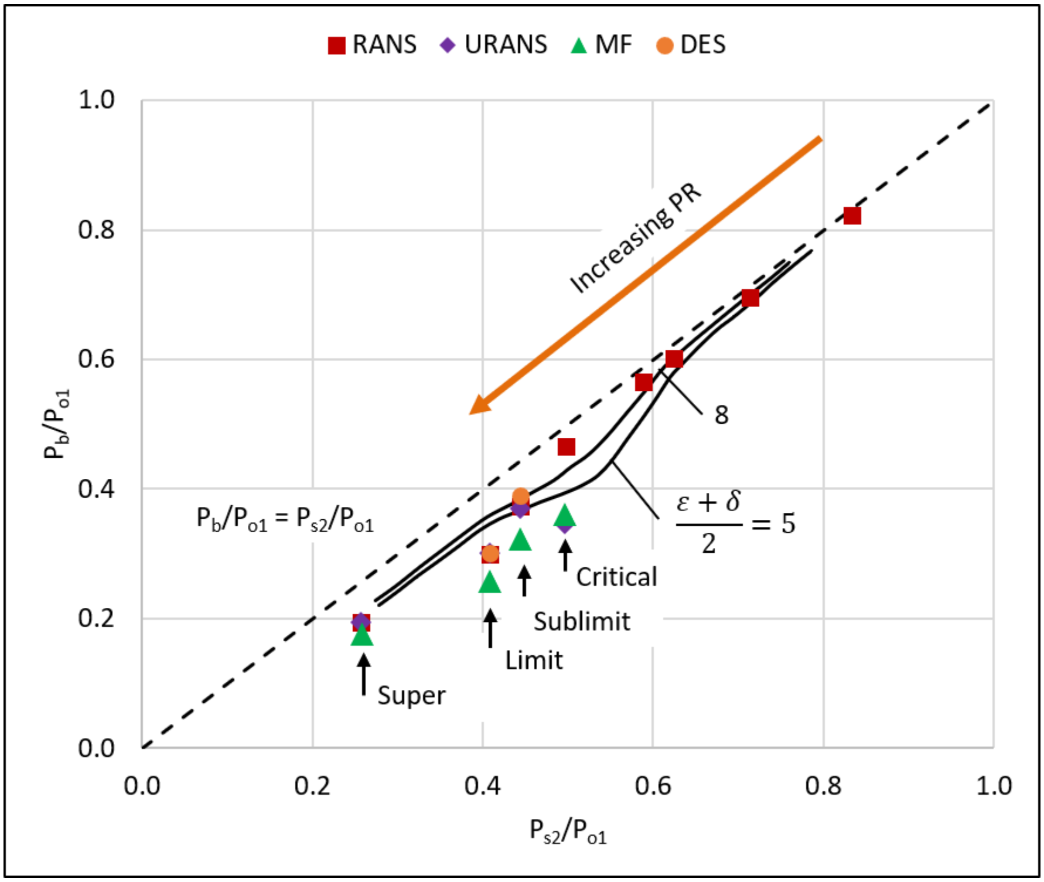

Figure 4.16: Comparison with the base pressure correlation proposed by Sieverding.

be small compared to wake losses as a result of how the vortices are being shed from the trailing edge. When the base pressure region is attached to the trailing edge, vortices shed quickly leading to increased mixing and wake losses.

Increase of the pressure ratio to sublimit loading causes the flow expansion around the trailing edge to become stronger, leading to a larger and more established base pressure region that pushes vortex formation downstream as well as decreases the frequency of the vortex shedding. Although there is a reduction in wake losses, shock and freestream losses are increased. This is a product of the strong oblique trailing edge shock system, with the pressure side shock interacting with the suction surface boundary layer and the suction side shock propagating through the downstream wake. For limit loading the loss is further increased due to the complex flow near the trailing edge and base pressure region. As the TEPSS passes through the base pressure

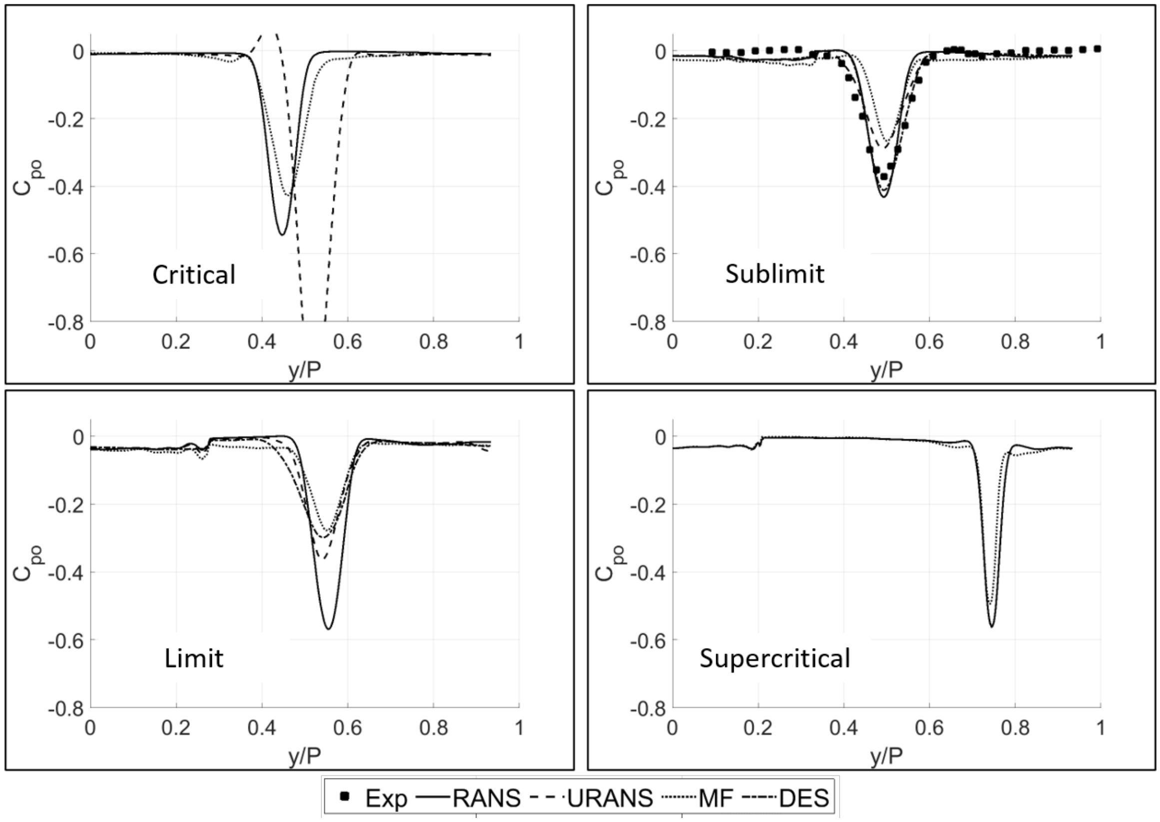

Figure 4.17: Downstream total pressure loss distributions at each loading condition.

region acoustic waves propagate upstream along the suction surface followed by flow separation and increased wake width and depth. Also included is the impact of the suction side shock on the downstream wake profile. Predictions for super critical loading show that as the TEPSS departs the base pressure region, the influence of vortex formation becomes small and freestream losses are reduced for the majority of the domain.

Looking at the difference in modeling approaches, it is clear that the RANS simulations predict the smallest wake width and largest wake depth of the modelling strategies considered for all loading conditions. This is due to a lack of vortex/shock interactions. With the exception of critical loading, the URANS and model free approaches show a much smaller wake depth; however, due to vortex formation they predict an increase in wake width compared to RANS. The DES approach, shown only for the sublimit and limit loading conditions, shows the widest wake prediction as well as best correlation with available experimental data.

During critical loading the URANS method predicted an unrealistic downstream loss profile. It should be noted the authors preformed a rigorous grid refinement study as well as manual time step adjustment to repair the downstream loss prediction. It was concluded that the URANS method failed to correctly predict the transition from near trailing edge vortex formation to shock trailing edge vortex formation at the edge of the base pressure region. Further analysis results are presented and discussed later in this paper.

4.3.3 Transient Phenomena

Shown in Figure 4.18 are the normalized power spectral densities of the mass flow averaged total pressure loss coefficient at the evaluation plane for the critical, sublimit and limit loading conditions. Supercritical loading is not presented as the loss coefficient for each modeling approach remained temporally constant. This is believed to be a result of the choking of the flow caused by the trailing edge pressure surface shock. As can be seen there is a peak energy that clearly defines the vortex shedding frequency for each modeling approach.

Table 4.6: Power spectrum analysis summary.

Model Strategy	Loading	Peak Freq. (kHz)	Strouhal #	Vortex Period (ms)
MF	Critical	70.2	0.279	0.014
	Sublimit	84.7	0.316	0.012
	Limit	63.0	0.226	0.016
URANS	Critical	60.3	0.241	0.017
	Sublimit	58.1	0.217	0.017
	Limit	60.7	0.217	0.016
DES	Sublimit	35.9	0.134	0.028
	Limit	46.2	0.165	0.022

A summary of the peak vortex frequency, calculated Strouhal number and vortex shedding period is given in Table 4.6. The Strouhal number was computed using

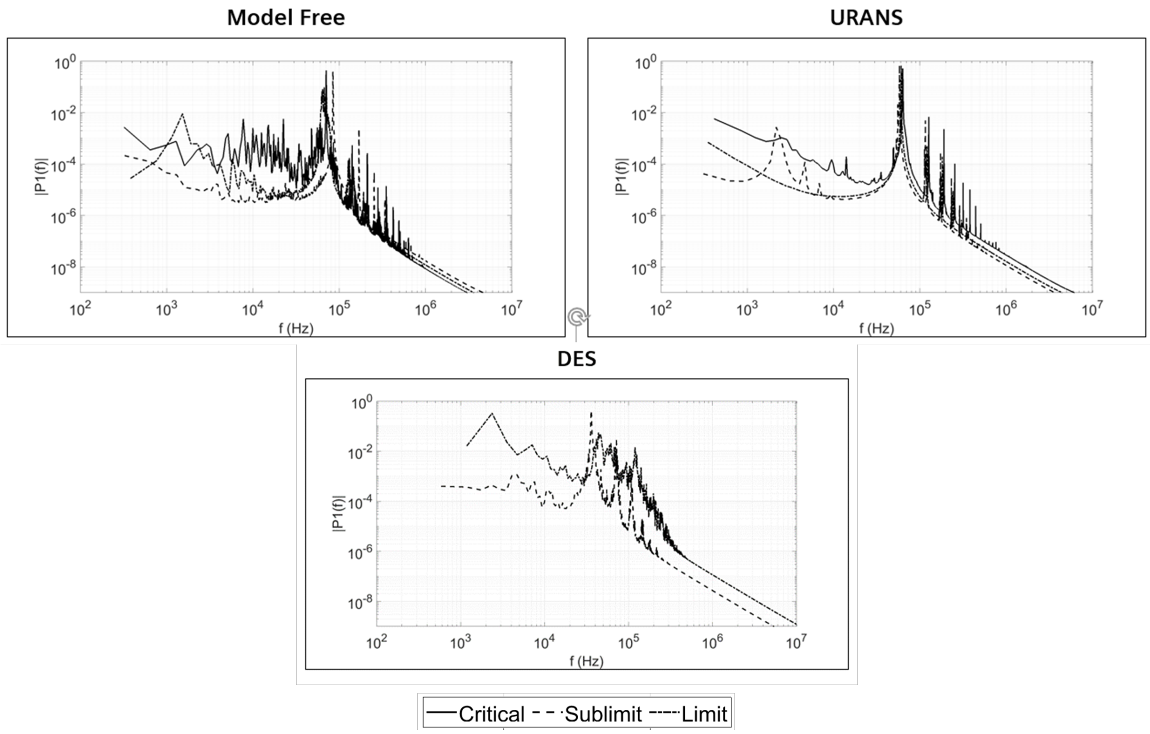

Figure 4.18: Power spectrum - mass-flow averaged total pressure loss coefficient.

Equation 4.2 with f_{vs} being the peak vortex shedding frequency, d_{te} the trailing edge diameter and $V_{2,is}$ the mass flow averaged isentropic flow velocity at the evaluation plane.

$$St = \frac{f_{vs} d_{te}}{V_{2,is}} \tag{4.2}$$

For each modeling strategy, the average adaptive time step required to produce a convective CFL number of less than 1 was smaller for higher total pressure ratios. Although there is a wide range of predicted Strouhal numbers between modeling strategies, they are all within the bounds of similar experimental and computational investigations [17]. The model free simulation shows a much higher predicted vortex shedding frequency than the other unsteady methods for all loading conditions, with a peak difference occurring during sublimit loading. As discussed previously, this is a product of the state of the trailing edge boundary layer. The results of the

URANS simulations predict lower Strouhal numbers than the model free approach; however, the DES simulations predict Strouhal numbers to be much lower than either of the other methods. To help clarify the causes of the differences in vortex shedding frequency between modeling strategies flow visualizations of the normalized density gradient at various phase states are presented in the following section.

4.3.3.1 Critical Loading

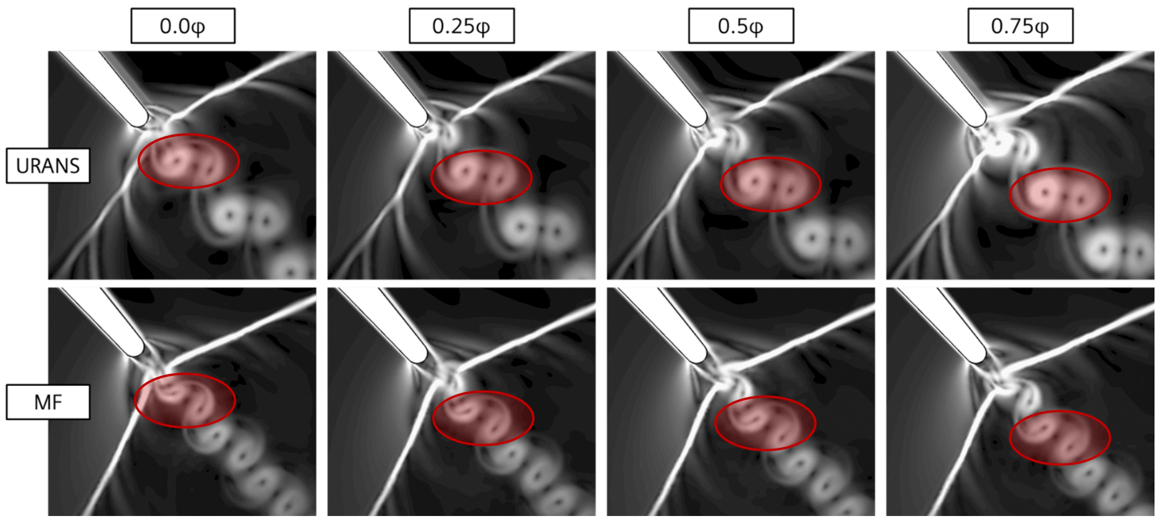

Figure 4.19: Normalized density gradient at the trailing edge - critical loading.

Figure 4.19 shows the URANS and model free visualizations of the instantaneous normalized density gradient for a full vortex shedding period. The left most images describe the point where the pressure side trailing edge vortex is initially shed and the right most image illustrates the point just prior to the next pressure side vortex period. Comparing modeling approaches, it is clear that the base pressure region, trailing edge shock structures and trailing edge boundary layers are predicted quite differently between methods.

The URANS approach shows a much smaller base pressure region, with vortex formation occurring very near the trailing edge surface. In contrast the model free approach predicts a larger base pressure region with the shock clearly forming at the coalescence of the trailing edge pressure and suction side shear layers. This difference between model predictions results in an increase in vortex shedding period as shown in Table 4.6. In agreement with previous experimental work [19, 20], both modeling approaches show the pressure side shear layer to dominate the vortex shedding process. As described by Han and Cox this is due to the rapid expansion around the pressure side trailing edge, resulting in vortex pairs that have been highlighted in red.

Overall, predictions of the trailing edge shock system are quite different between modeling approaches with the URANS method predicting both the pressure and suction side shocks to be approximately normal to the airfoil outlet metal angle, while the model free approach suggests a more oblique shock structure. As described by Sieverding et al. [8], pressure waves initiate from the point of boundary layer separation on both the pressure and suction surfaces. These waves impinge on the suction side boundary layer resulting in the smearing of the blade loading distribution seen in Figures 4.11 and 4.12. The location and angle of the shock formation is directly related to the boundary layer state at the trailing edge which is clearly different between modeling strategies and has been documented previously through wall normal velocity profiles.

4.3.3.2 Sublimit Loading

Figure 4.20 shows instantaneous predictions of the normalized density gradient for each modeling approach at the sublimit loading pressure ratio. As expected, each of the modeling strategies predicts an oblique trailing edge shock system that forms a well-established base pressure region. The flow expands rapidly around the trailing edge leading to a strong separated shear layer that coalesces into two distinct oblique shocks. The flow upstream of the shock is choked and therefore temporally stationary. The model free approach shows the only variation, although minute, of the flow prior to the suction surface shock. Referring back to the surface isentropic Mach number distributions presented in Figures 4.11 and 4.12, an explanation for the smearing of the model free shock impingement can be explained by highlighting the suction

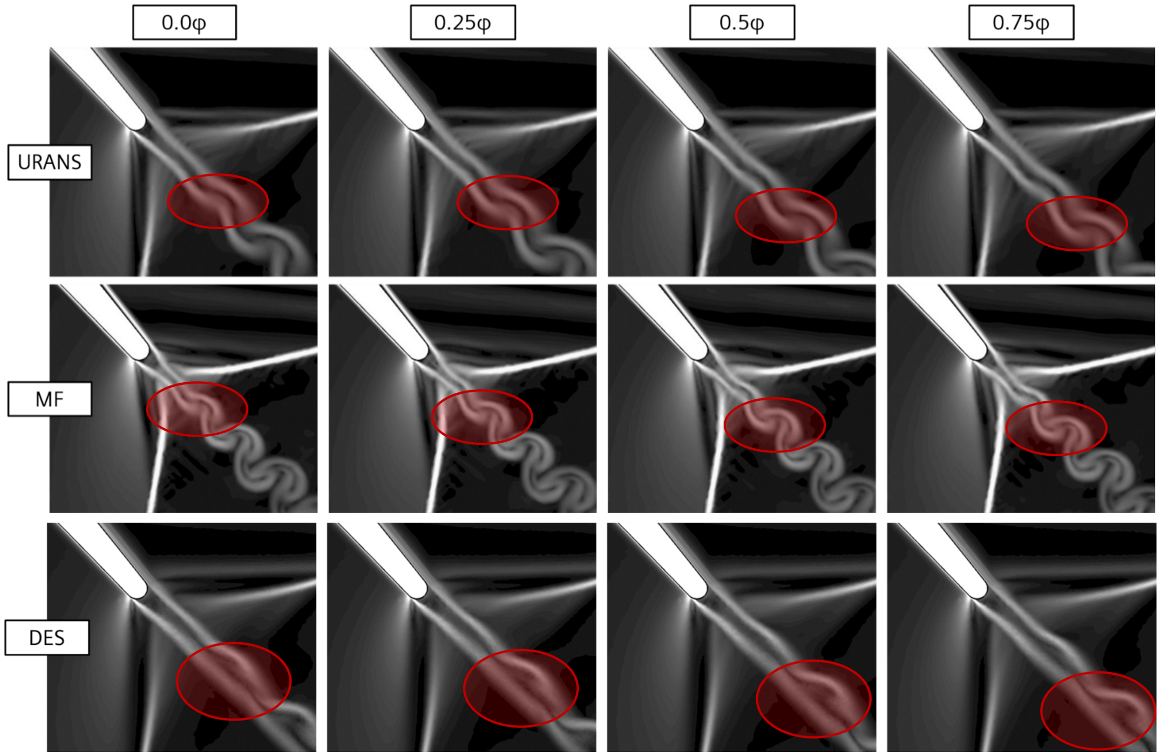

Figure 4.20: Normalized density gradient at the trailing edge - sublimit loading.

surface boundary layer. The flow separates slightly during the shock boundary layer interaction, resulting in slight fluctuations of the suction surface pressure distribution. In a time-averaged sense these pressure fluctuations merge into a smearing of the shock impingement.

Similar to critical loading, the predicted von Karman vortex street for the model free approach is tighter and more frequent than the other unsteady methods. This is a result of the state of the trailing edge boundary layer and pressure side expansion. The model free approach shows a much smaller boundary layer than the other methods; that then causes the size of the base pressure region to shrink. This in turn results in tighter vortex pairs as well as closer trailing edge shocks. Both the URANS and DES simulations predict the size of the base pressure region to be much larger than the model free approach. However, as can be seen the DES predicts vortex formation to occur much farther downstream.

4.3.3.3 Limit Loading

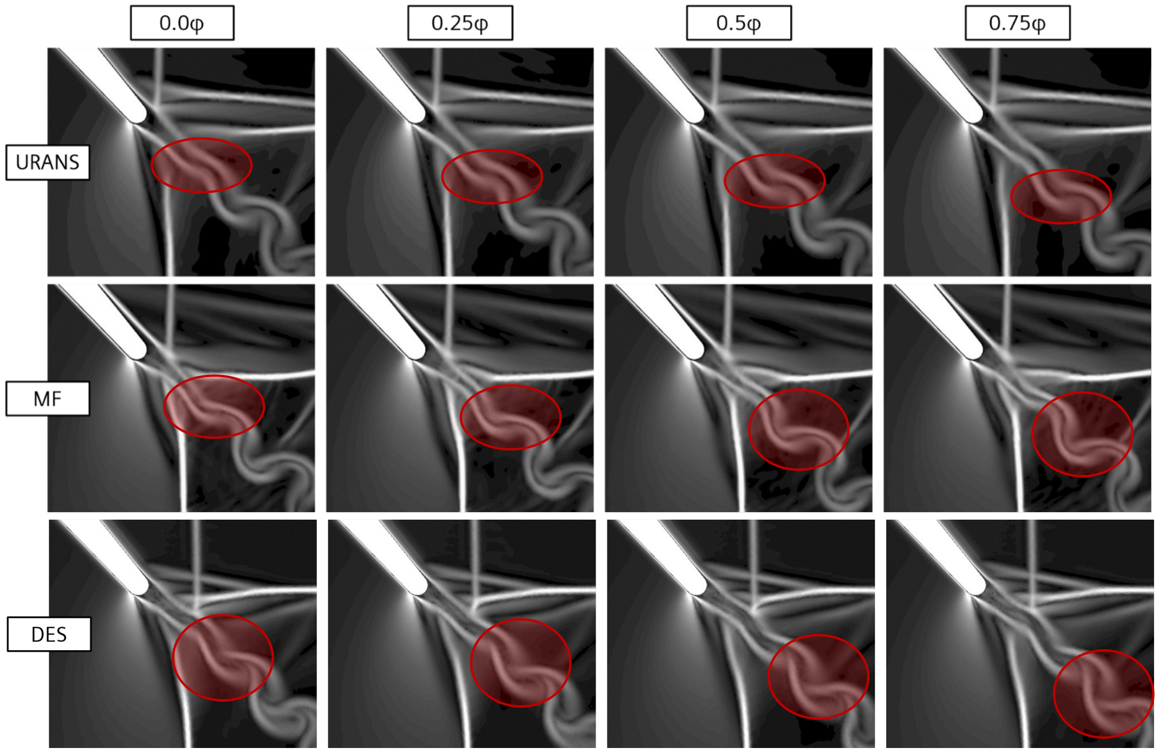

Figure 4.21: Normalized density gradient at the trailing edge - limit loading.

Lastly the instantaneous predictions of the limit loading condition are presented in Figure 20. Clearly, the flow is intrinsically complex, showing a combination of shock/boundary layer interaction, Prandtl-Meyer expansion, vortex formation as well as flow separation. The rapid expansion around the trailing edge pressure side results in the formation of the base pressure region which then leads to the formation of the oblique trailing edge shock system. Vortices are then shed from the end of the base pressure region, still dominated by the pressure side flow expansion. The oblique pressure side shock, formed at the end of the base pressure region achieves sufficient flow turning to clear the suction surface of the adjacent airfoil and move into the base pressure region. This shock then interacts with the suction side shear layer, creating acoustic disturbances within the suction side boundary layer leading to flow separation upstream of the trailing edge.

Although each modeling approach clearly shows each of the previously described flow structures, the magnitude and location of each are different. The model free simulation predicts a much larger separation period along the suction surface than the other approaches as well as the smallest base pressure region. Both the URANS and DES approaches show similar base pressure sizes; however, the vortex formation downstream is drastically different between the methods. The vortices of the URANS simulation are much thinner and smaller than the DES approach, resulting in the drastic reduction in the predicted Strouhal number for the DES.

4.4 Conclusion

To better understand the effect of vortex shedding on the nature of the trailing edge shock system during airfoil limit loading a computational fluid dynamic investigation was performed for a transonic turbine airfoil at critical, sublimit, limit and super-critical conditions. Four modeling strategies were employed: steady state RANS, unsteady RANS, DES and turbulence model free.

Similar to previous work [21, 3], as limit loading is reached the flow within the airfoil passage becomes fully choked and any further increase in pressure ratio fails to change the channel output. The influence of modeling strategies on the predicted mass-flow averaged total pressure loss coefficient, mass-flow averaged flow angles, and on the limit loading pressure ratio were found to be insignificant with the exception of the URANS model during critical loading. It was found that the URANS modeling approach failed to predict the transition from near trailing edge dominated vortex formation to aft base pressure vortex formation resulting in a drastic rise in predicted total pressure loss.

Surface isentropic Mach distributions were predicted similarly for all modeling strategies, with the exception of the trailing edge base pressure region and points of shock impingement along the suction surface. A smearing of the blade loading was predicted as a result of the relative position of the Trailing Edge Pressure Side

Shock (TEPSS) and the point of vortex formation. When the TEPSS was predicted aft of the trailing edge vortex street, the oscillatory nature of the pressure side shear layer resulted in a fluctuating shock behavior that then propagated to the adjacent airfoil surface. As the pressure ratio was increased and the pressure side shear layer gained sufficient momentum to create a well-defined base pressure region, the oblique trailing edge shock was formed upstream of vortex formation resulting in a relatively stationary shock system.

A detailed review of the boundary layer states at the trailing edge reveals that all of the modeling approaches predicted laminar boundary layer profiles along the pressure surface trailing edge and turbulent profiles along the suction surface. In summary, the model free simulation approach predicted much smaller boundary layer thicknesses, unless separation occurred as did for the limit loading condition. Each modeling strategy predicted separation, although with varying degrees of size and magnitude, during limit loading along the suction side trailing edge caused by acoustic wave propagation of the interaction of the suction side shear layer and the TEPSS.

The predicted base pressure distributions were also reviewed, showing the base pressure to decrease with increasing pressure ratio. The unsteady simulation approaches consistently predicted lower average surface pressures than the steady state RANS simulations. As the pressure ratio was increased the RANS, URANS and DES simulations all showed near identical predictions of the airfoil base pressure, suggesting the flow to be relatively stationary within the region. The model free approach showed a similar distribution; however overall magnitude of the base pressure deficit was increased for all loading conditions.

Temporal documentation of the mass flow averaged total pressure loss coefficient downstream of the airfoil allowed for the dominant vortex shedding frequency to be identified and subsequent Strouhal number to be calculated. It was found that the DES approach predicted the lowest vortex frequency for both the sublimit and limit loading conditions. The model free approach predicted a much smaller base pressure region, resulting in a much higher vortex shedding frequency than the other methods. A formal documentation and review were made outlining the required simulation time step to achieve accurate temporal resolution as well as approximate vortex shedding period.

Qualitative images of the numerical Schlieren (normalized density gradient) contours were presented and reviewed showing large differences in the prediction of vortex shape, size and subsequent shock influence. Although conclusions can be drawn on modeling ability, without extensive experimental documentation no concrete justification can be made at this time, further outlining the importance of an experimental investigation.

REFERENCES

[1] C. H. Hauser, H. W. Plohr, and G. Sonder, "Study of flow conditions and deflection angle at exit of two-dimensional cascade of turbine rotor blades at critical and supercritical pressure ratios," *NACA-RM E9K25*, 1950.

[2] C. H. Hauser and H. W. Plohr, "Two-dimensional cascade investigation of the maximum exit tangential velocity component and other flow conditions at the exit of several turbine blade designs at supercritical pressure ratios," *NACA-RM E51F12*, 1951.

[3] I. Fruchtman, "The limit load of transonic turbine blading," in *Turbo Expo: Power for Land, Sea, and Air*, vol. 79788, p. V01AT01A080, American Society of Mechanical Engineers, 1974.

[4] A. J. Glassman, "Estimating turbine limit load," *NASA CR-191105*, 1993.

[5] S. S. Chen, "Axial-flow turbine rotor discharge-flow overexpansion and limit-loading condition. part 2; method of analysis and performance evaluation of computer code axod2," *NASA/TM-2018-219911*, 2018.

[6] S. Owen, F. Taremi, and M. Uddin, "Effect of inflow conditions on transonic turbine airfoil limit loading." unpublished - Accepted - IMechE Journal of Power and Energy, 2021.

[7] C. Sooriyakumaran, "Experimental study of profile losses in three transonic turbine cascades," masters thesis, Carelton University, 2014.

[8] C. H. Sieverding, H. Richard, and J.-M. Desse, "Turbine blade trailing edge flow characteristics at high subsonic outlet mach number," *J. Turbomach.*, vol. 125, no. 2, pp. 298–309, 2003.

[9] D. Corriveau and S. Sjolander, "Influence of loading distribution on the performance of transonic high pressure turbine blades," *Journal of Turbomachinery(Transactions of the ASME)*, vol. 126, no. 2, pp. 288–296, 2004.

[10] S. Owen, F. Taremi, and M. Uddin, "Turbulence modeling effects of transonic, high pressure airfoils near design incidence," in *AIAA Aviation 2019 Forum*, p. 2965, 2019.

[11] T. Léonard, L. Y. Gicquel, N. Gourdain, and F. Duchaine, "Steady/unsteady reynolds-averaged navier–stokes and large eddy simulations of a turbine blade at high subsonic outlet mach number," *Journal of Turbomachinery*, vol. 137, no. 4, p. 041001, 2015.

[12] D. Lin, X. Yuan, and X. Su, "Local entropy generation in compressible flow through a high pressure turbine with delayed detached eddy simulation," *Entropy*, vol. 19, no. 1, p. 29, 2017.

[13] X. I. Yang and K. P. Griffin, "Grid-point and time-step requirements for direct numerical simulation and large-eddy simulation," *Physics of Fluids*, vol. 33, no. 1, p. 015108, 2021.

[14] K. K. Agarwal, S. R. Konakalla, and S. Selvan, "On meshing guidelines for large eddy simulations of gas turbine combustors," in *Turbo Expo: Power for Land, Sea, and Air*, vol. 45691, p. V04BT04A011, American Society of Mechanical Engineers, 2014.

[15] M.-S. Liou, "Ten years in the making-ausm-family," in *15th AIAA Computational Fluid Dynamics Conference*, p. 2521, 2001.

[16] Siemens, "Star-ccm+ user manual," 2021. Last accessed 10 Oct. 2021.

[17] C. Sieverding and M. Manna, "A review on turbine trailing edge flow," *International Journal of Turbomachinery, Propulsion and Power*, vol. 5, no. 2, p. 10, 2020.

[18] C. Sieverding, M. Stanislas, and J. Snoek, "The base pressure problem in transonic turbine cascades," in *ASME 1979 International Gas Turbine Conference and Exhibit and Solar Energy Conference*, pp. V01BT02A019–V01BT02A019, American Society of Mechanical Engineers, 1979.

[19] L. S. Han and W. Cox, "A visual study of turbine blade pressure-side boundary layers," in *Turbo Expo: Power for Land, Sea, and Air*, vol. 79566, p. V001T01A020, American Society of Mechanical Engineers, 1982.

[20] T. C. Currie and W. E. Carscallen, "Simulation of trailing edge vortex shedding in a transonic turbine cascade," in *Turbo Expo: Power for Land, Sea, and Air*, vol. 78729, p. V001T01A119, American Society of Mechanical Engineers, 1996.

[21] S. S. Chen, "Axial-flow turbine rotor discharge-flow overexpansion and limit-loading condition, part 1: Computational fluid dynamics (cfd) investigation," *NASA/TM-2017-219506*, 2017.

CHAPTER 5: CONCLUSIONS

In this dissertation a detailed methodology to simulate the prediction of airfoil limit loading was developed and a thorough investigation into the factors that influence the limit loading condition was conducted.

Chapter 2 provides a computational baseline using data previously collected at the Pratt & Whitney Canada High-Speed Wind Tunnel at Carleton University. An assessment of the predictive capabilities of a number of Reynolds-Averaged Naiver-Stokes eddy viscosity turbulence models showed the shear stress transport $k - \omega$ turbulence model with γ transition to have superior predictive veracity for the limit loading condition. The development of a novel adaptive mesh refinement algorithm based on the normalized local cell gradients of total pressure, total temperature, density, turbulent kinetic energy, turbulent eddy viscosity and the specific dissipation rate of turbulence was presented and shown to provide an overall reduction in computational cost of 50% per simulation.

After demonstrating the ability to properly capture the aerodynamics surrounding a turbine airfoil under design conditions the investigation was extended to the potential inflow conditions supplied by an upstream combustor in Chapter 3. Influence of inflow conditions was found to be minimal on the exit flow profile with the exception of the mass-flow averaged total pressure loss coefficients. Results show incidence variation to change the total pressure loss coefficient differently for each airfoil, whereas turbulence intensity and turbulent length scale predicted a drastic rise in loss with increased turbulence level for all airfoils considered. The geometric characteristics of each airfoil were also investigated for influence on the stages to limit loading. Similar to previous experimental work the limit loading pressure ratio and the mass-flow averaged outlet flow angle were strongly correlated with the airfoil outlet metal angle. It was also determined that the airfoil stagger and trailing edge blockage ratio play a role in the determination of the sublimit loading range.

Lastly the effect of transient vortex shedding on the nature of the trailing edge shock system and subsequent influence on the stages towards limit loading was determined in Chapter 4. A detailed review of the boundary layer states at the trailing edge were performed showing that all of the modeling approaches predicted laminar boundary layer profiles along the pressure surface trailing edge and turbulent profiles along the suction surface trailing edge. Each modeling strategy predicted separation along the suction surface during limit loading due to acoustic wave propagation caused by the shock-base pressure interaction, although with varying degrees of size and magnitude.

Temporal evolution of the mass flow averaged total pressure loss coefficient downstream of the airfoil allowed for the dominant vortex shedding frequency to be identified and subsequent Strouhal number to be calculated. It was found that each transient modeling strategy predicted the vortex frequency differently. A formal documentation and review were made outlining the required simulation time step to achieve accurate temporal resolution as well as approximate the vortex shedding period. Qualitative images of numerical Schlieren (normalized density gradient) contours were presented and reviewed showing large differences in the prediction of vortex shape, size and subsequent shock influence.

Although conclusions were made on modeling ability and influence of airfoil geometric characteristics on the stages towards limit loading, without extensive experimental documentation no concrete justification can be made at this time. Future work is required isolating the limit loading condition to provide the aerodynamic community with a complete understanding of how to mitigate costly design deficiencies going forward.